Institut für Angewandte Physik
Fachrichtung Physik
Fakultät Mathematik und Naturwissenschaften
Technische Universität Dresden

Low Voltage Electron Emission from Ferroelectric Materials

Dissertation
zur Erlangung des akademischen Grades
Doctor rerum naturalium
(Dr. rer. nat.)

vorgelegt von
Oliver Mieth
geboren am 17. Februar 1981 in Meißen

Dresden 2010

TECHNISCHE
UNIVERSITÄT
DRESDEN

Eingereicht am 11.03.2010

1. Gutachter: Prof. Dr. Lukas M. Eng

2. Gutachter: Prof. Dr. Ramamoorthy Ramesh

Verteidigt am 26.10.2010

Abstract

Electron emission from ferroelectric materials is initiated by a variation of the spontaneous polarization. It is the main focus of this work to develop ferroelectric cathodes, which are characterized by a significantly decreased excitation voltage required to initiate the electron emission process. Particular attention is paid to the impact of the polarization on the emission process. Two materials are investigated. Firstly, relaxor ferroelectric lead magnesium niobate - lead titanate (PMN-PT) single crystals are chosen because of their low intrinsic coercive field. Electron emission current densities up to $5 \cdot 10^{-5}\,\mathrm{A/cm^2}$ are achieved for excitation voltages of 160 V. A strong enhancement of the emission current is revealed for the onset of a complete polarization reversal. Secondly, lead zirconate titanate (PZT) thin films are investigated. A new method to prepare top electrodes with sub-micrometer sized, regularly patterned apertures is introduced and a stable electron emission signal is measured from these structures for switching voltages $< 20\,\mathrm{V}$. Furthermore, a detailed analysis of the polarization switching process in the PMN-PT samples is given, revealing a spatial rotation of the polarization vector into crystallographic easy axes, as well as the nucleation of reversed nano-domains. Both processes are initiated at field strengths well below the coercive field. The dynamics of the polarization reversal are correlated to the electron emission measurements, thus making it possible to optimize the efficiency of the investigated cathodes.

Kurzfassung

Die Ursache für Elektronenemission aus ferroelektrischen Materialien ist eine Veränderung des Zustandes der spontanen Polarisation. Gegenstand der vorliegenden Arbeit ist eine Verringerung der dafür nötigen Anregungsspannung, wobei besonderes Augenmerk auf die Rolle der ferroelektrischen Polarisation innerhalb des Emissionsprozesses gelegt wird. Es werden zwei verschiedene Materialien untersucht. Das Relaxor-Ferroelektrikum Bleimagnesiumniobat - Bleititanat (PMN-PT) wurde aufgrund seines geringen Koerzitivfeldes ausgewählt. Es konnten Emissionsstromdichten von bis zu $5 \cdot 10^{-5}\,\mathrm{A/cm^2}$ bei einer Anregungsspannung von 160 V erreicht werden. Bei Einsetzen eines vollständigen Umschaltens der Polarisation wurde eine deutliche Verstärkung des Emissionsstromes festgestellt. Desweiteren werden Untersuchungen an Bleizirkoniumtitanat (PZT) Dünnfilmen gezeigt. Eine neue Methode, eine Elektrode mit periodisch angeordneten Aperturen im Submikrometerbereich zu präparieren, wird vorgestellt. Diese Strukturen liefern ein stabiles Emissionssignal für Anregungsspannungen $< 20\,\mathrm{V}$. Eine detailierte Analyse des Schaltverhaltens der Polarisation der PMN-PT Proben zeigt sowohl eine Rotation des Polarisationsvektors als auch eine Nukleation umgeschaltener Nanodomänen. Beide Prozesse starten bei Feldstärken unterhalb des Koerzitivfeldes. Die ermittelte Zeitabhängigkeit des Schaltprozesses erlaubt Rückschlüsse auf den Emissionsprozess und erlaubt es, die Effizienz der untersuchten Kathoden weiter zu optimieren.

Contents

1 Introduction

Since the discovery of cathode rays in the 19^{th} century [1], different kinds of electron sources have been invented. This development not only changed most peoples's everyday life, but also stimulated scientific progress in many ways. The invention of television based on cathode ray tubes brought the "world" into millions of living rooms. The electron was discovered as a particle based on experiments on cathode rays [2] and the successful explanation of electron emission due to the photoelectric effect [3] represents a breakthrough in quantum physics being finally rewarded with the Nobel Prize. The wave character of emitted electrons is exploited in electron microscopes [4], which opened the door to the nanoworld.

There have always been attempts to improve existing cathodes as well as to develop new types of electron emitters, but it was not before 1974 when the idea of ferroelectric emitters has been reported [5]. Ferroelectricity was discovered in 1921 [6]. Since then scientific interest in this materials has increased drastically. In the 1940s, the possible use in sonar applications for submarine detection of recently discovered ferroelectric oxides initiated a new era of research in this field. Nowadays, ferroelectrics are particularly promising candidates for non-volatile memory devices [7], but also finding increased interest in functional meta-material applications [8, 9]. Accordingly, after decades of research, the preparation of high-quality single crystals and thin films is well established and has been extended to a wide variety of materials.

The mechanism of ferroelectric electron emission (FEE) is different from any other kind of cathodes developed so far. The crystal lattice provides not only a reservoir of electrons but is directly involved in the emission process [10]. A variation of the ferroelectric polarization, which is induced by distortions of the crystal structure, initiates the emission of surface charges that screened the depolarization field.

The first period of research on ferroelectric electron emission was characterized by small emission current densities ($< 10^{-7}\,\mathrm{A/cm^2}$) achieved by pyroelectric, piezoelectric or electric field induced polarization variations from single crystal ferroelectrics. Much higher current densities of up to 100 A/cm^2 have been found in 1989 [11], which was accomplished by a new kind of top electrodes being prepared on the ferroelectric emitters. A metal layer with patterned apertures allowed the formation of a surface flashover plasma that enhanced the emission current tremendously. Inspired by this, many groups joined this topic and investigations were performed on almost any known ferroelectric material using different electrode patterns. It was shown that ferroelectric cathodes can be used as electron sources in microwave tubes [12] or in flat panel displays [13].

However, since the emission efficiency is poorer in thin films compared to bulk materials, most presented cathodes were single crystals or ceramics with thicknesses of $> 100\,\mu$m, and corresponding operation voltages of several kV. Moreover, most investigated materials exhibit quite large coercive fields. As a result, high voltages are required to switch the spontaneous polarization and to induce a polarization variation sufficient to initiate an emission of electrons. Lower operation voltages of ferroelectric electron sources are desired not only for reasons of convenience and applicability but also to reduce the power consumption for this kind of cathodes.

It is the objective of the present work to proove that ferroelectric electron emission is possible at drastically reduced excitation voltages and to clarify the role of ferroelectric polarization within the emission process.

A brief introduction into the phenomenon of ferroelectricity (see Chapter 2) is followed by a description of the basic principles of ferroelectric electron emission in Chapter 3. The experimental setup and methods are introduced in Chapter 4.

Two different ferroelectric systems were investigated. Lead magnesium niobate - lead titanate (PMN-PT) single crystals and lead zirconate titanate (PZT) thin films both promise low voltage electron emission. PMN-PT is a relaxor ferroelectric material that recently attracted great interest due to its outstanding piezoelectric properties [14]. The spontaneous polarization can be reversed with low applied electric fields ($\sim 2\,$kV/cm^2), which is about one order of magnitude smaller than for most other ferroelectrics, and thus a large polarization variation can be induced at moderate voltage amplitudes $< 100\,$V even for single crystals with a thickness of several hundreds of µm. The achieved results are presented and discussed in Chapter 5.

A different approach to reduce the operation voltage for electron emission was performed for PZT thin films. As can be seen in Chapter 6, a reduced emitter thickness enables the polarization switching and subsequently, the onset of electron emission at lower voltages.

In Chapter 7 the reversal of the ferroelectric polarization in the emitter structures is investigated in detail and correlations to the emission process are revealed. Finally, a summary of the presented results and conclusions is given in Chapter 8, as well as suggestions of a further optimization of the investigated electron emitters.

2 Ferroelectricity

The phenomenon of ferroelectricity is introduced in this chapter. The most important properties of ferroelectric materials are explained and examples of applications are given. Relaxor ferroelectricity is described in more detail and differences between ferroelectric single crystals and thin films are pointed out. Finally, the materials investigated in the present work are specified and described.

2.1 Basic Properties of Ferroelectrics

The piezoelectric effect describes the appearance of an electric polarization $\mathbf{P}$ within a solid if it is exposed to mechanical stress $\mathbf{S}$. This effect is caused by a relative displacement of the centers of positive and negative charges. Therefore, piezoelectricity appears in noncentrosymmetric materials only. Accordingly, the application of an electric field $\mathbf{E}$ to a piezoelectric leads to mechanical strain $\boldsymbol{\varepsilon}$ in this material. This is called converse piezoelectric effect.

Some piezoelectrics exhibit a spontaneous polarization in the absence of mechanical stress. This subgroup of piezoelectrics is called pyroelectrics (see Figure 2.1). If the orientation of this spontaneous polarization can be changed by an applied external electric field, the pyroelectric material is called ferroelectric [15].

In most materials, ferroelectricity is only present below the so-called Curie temperature T_C [17]. For temperatures higher than T_C the material is in the paraelectric phase and shows no spontaneous polarization. The order of the phase transition between the ferroelectric and the paraelectric phase determines the type of ferroelectricity. Two different classes of ferroelectric materials can be distinguished [7]. Order-disorder ferroelectrics exhibit a first order phase transition. The polarization shows a discontinuous change at the Curie temperature. In contrast, displacive ferroelectrics are characterized by a second order phase transition, where the polarization decreases continuously

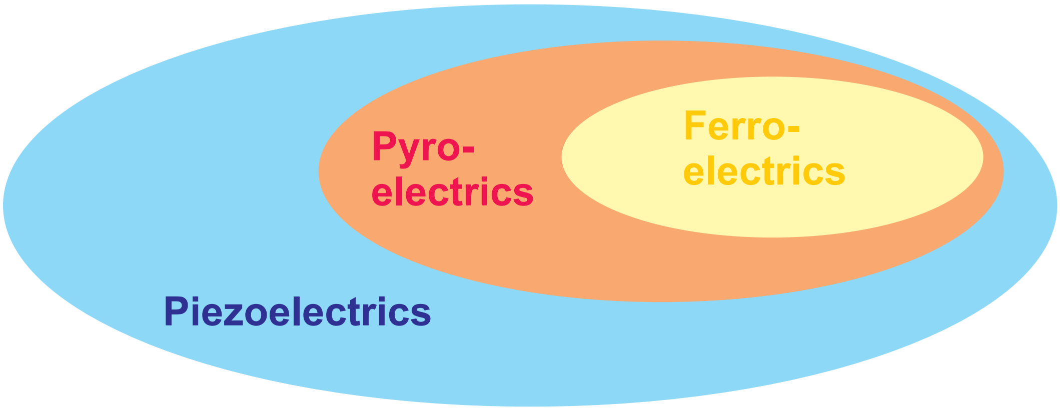

Figure 2.1: Classification of ferroelectric materials. All ferroelectrics are belong to the class of pyroelectric and piezoelectric materials [16].

to zero at T_C.

In displacive ferroelectrics the spontaneous polarization is mainly created by the displacement of differently charged ionic sublattices. This is shown in Figure 2.2 for a perovskite crystal structure. The center positions of positive and negative charges are shifted and thus a microscopic dipole moment is formed within a unit cell. If these dipole moments are parallel for several neighboring unit cells, a macroscopic polarization can be measured.

2.1.1 Ferroelectric Domains

In general, ferroelectric crystals are not polarized uniformly but exhibit regions with different orientations of the ferroelectric polarization. These regions are referred to as domains. The crystal surfaces are charged by the spontaneous polarization. These charges induce a depolarization field which is oriented antiparallel to the polarization. In order to minimize the depolarization field energy, domains with opposite polarization directions are formed. However, the formation of domain walls, which are the boundaries between different domains, also requires energy and thus, the final domain state will be a thermodynamic equilibrium which minimizes the total energy [18].

The width of ferroelectric domain walls usually is in the range of several nanometers. This is much smaller than ferromagnetic domain walls [17]. The type of a domain wall is determined by the polarization orientation on either side of the wall. For a tetragonal crystal structure, 90 ° and 180 ° domain walls are possible (see Figure 2.2). A more complex situation is found in rhombohedral ferroelectric materials. Three types of domain walls are present but the actual angle between the adjacent polarization states depends on the degree of the rhombohedral distortion. The properties of domain walls may be differ-

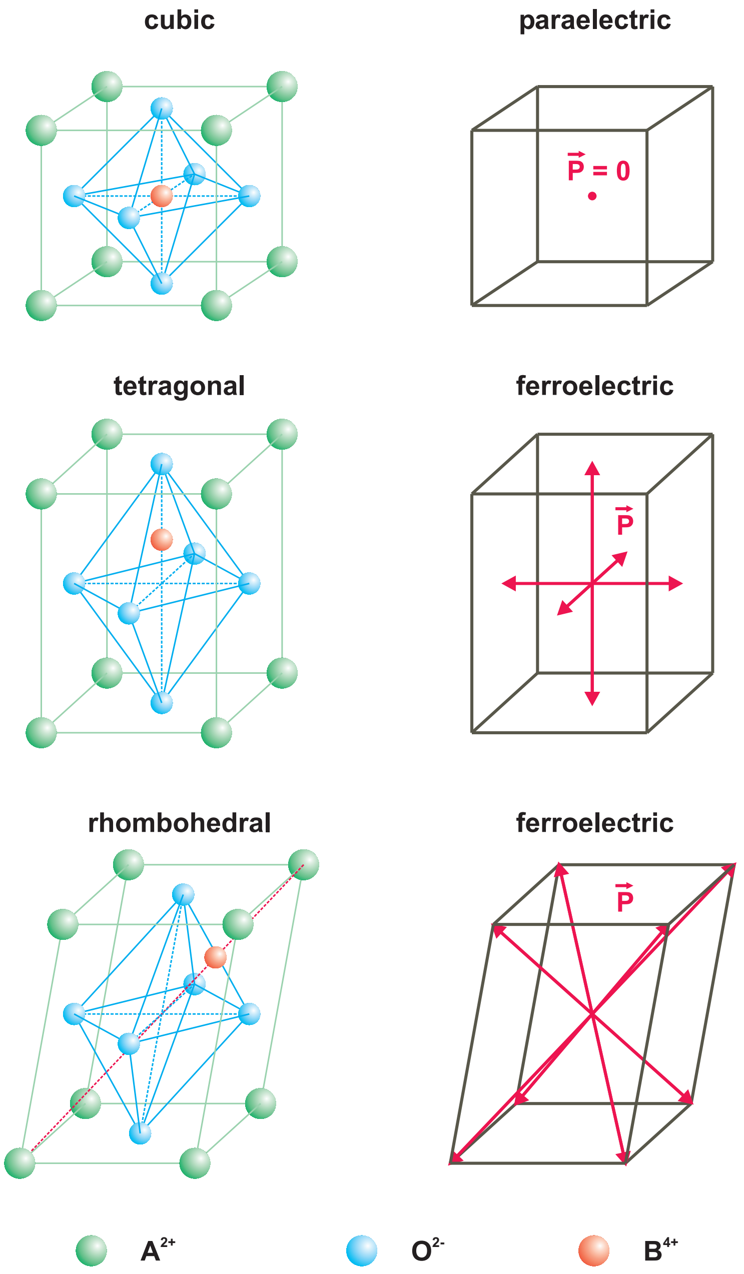

Figure 2.2: Perovskite crystal structure. Perovskite crystals consist of two different positively charged cations A and B and negatively charged oxygen ions. The left column depicts perovskite unit cells with cubic, tetragonal, and rhombohedral symmetry. In the right column the possible orientations of the ferroelectric polarization are shown. For cubic crystal symmetry the material is in a paraelectric phase and no spontaneous polarization is present. In the ferroelectric tetragonal phase the unit cell is distorted and the ion B is shifted from the center position. There are 6 possible polarization orientations. For a rhombohedral crystal structure the B cation is displaced along the body diagonal of the unit cell. This leads to 8 possible orientations of ferroelectric polarization.

ent than for the rest of the material. For instance, an increased conductivity has been measured for certain types of domain walls in ferroelectric bismuth ferrite [19]. Furthermore, in lithium niobate domain walls may be used as a pattern for lithography, since the surface adsorption of metal particles and organic molecules is restricted to domain boundaries only [20].

2.1.2 Switching the Ferroelectric Polarization

The dependence of the polarization **P** on an external electric field **E** typically manifests as a hysteresis loop as shown in Figure 2.3. The maximum polarization value for high electric fields is called saturation polarization $\mathbf{P}_S$. If the electric field is decreased to zero, the remanent polarization $\mathbf{P}_r$ remains. To switch the polarization orientation a certain electric field value, called coercive field $\mathbf{E}_C$, is needed.

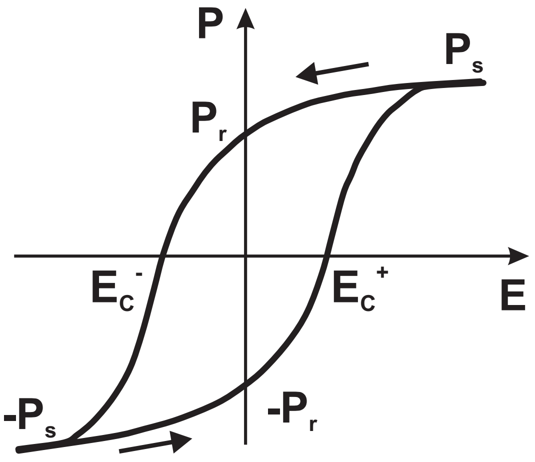

Figure 2.3: Ferroelectric hysteresis loop. The polarization saturates ($\mathbf{P}_S$) for high electric fields. If no electric field is applied, the remanent polarization $\mathbf{P}_r$ remains. The polarization orientation is switched at the coercive fields $\mathbf{E}_C$.

Switching of the ferroelectric polarization is of great importance with respect to most technological applications of ferroelectric materials [7, 18]. Mostly, polarization reorientation is accomplished by the application of an electric field higher than the coercive field. However, the application of mechanical stress may also be sufficient to switch the polarization state [21]. To initiate the switching process nucleation centers of the reversed polarization state are needed. In principle, this domain nucleation can start anywhere in the ferroelectric but is likely to take place in the vicinity of defects, existing domain walls, and the material surface, since there, the energy barrier for domain nucleation is significantly reduced [22]. The nucleation centers are not stable below a critical size limit of several nanometers and may disappear again [23]. Nevertheless, after the reversed domains have gained a sufficient size, they grow in the direction of the applied electric field. This process takes place on a time scale of several nanoseconds and the resulting needle-like domains connect both crystal surfaces. However, only a small volume fraction of the material is switched this way and in parallel, a slower sideward motion of the domain walls is initiated. This process is driven by permanent two-dimensional nucleation at the domain boundaries. The newly created nucleation centers merge together and the domain wall this way moves through the material connecting the several needle-like domains until the switching process is completed.

2.1.3 Applications of Ferroelectric Materials

Because of their unique properties ferroelectric materials have found their way into numerous applications [24]. In the following some examples are listed:

1. The high dielectric permittivity of ferroelectrics makes them suitable for the use as dielectrics in compact capacitor structures and dynamic random access memory (DRAM) devices [25].
2. The piezoelectric properties are employed in transducers, actuators, and electromechanical sensors. [25]
3. The pyroelectric effect in ferroelectrics is used in IR sensors at room temperature [18].
4. Non-linear optical behavior is employed for optical frequency conversion [26].
5. The coexistence of two or more different polarization states is utilized for data storage in non-volatile memories (FeRAM) [7, 27].

Applications related to electron emission, which is in the focus of the present work, from ferroelectric materials are discussed in more detail in Section 3.5

2.2 Relaxor Ferroelectrics

Relaxor ferroelectrics can be distinguished from conventional ferroelectric materials by three characteristic features [28]:

1. The absence of a sharp phase transition to an ordered ferroelectric phase. The polarization does not vanish at a particular phase transition temperature T_C but decreases more or less gradually to zero. This can be seen in Figure 2.4 (a) for the example of $Pb(Sc_{1/2}Ta_{1/2})O_3$ (PST).

2. The strong frequency dispersion of dielectric permittivity for temperatures close to the maximum of the permittivity. This maximum is shifted to higher temperatures for higher frequencies.

3. The absence of any optical anisotropy.

Exemplarily, the polarization dependence of $Pb(Sc_{1/2}\ Ta_{1/2})O_3$ (PST) is shown in Figure 2.4 (a) [29]. After thermal annealing, this material is in an ordered state, i.e. the Sc^{3+} and Ta^{5+} ions are distributed homogeneously. The dependence of polarization on temperature shows the ferroelectric nature of this state, since the polarization keeps a constant value for increasing temperatures and disappears abruptly at the phase transition temperature. If PST is in a disordered state, where Sc^{3+} and Ta^{5+} ions are randomly distributed, the material shows relaxor ferroelectric behavior and the depolarization starts at lower temperatures. No sharp phase transition can be seen but the polarization decreases gradually. Figure 2.4 (b) shows the frequency dispersion of the dielectric permittivity and the loss factor as functions of temperature for lead magnesium niobate $Pb(Mg_{1/3}\ Nb_{2/3})O_3$ (PMN) [30]. This material will be introduced in more detail in section 2.4. For ferroelectric materials a maximum of the permittivity corresponds to a phase transition between paraelectric and ferroelectric phase [18]. It is clearly visible that for PMN the maxima of the permittivity are shifted to higher temperatures for increasing frequencies. This is a typical relaxor behavior for a relaxor ferroelectric.

The origin of relaxor ferroelectricity is found in small polar nanoclusters, which show up on unit cell dimensions [31]. Relaxors with a perovskite structure (see Figure 2.2) mostly have at least two differently charged B site cations. Therefore, charge neutrality is not given for a single unit cell but for a larger volume depending on the charge difference and spatial distribution of the ions. This leads to randomly oriented electric fields within the material, which disturb any long range ordering as it is present in conventional ferroelectrics. Instead of domains with a uniform polarization small polar clusters are formed. However, the application of an electric field at temperatures well below the paraelectric phase transition point can initiate a transition to a ferroelectric phase where the polar clusters are oriented in parallel. This goes along with a transformation of the crystal structure as has been shown for PMN [32].

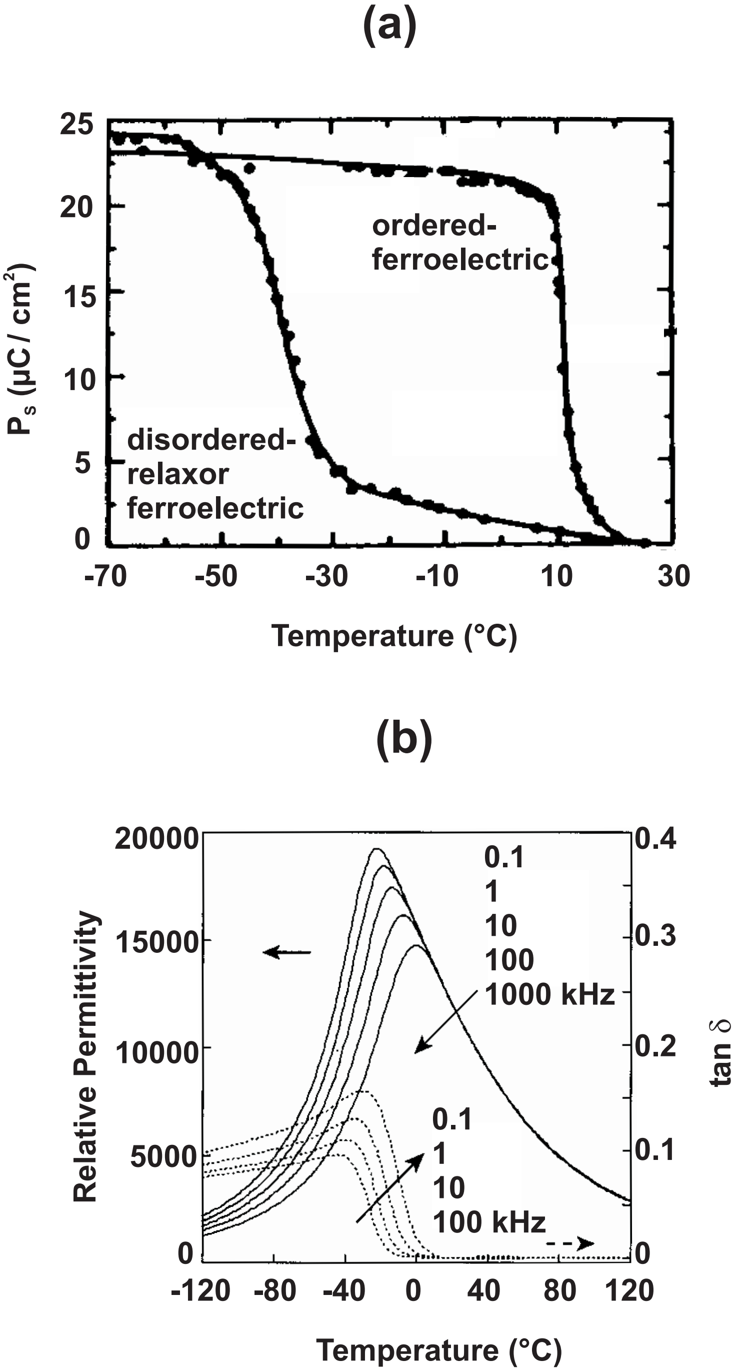

Figure 2.4: Characteristic features of a ferroelectric relaxor. (a) Spontaneous polarization of Pb($Sc_{1/2}Ta_{1/2}$)O_3 (PST) as a function of temperature. In a thermal annealed state the material exhibits an ordered structure with ferroelectric properties. The polarization disappears abruptly for temperatures above the phase transition temperature. In a disordered state the material is relaxor ferroelectric and the polarization decreases gradually to zero for increasing temperatures [29]. (b) Temperature dependence of the relative permittivity and dielectric losses of 0.49 mm thick lead magnesium niobate (PMN) bulk ceramic at various frequencies [30].

There, the application of a DC electric field leads to a transition from cubic to rhombohedral crystal symmetry.

An intuitive explanation for the slow depolarization effect with increasing temperatures and the absence of a sharp phase transition might be the presence of distinct Curie temperatures T_C for different regions within the material. Since the random fields are not homogeneous and influence the energy potential of the polar nanoregions, the activation energy for each cluster is slightly different. Thus, the transition between paraelectric and ferroelectric phase takes place at different temperatures for various clusters. The macroscopic measurements are an average of all polar nanoregions within the material and therefore no sharp phase transition is measured.

Several models have been postulated to explain relaxor ferroelectricity and describe the interaction of small polar clusters and random fields on the nanoscale [28, 33, 34]. However, the reasons for relaxor ferroelectricity are still under debate and not completely understood. Nevertheless, their high piezoelectric coefficients compared to conventional ferroelectrics and dielectric constants make relaxor materials very interesting for a wide range of applications.

2.3 Ferroelectric Thin Films

The first-investigated ferroelectric materials were single crystals, polycrystalline ceramics, or powders [6, 35]. But the invention and steady improvement of several preparation techniques have lead to high quality ferroelectric films with thicknesses $< 1\,\mu$m [15]. The properties of thin films may differ significantly from bulk materials. It is possible to manipulate the polarization with much lower voltages compared to thick crystals, which is one reason why thin films have attracted such great interest [7].

However, a lot of extrinsic influences must be taken into account for understanding the behavior of ferroelectric films. The most important external impact is the interaction of the ferroelectric layer with the substrate. The deposited ferroelectric and the substrate possess different lattice constants. The resulting lattice mismatch induces mechanical strain in the film [36]. Since piezoelecticity and ferroelectricity are coupled and most ferroelectrics are simultaneously ferroelastic[*], the ferroelectric properties are directly affected by

---

[*] Ferroelasticity decribes the dependence of an internal mechanical strain on external mechanical stress. In analogy to ferroelectric materials, the external stress can switch the orientation of the internal strain, which is coupled to the piezoelectric deformation and therefore to the ferroelectric polarization.

the induced strain. It has been shown that for compressive stress polarization orientations perpendicular to the sample surface are preferred. Accordingly, tensile substrate induced stress leads to the formation of domains with polarization directions within the surface plane of the sample [37]. Furthermore, a particular polarization orientation may become energetically favored, i.e. the film is prepolarized by the substrate stress [15]. The induced stain can be relaxed by the formation of dislocations and defects in the crystal structure of the ferroelectric. This effect is the more probable the thicker the prepared layer and the larger the lattice mismatch. However, defects also influence the ferroelectric properties since internal electric fields prepolarize the sample or even prevent a switching of polarization.

There are also intrinsic effects which lead to differences between ferroelectric films and crystals. In the literature these are called *size-effects* [24, 38]. The depolarization field, which has been introduced in section 2.1.1, is larger in thin films and may suppress the formation of a spontaneous polarization. Critical size limits of several nanometers have been predicted, but measurements of ultrathin films still proved the existence of a polarization [39, 40]. Probably, the screening by free surface charges diminishes the impact of the depolarization field.

In summary, the properties of ferroelectric thin films are mainly governed by the interaction with the substrate. A decrease of the remanent polarization for lead zirconate titanate (PZT) has been reported for decreasing film thickness [41] as well as an increasing coercive field [42]. However, the absolute value of polarization for thin films can be significantly larger than for the respective bulk structures [43]. Thus, improving the ferroelectric properties by strain engineering seems a promising possibility to adapt thin films to the demands of many applications.

2.4 Materials

The two material systems investigated within this work are introduced in the following.

2.4.1 Lead Magnesium Niobate - Lead Titanate

$Pb(Mg_{1/3}\ Nb_{2/3})O_3$ - $PbTiO_3$ (PMN-PT) is a relaxor ferroelectric (see Section 2.2). The local disorder is caused by the Mg^{2+} and Nb^{5+} ions, which carry different charges and both occupy the B cation sites in the perovskite unit cell. The addition of lead titanate ($PbTiO_3$), which contains Ti^{4+} ions as

B cations, increases the number of possible B cations to three. The randomly oriented local electric fields are decreased, since a unit cell containing a Ti^{4+} ion is charge neutral and the relaxor-based effects are reduced. Thus, it can be stated -in a simplified picture- that the addition of lead titanate makes the composition more ferroelectric. Accordingly, by changing the ratio of PMN and PT it is possible to tune the properties of the composition.

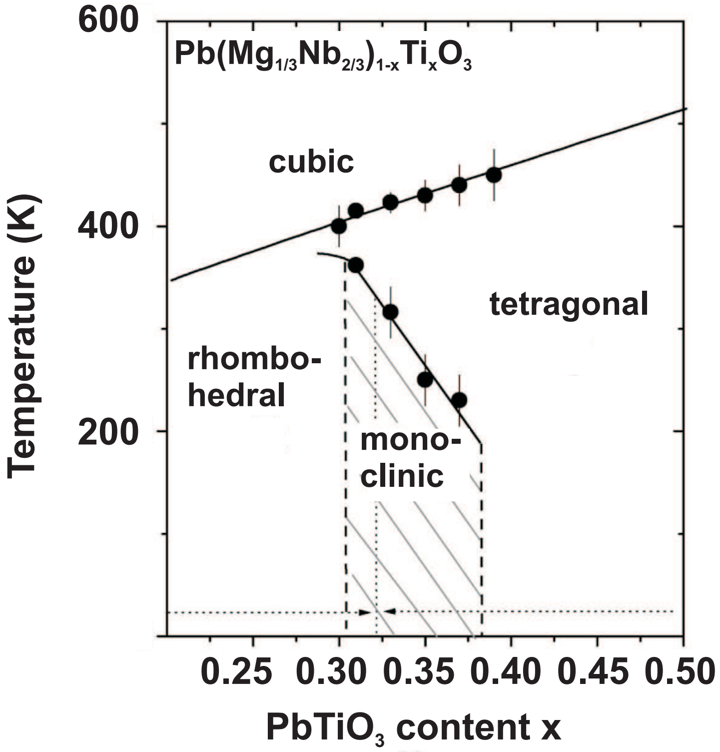

Figure 2.5: Phase diagram of PMN-PT. Above a certain temperature T_C the material is in a cubic paraelectric phase. The value of T_C increases for higher PT contents. The dotted vertical line represents a morphotropic phase boundary between a rhombohedral and a tetragonal phase of crystal symmetry. The coexistence of regions with monoclinic symmetry has been reported for PT ratios of $31\,\% \leq x \leq 37\,\%$ [44].

In Figure 2.5 a phase diagram of PMN-PT is depicted [44]. An increase of the transition temperature to the cubic paraelectric phase for higher lead titanate contents is clearly visible. Furthermore, for a composition with 33 % of lead titanate the crystal symmetry changes from rhombohedral to tetragonal. These phases are separated by a morphotropic phase boundary[†]. However, within a range of $31\,\% \leq x \leq 37\,\%$ for the mole fraction of PT the coexistence of regions with monoclinic crystal symmetry has been reported [45]. The close proximity and coexistence of several crystal symmetries is probably the origin

---

[†] A morphotropic phase boundary shows no temperature dependence.

of the very large piezoelectric coefficients of PMN-PT compositions close to the morphotropic phase boundary. Piezoelectric coefficients $d_{33} > 2.5\,\mathrm{nC/N}$ and responses $> 2\,\mathrm{nm/V}$ have been measured for PMN-PT and the similar composition PZN-PT, where magnesium is substituted by zirconium [14]. These values are much larger than for other piezoelectric materials and have stimulated extended research on such compositions. The current picture of the driving mechanism of the piezoelectric response is a rotation of ferroelectric polarization during the phase transition from rhombohedral to tetragonal crystal structure [46, 47]. This rotation will be discussed in more detail in section 7.3, where a complete 180 ° rotation path of the polarization is revealed.

The samples used in this work possess a lead titanate content of 28 % and a rhombohedral crystal structure according to Figure 2.5. This has been confirmed by means of X-ray diffraction experiments which revealed a unit cell parameter $a = 4.0227(2)$ Å and a distortion from cubic phase of $\alpha = 89.90(1)\,^{\circ}$ [48]. The single crystal samples were purchased by Morgan Electro Ceramics (US) with both surfaces covered by a gold electrode. One side was polished afterwards which reduced the sample thicknes to approximately 400 μm. The crystals were bought in a poled state with the polarization being preferably oriented upwards.

2.4.2 Lead Zirconate Titanate (PZT)

Lead zirconate titanate is a composition between the antiferroelectric lead zirconate ($PbZrO_3$) and the ferroelectric lead titanate ($PbTiO_3$). The B cation site in the perovskite unit cell thus is occupied by either a Zr^{4+} or a Ti^{4+} ion. Similarly to PMN-PT, the ratio between the two components determines the properties of the whole composition.

In the phase diagram of PZT, which is shown in Figure 2.6, it can bee seen that the Curie temperature is increased for higher contents of $PbTiO_3$ from 230 °C, the value for pure $PbZrO_3$, to 490 °C for pure $PbTiO_3$ [49]. It is also visible that the crystal structure of the ferroelectric phase depends on the Zr-Ti ratio. High mole fractions of lead titanate result in a tetragonal structure, whereas lead zirconate contents of more than 52 % lead to a rhombohedral crystal structure. These two phases are separated by a morphotropic phase boundary.

The PZT samples used in this work (see chapter 6) were thin films of $Pb(Zr_{0.4}Ti_{0.6})O_3$ composition. According to Figure 2.6, this corresponds to a tetragonal crystal structure. The thickness of the ferroelectric layer was 600 nm. They were prepared by multi-target sputtering at the Institute of

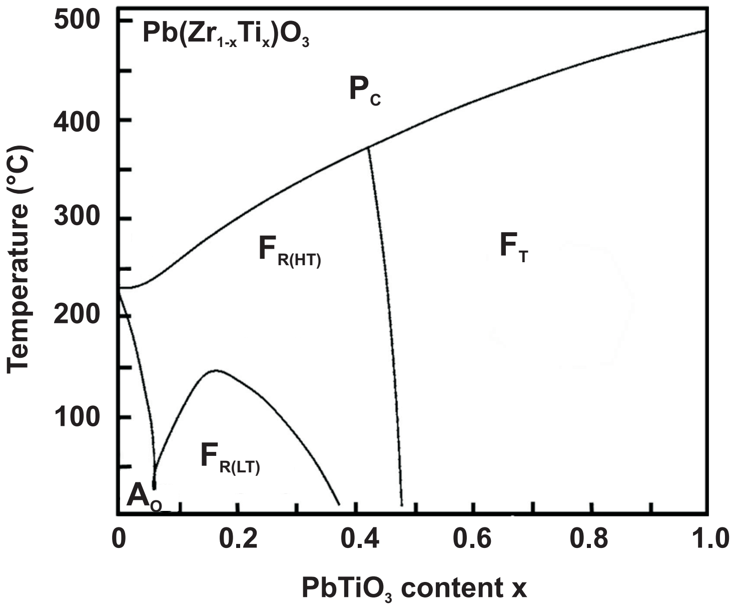

Figure 2.6: Phase diagram of PZT. P$_C$ represents the paraelectric cubic phase for high temperatures. F$_T$ corresponds to the ferroelectric phase with tetragonal crystal symmetry, which is present for high mole fractions of PbTiO$_3$. A morphotropic phase boundary separates the tetragonal phase from the high temperature ferroelectric rhombohedral phase (F$_{R(HT)}$). A second rhombohedral phase at lower temperatures is designed F$_{R(LT)}$. For small PbTiO$_3$ contents the composition is antiferroelectric and shows an orthorombic structure (A$_O$) [49].

Solid State Electronics (TU Dresden) in the group of Professor Gerlach on silicon wafers with an BaPbO$_3$ oxide bottom electrode [50].

3 Ferroelectric Electron Emission

Electron emission from ferroelectric materials exhibits remarkable differences compared to emission from other cathodes. The basic principles of ferroelectric electron emission are described in this chapter. The mechanisms behind the so-called weak and strong emission process will be explained subsequently. Differences and difficulties of electron emission from ferroelectric thin films will be discussed and some applications based on ferroelectric cathodes are described at the end of this chapter.

3.1 General Aspects

Electron emission from ferroelectric materials is initiated by a change of the depolarization field which is induced by the presence of a spontaneous polarization (see chapter 2.1) and oriented antiparallel to the polarization. This field is partially decreased by the formation of domains with different polarization directions. However, since the formation of domain walls requires energy, a residual depolarization field strength remains in the equilibrium state [18]. Free charges located close to the material surface screen the remaining field. These charges either stem from the surrounding medium or from the material itself. The two different systems of charges can be seen in Figure 3.1 (a) for a single domain ferroelectric covered by two electrodes. The bound charges resulting from the spontaneous polarization are shown in white color, whereas the yellow symbols represent the free screening charges on each crystal surface. Figure 3.1 (b) depicts a non-equilibrium state where the polarization orientation is switched. The deviation of spontaneous polarization leads to imbalance charges ΔP that can be screened by three relaxation currents [10].

$$\Delta P = \int_0^t J_C \, dt + \int_0^t J_B \, dt + \int_0^t J_{em} \, dt \tag{3.1}$$

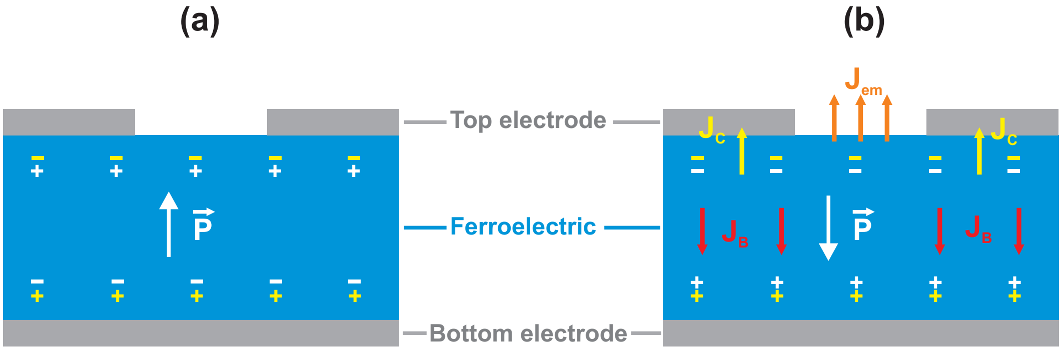

Figure 3.1: (a) Equilibrium state of a single domain ferroelectric. Bound charges resulting from the spontaneous polarization are shown in white color. The yellow symbols correspond to free surface charges that screen the polarization. (b) Non-equilibrium state after polarization reversal. The bound charges are switched and the relaxation of the polarization change ΔP can take place by three currents. A charge transport through the bulk (J_B) is indicated in red. The yellow arrows represent the compensation current J_C injected from the electrodes, whereas the orange arrows correspond to a charge emission from the material surface. To visualize the direction of electron movement all arrows point in negative current direction.

The term J_C represents the compensation current which is injected from the electrodes to the material (see Figure 3.1 (b)), whereas the bulk conductive current is named J_B. The relaxation time of this current depends on the conductivity of the material and since most ferroelectrics are insulating, this current can be neglected. Nevertheless, in ferroelectric thin films leakage currents might have to be taken into account [7]. The third term J_{em} describes the emission of charges from the material surface.

Ferroelectric electron emission (FEE) is a transient current caused by a change of ferroelectric polarization [10, 51, 52]. This is in contrast to other solid state electron emitters, like metals or semiconductors, which exhibit a continuous emission current. Thus, in order to achieve a steady ferroelectric emission the polarization must be changed periodically. It has to be noted that the deviation of the polarization ΔP is not restricted to complete switching but can also be accomplished by piezoelectric [10] and pyroelectric [5, 53] effects, the initiation of a ferroelectric phase transition [54], or the application of an electric field smaller than the coercive field.

The probabilty of charge emission strongly depends on the electrode structure [55, 56]. Compensation currents injected from the electrodes are competitive to an emission of charges in screening the polarization change. Two sorts of electrode structures have been established for the formation of FEE and can be seen in in Figure 3.2. Part (a) shows a ferroelectric with one surface covered by an electrode whereas the other surface is completely uncoated. The top electrode is positioned in a certain distance δ from the ferroelectric and acts simultaneously as a detector of the emitted charges. In this setup the compensation current J_C is zero and therefore, assuming an insulating sample, the whole screening of ΔP is done by a charge emission current J_{em} (see Equation 3.1). The applied field is oriented perpendicularly to the sample surface and no tangential field components are present. However, depending on the distance δ the vacuum gap between top electrode and sample induces a drop of the applied electric field and thus, higher field strengths are necessary to induce the same polarization change than for an electrode being in direct contact with the sample.

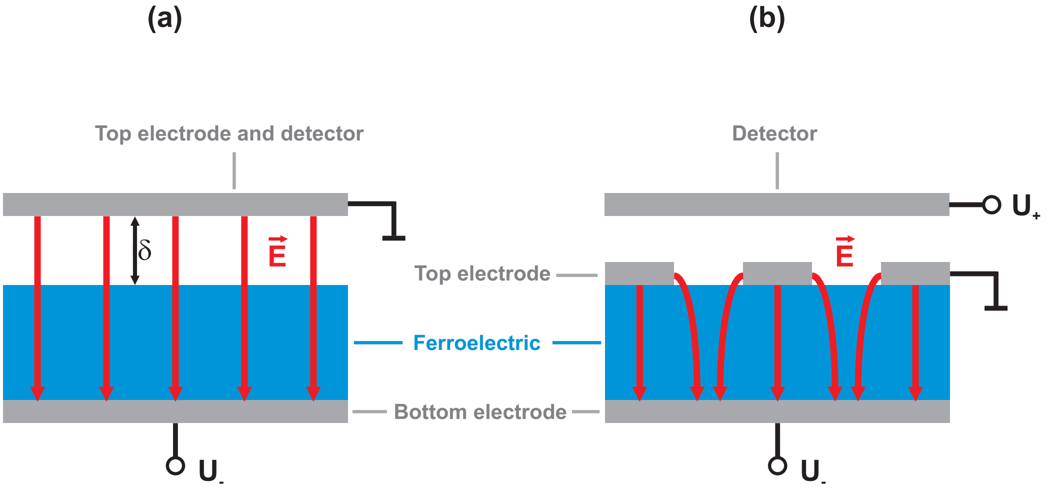

Figure 3.2: Top electrode geometries for Ferroelectric Electron Emission. (a) The top electrode is separated from the ferroelectric surface by a vacuum gap δ. In this "plane-to-plane" geometry only normal components of the electric field are present. Emitted charges are measured as a current flow through the top electrode. (b) The upper electrode is in direct contact to the ferroelectric surface and exhibits apertures which leave some free surface area to enable charge emission from the surface. The electric field shows components parallel to the sample surface within the free surface area. The electron emission is measured by an additional detector.

The latter case is shown in Figure 3.2 (b). The top electrode is prepared in direct contact with the ferroelectric sample. To enable electron emission a free uncoated surface area is necessary. Such openings in the electrode can, for instance, be realized by ring [57] or strip-like patterns [58]. Emitted electrons are measured by a separate detector which is not involved in the emission process. The electrode apertures are only affected by fringing electric fields, which come in from the top electrode edges and contain field components oriented parallel to the sample surface. The impact of these field components will be discussed in Section 3.3. Since the material is partially coated with the electrode, both relaxation currents J_C and J_{em} can be present and the size of the apertures determines the probability and magnitude of the charge emission current.

The top electrode geometry strongly influences the ferroelectric emission process [10]. Two types of FEE can be classified and will be introduced in the following Sections 3.2 and 3.3.

3.2 Weak Ferroelectric Electron Emission

Weak FEE strictly follows the mechanism introduced in Section 3.1. A change of the spontaneous polarization creates strong repulsive fields up to 10^8 V/cm at the ferroelectric surface and the electrons which screened the former polarization state are emitted into free space. In this sense, weak FEE is a field emission of screening charges. Emission currents up to 10^{-7} A/cm^2 have been reported [59]. The electron energy can be as large as 10^5 eV [53].

Weak FEE is realized with both types of electrode geometries shown in Figure 3.2. The most common structure is the "plane-to-plane" geometry with a gap δ between sample and top electrode (see Figure 3.2 (a)). In order to minimize the voltage necessary to initiate the electron emission process, the gap size is kept as small as possible and is usually in the range of several tens of μm.

For a gap free electrode structure, shown in Figure 3.2 (b), the situation is more complicated. Electron emission is limited to originate from the apertures within the top electrode. The application of an electric field induces a polarization change $\Delta\mathbf{P}$ in these free surface areas similar to a "plane-to-plane" geometry and the screening is at least partially done by electron emission. However, the electric field is applied between top and bottom electrode and the strength of the normal field components in free surface areas is more and more reduced for increasing distance from the electrode edges [55]. For large aperture sizes the induced polarization change $\Delta\mathbf{P}$ might be too small to induce a measureable electron emission current. Moreover, compensation currents J_C are present and screen parts of $\Delta\mathbf{P}$. This reduces the amount of charges which is emitted into vacuum. Hence, the aperture size is a very important parameter for optimizing the electron emission current.

Calculations of the electric field distribution within a typical electrode structure can be seen in Figures 3.3, 3.4, and 3.5. A dielectric material of thickness d and permittivity $\varepsilon_r = 500$ is covered by two electrodes. The top electrode exhibits an aperture of size w (see Figure 3.3 (a)). The normal com-

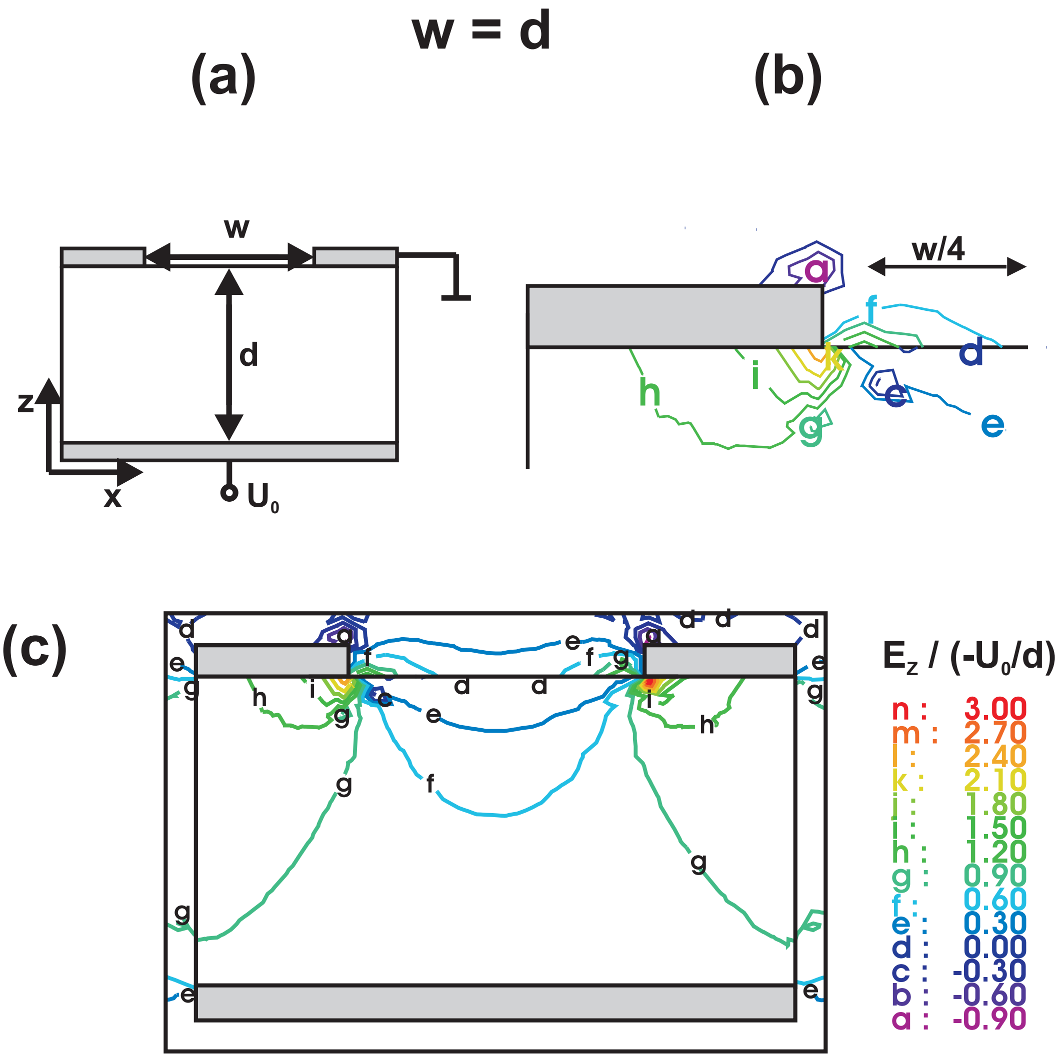

Figure 3.3: Calculations of the normal electric field component in emitter structures. (a) Sketch of a typical electrode structure. Two electrodes, which are indicated in grey, are prepared to a ferroelectric sample of thickness *d* and permittivity $\varepsilon_r = 500$. The top electrode exhibits an aperture of width *w*. A voltage U_0 is applied to the bottom electrode. (b) Detailed depiction of the distribution of E_z for w = d close to the top electrode edges. Equal value lines of E_z are shown normalized to U_0/d. (c) The normal field component is shown for the whole emitter structure

ponent of the electric field E_z has been calculated for a voltage U_0 applied to the bottom electrode by solving the equation

$$\nabla \cdot [-\varepsilon_r \varepsilon_0 \nabla(U)] = 0 \tag{3.2}$$

on the basis of the finite-element method (FEM) with the assumption of no free charges. Equal value lines are shown normalized to U_0/d for different aperture sizes. Figure 3.3 shows the case of w = d. Below the top electrode the field strength corresponds more or less to U_0. Furthermore, a field enhancement close to the electrode edges is clearly visible. For the aperture region two general trends can be seen:

- A reduction of the normal field component for an increasing distance in x-direction from the electrode.
- A reduction of the normal field component for a decreasing distance in z-direction from the surface.

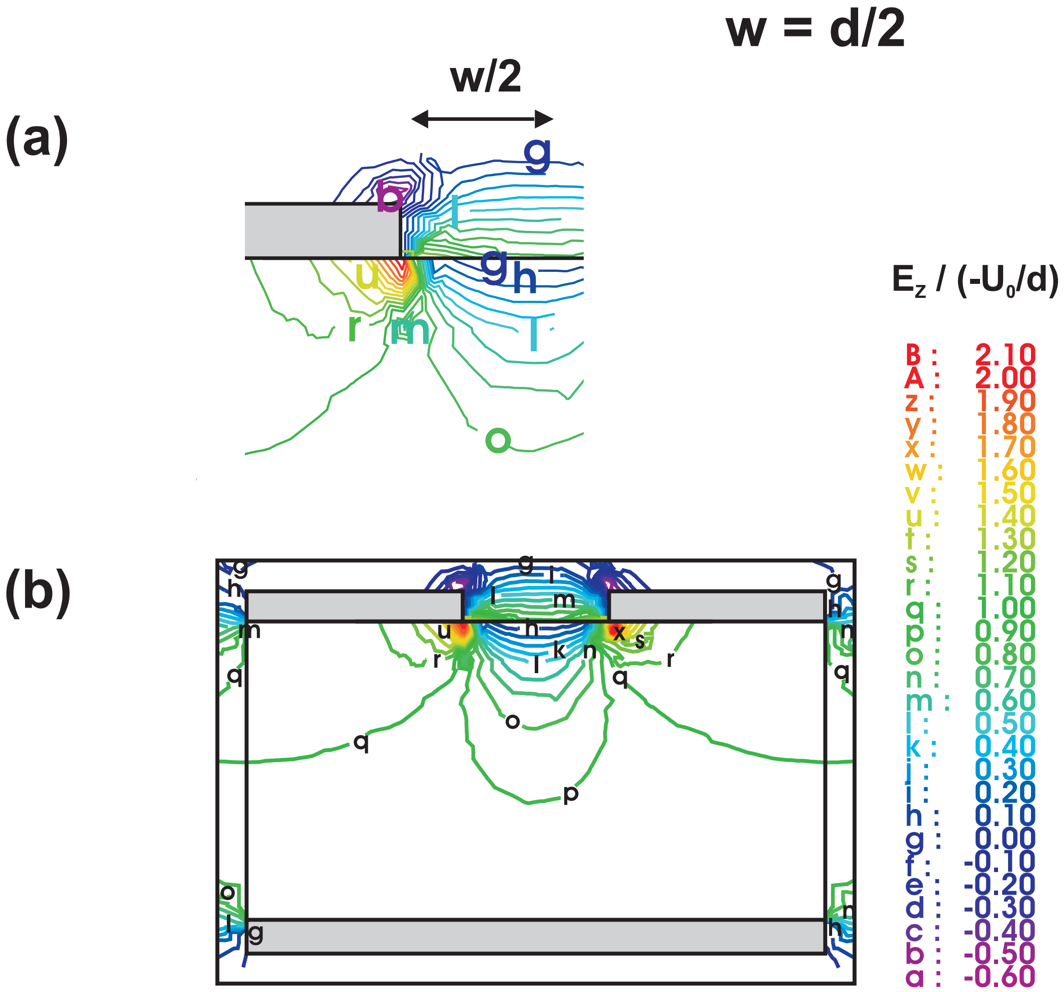

Figure 3.4: Calculations of the normal electric field component for an aperture size of w = d/2. Part (a) shows the distribution of E_z in the aperture region in more detail, whereas Part (b) depicts the normal field component in the complete emitter structure.

Thus, in the free surface area, which is supposed to be the origin of electron emission, E_z is reduced to less than 30 % of the initial electric field strength. Therefore, a direct switching of the ferroelectric polarization in this area will only take place for the application of voltages U_0, which are several times larger than the coercive voltage of the ferroelectric material. For smaller aperture sizes higher values of E_z are present in the free surface region. This can be seen in Figures 3.4 and 3.5, where the normal electric field component is shown for w = d/2 and w = d/10, respectively. In the aperture center field strength of up to 50 % of E_0 are revealed. Accordingly, for smaller aperture sizes a larger fraction of the free surface area can be switched for a certain voltage U_0. This induces a larger polarization variation $\Delta\mathbf{P}$ and increases the probability of electron emission. It is therefore favorable to use gap sizes smaller than the emitter material thickness.

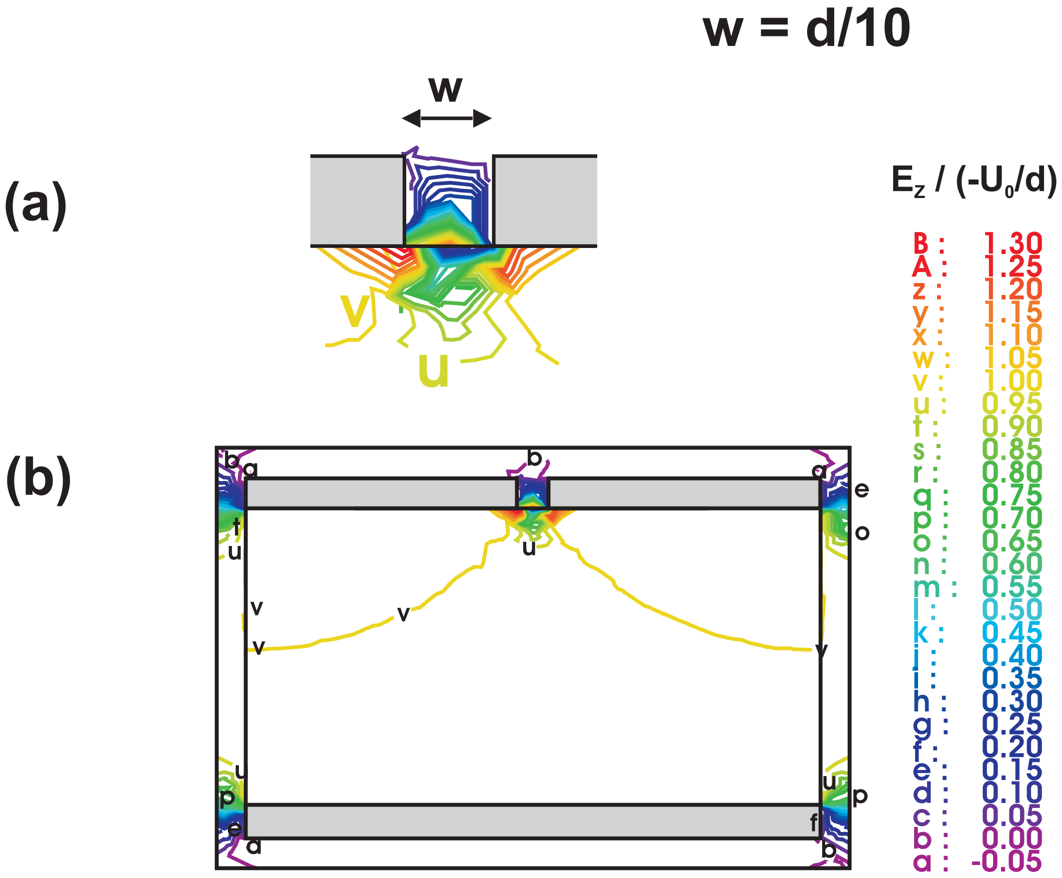

Figure 3.5: Calculations of the normal electric field component for an aperture size of w = d/10. Part (a) shows the distribution of E_z in the aperture region in more detail, whereas Part (b) depicts the normal field component in the complete emitter structure.

To initiate ferroelectric electron emission, it may be sufficient to achieve polarization reversal only in a small fraction of the gap region (see Figure 3.3 (a)). This area will most likely be close to the electrode edges where the applied electric field is enhanced. Moreover, depending on the domain wall mobility, domains of the switched polarization state are able to propagate towards the aperture center, where the electric field strength is below the coercive field [60]. However, in case of inclompete polarization reversal, the screening charges can move to non-switched regions within the aperture. This reduces the repulsive fields, which are induced by the polarization change, and therefore also decreases the achievable electron emission current.

3.3 Strong Ferroelectric Electron Emission

Strong FEE is characterized by significantly larger emission currents than weak FEE. Current densities up to 100 A/cm^2 have been reported [61–63]. This is about 9 orders of magnitude larger than the values reported for weak FEE (see chapter 3.2) and can be explained by a completely different electron emission mechanism. Strong ferroelectric electron emission is initiated by the formation of a surface flashover plasma. Since the propagation of this plasma is driven by horizontal components of the applied electric field, strong FEE is only achieved for a gap free electrode structure shown in Figure 3.2 (b). The surface plasma consists of free charge carriers, i.e. electrons and ions, and spreads out into the aperture region. Thus, the plasma acts as a movable electrode and allows polarization switching in regions more distant from the electrode edges. The free charges of the plasma can easily be emitted into the vacuum by the application of an extraction field.

The plasma can be created in different ways [10]. If a negative voltage pulse is applied to the bottom electrode, weak FEE will be initiated in the top electrode aperture close to the electrode edges. The created electrons are accelerated towards the top electrode. For a positive voltage pulse, field emission can be triggered from the top electrode. In this case, the electrons will move away from the electrode edges. The electron movement parallel to the ferroelectric surface creates more secondary free charge carriers in an avalanching process until a charge neutral plasma is formed which screens the polarization change $\Delta\mathbf{P}$. Another possibility of plasma formation is the exploitation of a field-induced phase transition from a non-ferroelectric to a ferroelectric crystal phase. Examples are relaxor ferroelectric [64, 65] and antiferroelectric materials [58, 66]. A macroscopic spontaneous polarization is only present when a sufficient voltage is applied. In this case, repetitive strong FEE can be operated by monopolar voltage pulses, but the repetition time is limited to the duration of the phase transition, which may be up to several μs [67].

The process of surface plasma formation is not restricted to ferroelectric materials but simply requires the creation of free charges and a polarization variation, which has to be screened. This can also be achieved with paraelectric materials where a dielectric polarization is changed by an applied electric field. Field electron emission from the top electrode provides the free charges required to start the surface flashover process. Since the change of dielectric polarization is restricted to the voltage pulse duration, dielectric electron emitters can be operated by monopolar pulses. The response of dielectric polarization is determined by the frequency of ionic oscillations ($10^{13}\,\mathrm{Hz}$) [10]. Accordingly, much higher repetition rates are possible for dielectric electron emitters than for ferroelectric ones, where the polarization switching time is the limiting factor. However, compared to cathodes, which are based on changes of a ferroelectric polarization, much higher electric fields of about $10 - 25\,\mathrm{kV/cm}$ are necessary to achieve the reported emission currents of several tens of $\mathrm{A/cm^2}$ [57, 68].

The formation of a surface flashover plasma leads to a damaging of the ferroelectric surface and the electrode [69, 70]. This effect limits the lifetime of the cathodes. For PZT ceramics strong ferroelectric electron emission for up to 10^6 switching cycles has been reported [10]. However, the shape of the current pulses changes and the quantity of charges per emission cycle is reduced for proceeding damaging of the emitter structure.

3.4 Thin Film Ferroelectric Electron Emission

Ferroelectric thin films offer the possibility to manipulate the spontaneous polarization with much lower voltages than for ceramics oder single crystals (see Section 2.3) [7]. Accordingly, ferroelectric thin film cathodes should be characterized by low operating voltages, which makes them interesting for a usage in commercial devices. However, the thickness of the emitter material does not only determine the value of the coercive voltage but also essentially influences the electron emission process [10]. This will be explained in the following for the two types of top electrode structures shown in Figure 3.2.

3.4.1 “Plane-to-Plane” Electrode Geometry

In a “plane-to-plane” electrode geometry, which is shown in Figure 3.2 (a), the top electrode and the ferroelectric are separated by a vacuum gap. The whole system can be treated as a plate capacitor filled with two different dielectric media. This is sketched in Figure 3.6 (a). The two electrodes represent the capacitor plates. Medium 1 is given by the vacuum gap. The corresponding thickness and permittivity are the gap size δ and the vacuum permittivity

$\varepsilon_1 = 1$. The ferroelectric with thickness d and permittivity ε_2 represents medium 2, respectively.

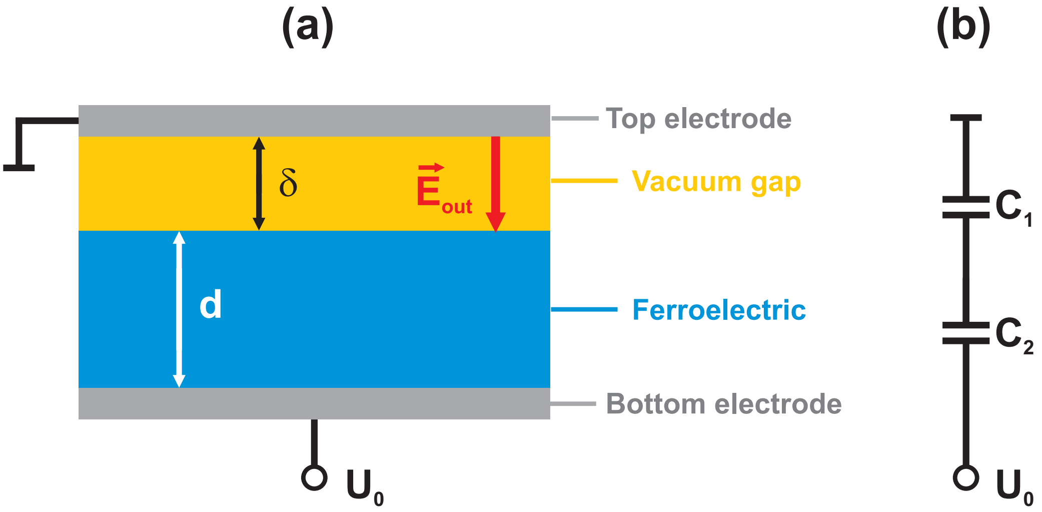

Figure 3.6: Capacitor structure of a "plane-to-plane" electrode geometry. (a) The space between the electrodes is filled by a vacuum gap and a ferroelectric of thicknesses δ and d, respectively. Imbalance surface charges create an electric field E_{out} between crystal surface and top electrode. This field is responsible for subsequent electron emission and is indicated by a red arrow. (b) A series connection of two capacitors as the equivalent circuit of the structure shown in part (a).

The equivalent circuit of this structure is a series connection of two capacitors with corresponding capacitances C_1 and C_2 (see Figure 3.6 (b)). A voltage U_0, which is applied between the two electrodes, splits up in two partial voltages U_1 and U_2 which take effect in the respective capacitor. Thus, only a fraction U_2 of the initial voltage U_0 is actually applied to the ferroelectric material. Using the equations

$$U_{1,2} = \frac{Q}{C_{1,2}} \quad , \tag{3.3}$$

$$C_1 = \varepsilon_0 \cdot \frac{A}{\delta} \quad , \tag{3.4}$$

and

$$C_2 = \varepsilon_0 \cdot \varepsilon_2 \cdot \frac{A}{d} \quad , \tag{3.5}$$

where Q and A are the charge brought on the electrodes and the area of the capacitor, respectively, the ratio U_1 / U_2 can be calculated to be

$$\frac{U_1}{U_2} = \frac{\varepsilon_2 \cdot \delta}{d} \quad . \tag{3.6}$$

With the relation $U_0 = U_1 + U_2$ equation 3.6 can be transformed to

$$U_2 = \frac{U_0}{\frac{\delta}{d} \cdot \varepsilon_2 + 1} \quad . \tag{3.7}$$

Obviously, the voltage fraction U_2 strongly depends on the ratio between gap size δ and material thickness d. The thickness of ferroelectric thin films usually is smaller than 1 μm. Assuming a gap size δ of 10 μm, it can be deduced from equation 3.7 that, for a film with a permittivity $\varepsilon_2 = 100$ and a thickness d of 1 μm, U_2 is only 0.1 % of the initial voltage U_0. Therefore, to achieve a switching of the spontaneous polarization the voltage applied to the electrodes has to be 3 orders of magnitude larger than the coercive voltage. This annihilates any advantage given from the low switching voltages of ferroelectric thin films.

Another value strongly affected by the emitter thickness is the electric field E_{out}, which is present between ferroelectric surface and top electrode (see Figure 3.6 (a)). This repulsive field is created by the polarization variation $\Delta\mathbf{P}$ that is screened by electron emission. Thus, E_{out} determines the probabiltiy of FEE to be initiated and the magnitude of the achieved electron current. It can be expressed as follows [10]:

$$E_{out} = \frac{\Delta P}{\varepsilon_0} \cdot \frac{1}{1 + \frac{\delta}{d} \cdot \varepsilon_2} \quad . \tag{3.8}$$

Apparently, the value of E_{out} is reduced for decreasing thickness of the emitter material. If the sample thickness is reduced from 1 mm to 1 μm for a given $\delta = 10\,\mu$m and $\varepsilon_2 = 100$, the value E_{out} is decreased by a factor of ~ 500. Hence, the achieved emission current for a certain polarization change $\Delta\mathbf{P}$ will be smaller for ferroelectric thin films as compared to ceramics or single crystals.

Equations 3.7 and 3.8 clearly show the difficulties of FEE from thin ferroelectric films for a "plane-to-plane" electrode geometry. Indeed, no results on FEE with this constellation have been reported in the literature so far.

3.4.2 Structured Top Electrodes

Top electrodes which are prepared in direct contact with the ferroelectric material (see Figure 3.2 (b)) are more favorable for thin film emission than "plane-to-plane" electrodes. Since there is no vacuuum gap between electrode and sample, the polarization can be manipulated by low voltages as desired for reduced operation-voltage cathodes. However, the formation of a surface flashover plasma and therefore the appearance of strong FEE should be avoided, because it damages the sample surface. This is even more critical for thin films and leads to a drastically decreased lifetime of the cathode [71]. Non-plasma assisted electron emission from structured top electrodes has been introduced in section 3.2. The electron emission originates in the free surface areas of the electrode, and from the distribution of the normal field component, which is shown in Figure 3.5, it was deduced that, in order to achieve a sufficient field strength close to the surface, the aperture size should be at least smaller than the sample thickness. This means, apertures have to be sub-micrometer sized for thin films.

Most results reported on thin film FEE have used different compositions of PZT [72–74], which are sometimes doped with niobium [75] or cadmium [76], and barium titanate [77]. The material thicknesses ranged from several tens of μm to several hundreds of nm. The top electrodes mainly consisted of striped patterns. The smallest reported aperture size was about $1.5\,\mu$m and thus, still larger than the film thickness [75]. Since only a small fraction of the free surface area was influenced by any applied electric field, only small emission currents ($< 1\,\mu\text{A/cm}^2$) could be measured. For a film thickness larger than several μm, plasma assisted FEE has been shown. This lead to a reduced lifetime of 300 emission cycles.

A different approach is the usage of metal top electrodes, which exhibit small randomly sized ($10\,\text{nm} - 10\,\mu\text{m}$) and distributed microholes [78–80]. These microholes are probably created during the preparation process of the top electrode. Small apertures can also be created by local dielectric breakdown of the sample [71]. However, this kind of electrodes also show small vacuum gaps between metal and ferroelectric, which complicate the field distribution and the emission process.

A possibility to produce regularly arranged periodic apertures of tunable sizes $< 1\,\mu$m in a metal electrode will be presented in Chapter 6.1 and subsequently, the successful demonstration of electron emission from this structures is shown.

3.5 Applications of Ferroelectric Electron Emission

Cathodes based on ferroelectric materials have some distinct properties compared to other electron emitters [10]. This is owned to the unique emission mechanism for FEE, which is caused by alterations of the crystal lattice, i.e.

the spontaneous polarization. In other electron sources the emission is initiated by changes in the electron subsystem of the material. Overbarrier emission is achieved if electrones are excited by an external energy source and eventually overcome the material workfunction. Examples are thermionic and photoelectron emission [3], where the energy is supplied by a thermal heater or a light source, respectively. Tunneling electron emission can be accomplished by a narrowing of the energy barrier of the electrons to increase the tunneling probability through this barrier. For field emission this is done by the application of an external electric field [81].

Ferroelectric electron emitters can be operated in low vacuum conditions ($\sim 10^{-3}\,\mathrm{mbar}$) and require no separate activation process, but have an instant turn-on. Strong FEE provides higher current densities than most other cathode types. The fabrication of ferroelectric materials is not expensive and well established. All these properties give rise to possible applications which employ the FEE effect [10, 24, 52, 82, 83]. Some examples will be explained in the following:

Flat panel displays use the local confinement of FEE. The electron emission is originated in surface areas where the polarization has been varied in a sufficient way. The locally created imbalance charges are directly converted to electron flux. This has been successfully demonstrated for a setup used for weak FEE measurements (see Figure 3.2 (a)) [10, 13]. A structured bottom electrode was prepared to a ferroelectric TGS crystal and the emission current was visualized by a luminescent screen and a CCD camera. The images reproduced the shape of the bottom electrode and thus proved the feasibility to create an emission current with high local resolution. Using an active matrix instead of one single rear electrode would create several local cathodes, each of them acting as a pixel within the whole display device. Resolution limits might be the ability to structure and address very small electrodes and the decreasing absolute emission current value for reduced pixel size.

Ferroelectric cathodes are also used for *microwave generation and amplification* in a wave tube [12, 84]. The high emission current in plasma-assisted ferroelectric emission and the small cross section of the active surface area simplifiy the required focusing system of the electron beam in these devices. Furthermore, current pulse shaping is easily achieved for ferroelectric cathodes by changing amplitude and duration of the trigger voltage pulse.

The high electrostatic fields induced pyroelectrically by a polarization variation have been used to successfully *trigger nuclear fusion* [85]. A lithium tantalate crystal was heated in a deuterium atmosphere. The surrounding gas atoms were ionized and accelerated by the created electric field at the crystal surface. A deuterated target was hit by the ions and by means of nuclear fusion helium and neutrons were generated. A pocket-sized neutron source based on this setup was proposed.

4 Instrumentation and Techniques

This thesis combines measurements of electron emission from ferroelectrics with investigations of the influence of ferroelectric polarization on the emission process. Several experimental techniques were used and will be introduced in this chapter. In the first part, the setup used for electron emission measurements will be explained in detail. The second part describes Piezoelectric Force Microscopy as a technique to image and manipulate the ferroelectric polarization on the nanometer length scale.

4.1 Electron Emission Measurements

Electron emission measurements were performed under ultra high vacuum (UHV) conditions at a pressure of $\sim 10^7$ mbar. The sample was mounted on a goniometer (Panmure Instruments Ltd.) and could therefore be moved in all three directions and rotated about all three axes. Electron emission was measured by channel electron multipliers (MD-402, Amptek, Inc.) and by a metal anode in combination with an amperemeter. A detailed description of the whole setup can be found in reference [86].

The single electron detectors were used to measure small emission currents. Positively and negatively charged particles can be detected. The difference between these two configurations is given by the input voltage applied in front of the detector aperture. This voltage is $+500\,\mathrm{V}$ and $-2400\,\mathrm{V}$ for negative and positive charges, respectively. Secondary electrons, which are created by incoming particles inside the detector tube, are accelerated by an internal voltage of $+2900\,\mathrm{V}$ and measured by a charge sensitive preamplifier. A seperate electronic control box creates a $5\,\mathrm{V}$ output voltage pulse of about $200\,\mathrm{ns}$ duration per detected particle. It is important to know that the system cannot distinguish several particles, which enter the detector tube simultaneously. In addition to the dead time of the amplifier this leads to nonlinearities in the

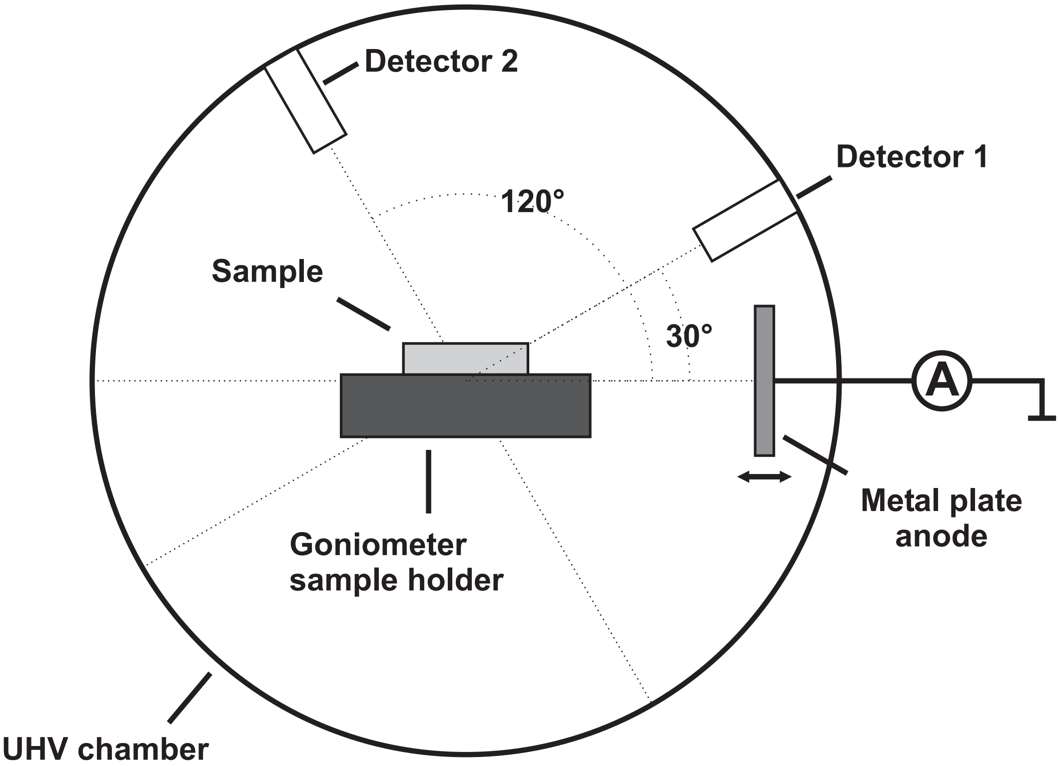

Figure 4.1: Cross section of the setup used for electron emission measurements. The investigated sample is mounted on a goniometer sample holder within a vaccum chamber. Two channel electron multiplier detectors are placed under a respective angle of 90°. A movable metal plate was used as an anode to measure large emission current ($>$ 500 fA) by means of an electrometer.

detector efficiency for count rates $> 10^6\,\mathrm{s}^{-1}$. Figure 4.1 shows a cross section of the vacuum chamber. The two detectors were mounted under a 90 ° angle with respect to each other. Detector 2 was modified by a metal grid placed in front of the detector aperture. This configuration was used to measure the energy distribution of incoming particles. A repulsive dc voltage was applied to this grid and thus, only particles with a sufficient kinetic energy were able to overcome this repulsive field and to be counted by the detector.

On account of the nonlinearities of the channel electron multipliers for higher count rates a second system for emission current measurements was set up. The idea was to measure the emitted current directly. To achieve this, a metal plate was used as an anode to collect incoming charges, which were measured by means of an electrometer (Keithley 617). The resolution limit of the system was $\sim 500\,\mathrm{fA}$. This value turned out to be lower than the upper count rate threshold of the single electron detectors and it was therefore possible to measure small and large emission signals with the combination of the two systems.

4.2 Ferroelectric Domain Imaging and Manipulation

In this work Piezoresponse Force Microscopy (PFM) has been used to investigate the influence of ferroelectric polarization on the electron emission process. PFM is a technique that enables the imaging and manipulation of the ferroelectric polarization on the nanoscale by means of an Atomic Force Microscope (AFM). This microscope belongs to the family of Scanning Probe Microscopes (SPM) that is characterized by a probe which is brought in close proximity or direct contact to the investigated sample [87]. A certain interaction between probe and sample is detected on a very local scale. By scanning the probe across the sample an image of the spatial distribution of this interaction can be obtained. Accordingly, either probe or sample have to be mounted on a xyz-scanning stage, which commonly consists of piezoelectric actuators allowing position control in the sub-nanometer range [88].

For the particular case of an AFM, the probe is a so-called cantilever, which is able to detect very small forces [89]. The cantilever is clamped at one end, whereas the other end carries a sharp tip. If this tip is approached to the sample, attractive or repulsive interactions lead to a deflection of the cantilever [90, 91]. The displacement of the probe carries information on the distance between cantilever and sample and can be measured in different ways, but the most common choice is an optical detection, where a laser beam is focused on the rear side of the cantilever and the reflected beam is measured by means of an interferometer or a four-quadrant photodiode [92–94]. The latter case is shown in Figure 4.2.

A variation of the cantilever deflection leads to a displacement of the reflected laser spot and subsequently -via a feedback loop- the tip height is adjusted by the z-scanner to keep the deflection at a constant setpoint level. This way, the recorded movement of the z-scanner reveals the sample topography.

Two main operation modes of an AFM are possible. The so-called contact and non-contact modes. In the contact mode the canitlever tip is brought in direct contact with the sample. Repulsive forces lead to a bending of the lever. The actual displacement depends on the applied force and the cantilever spring constant and is a direct measure of the sample topography. In contrast, in the non-contact mode the tip is brought in close proximity to the sample surface. There, attractive forces are present, similarly causing a cantilever deflection. If the cantilever is oscillating, usually close to its resonance frequency, the mode is called dynamic non-contact mode. The interaction forces with the sample influence this oscillation by a damping of the oscillation amplitude and a shift

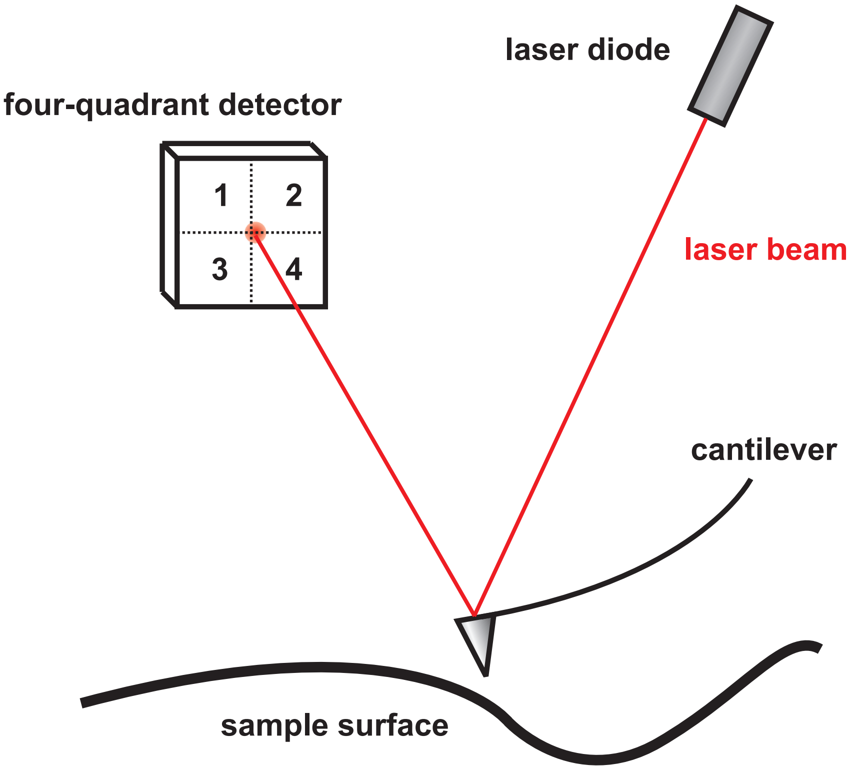

Figure 4.2: Optical detection in an Atomic Force Microscope. A laser beam is focused on the rear side of a cantilever. A four-quadrant diode measures the reflected beam, which carries information on the cantilever deflection [95].

of the system resonance frequency. Both effects can be used as feedback signal to control the tip height. This measurement mode provides the highest lateral resolution.

4.2.1 Domain Imaging

For Piezoresponse Force Microscopy, an AFM is operated in contact mode [96–99]. A conductive cantilever is needed, since a voltage is applied between tip and a bottom electrode underneath the sample. As all ferroelectrics are simultaneously piezoelectric (see Figure 2.1) this voltage induces a local mechanical deformation Δx of the sample volume below the tip due to the converse piezoelectric effect. This deformation can be written as follows:

$$\Delta x_j = d_{ij} E_i \qquad (4.1)$$

$$\text{with i} = 1...3 \text{ and j} = 1...6 \quad .$$

E_i denotes the component of the applied electric field and d_{ij} represents the piezoelectric tensor written in the Voigt notation [100]. Actually, the piezoelectric tensor d_{ikl} is of third order. However, using the symmetry of $d_{kl} = d_{lk}$ it is possible to simplify the kl-matrix to a 6-dimensional vector using the following relation:

$$d_j = d_{kl} \quad , \quad \text{(j = 1...6 and k,l = 1...3)} \tag{4.2}$$

with

$$j = k\delta_{kl} + (1 - \delta_{kl})(9 - k - l) \quad . \tag{4.3}$$

The crystal symmetry of the sample determines which elements of the d_{ij} tensor are non-zero. If the electric field is applied in x_3 = z direction, the most important components, however, are d_{33} and d_{15} for a polarization orientation perpedicular and parallel to the sample surface, respectively.

Since the AFM is operated in contact mode, the sample deformation is directly transmitted to the cantilever and the resulting deflection is measured by the position-sensitive detector. Figure 4.3 shows the principle of a PFM measurement. In parts (a) and (b) the polarization is oriented perpendicularly to the sample surface, i.e. in z-direction. If a voltage is applied between AFM tip and sample-bottom electrode, the component d_{33} leads to a sample deformation in z-direction. The four-quadrant diode detects this deformation (see Figure 4.2). Substracting the signals of the third and fourth quadrant from the signals of the first and second ones ((1+2)-(3+4)) reveals a variation of the cantilever bending. Thus, this so-called out-of-plane or z-signal carries information on the polarization component which points out of the surface plane. It is also visible that the direction of the piezoelectric response depends on the polarization orientation along the z-axis.

In Figures 4.3 (c) and (d) the polarization is oriented within the surface plane and perpendicularly to the cantilever (x-direction). The tensor component d_{15} induces a shear motion of the sample and subsequently of the AFM probe, which is also resolved by the detector. The signal difference of the odd and even quadrant numbers ((1+3)-(2+4)) reveals a signal change in x-direction. This signal will be referred to as in-plane or x-signal in the following.

If the polarization lies in the surface plane but is oriented parallel to the cantilever axis (y-direction), the situation is different. This case is sketched in Figures 4.3 (e) and (f). Again, the piezoelectric tensor component d_{15} induces a shear motion, but this deflection of sample and tip leads to a buckling of the cantilever and is not resolved by the x-signal but the z-signal of the detector. Therefore, it superimposes the signal measured for a polarization being oriented in z-direction. A possible way to distinguish these two signals is to rotate the sample about 90 ° [101]. However, due to the different mechanisms causing the cantilever deflection, the out-of-plane component of the polarization usually yields to a much higher variation in the z-signal and the contribution of the in-plane polarization component can be neglected.

For the case of an ac voltage V_{ac} applied between tip and bottom electrode, the sample oscillates with the voltage frequency f and the detected deflections can be written as

$$\Delta z \propto d_{33} sgn(P_3) V_{ac} \sin(\omega t) \tag{4.4}$$

and

$$\Delta x \propto d_{15} sgn(P_1) V_{ac} \sin(\omega t) \quad , \tag{4.5}$$

if the contributions of the polarization component, which is oriented in the surface plane and parallel to the cantilever are neglected [98]. P_3 and P_1 denote the polarization components pointing in z and x-direction, respectively. V_{ac} and $f_{ac} = \frac{\omega}{2\pi}$ are the amplitude and frequency of the applied ac voltage. From equations 4.4 and 4.5 can be seen that the amplitude, which is proportional to the respective tensor element, of the detected oscillations is a measure of the polarization magnitude, whereas the phase carries information on the polarization direction. Domains pointing antiparallel are distinguished by a 180 ° phase difference according to the *sgn*-function. Using lock-in amplifiers, amplitude and phase of the cantilever oscillations in z and x-direction can be extracted simultaneously and thus, by scanning the tip across the sample, a complete map of the domain distribution, containing information on the polarization magnitude and orientation, can be recorded. The resolution is solely limited by the tip radius. Values of 5 nm resolution have been reported [102].

The cantilever oscillations in PFM are induced by the piezoelectic tensor components and therefore, the ferroelectric polarization is measured indirectly. The correlation of these two measures is, in most cases, non-linear and even not univocal for several materials. Furthermore, in reality the polarization will not be oriented completely either in z or x-direction. This may be caused by the crystal structure of the sample, e.g. in a rhombohedral crystal phase (see Figure 2.2), or due to polycrystallinity of the sample, or if the sample is mounted with some tilt angle with respect to the AFM tip. Hence, it is difficult to obtain quantitative values of the spontaneous polarization. Complete knowledge of the crystal orientation and the correlation between the piezoelectric coefficients and the spontaneous polarization is required [103, 104]. Moreover, the particular properties of the cantilever influence the measured signal amplitude [105].

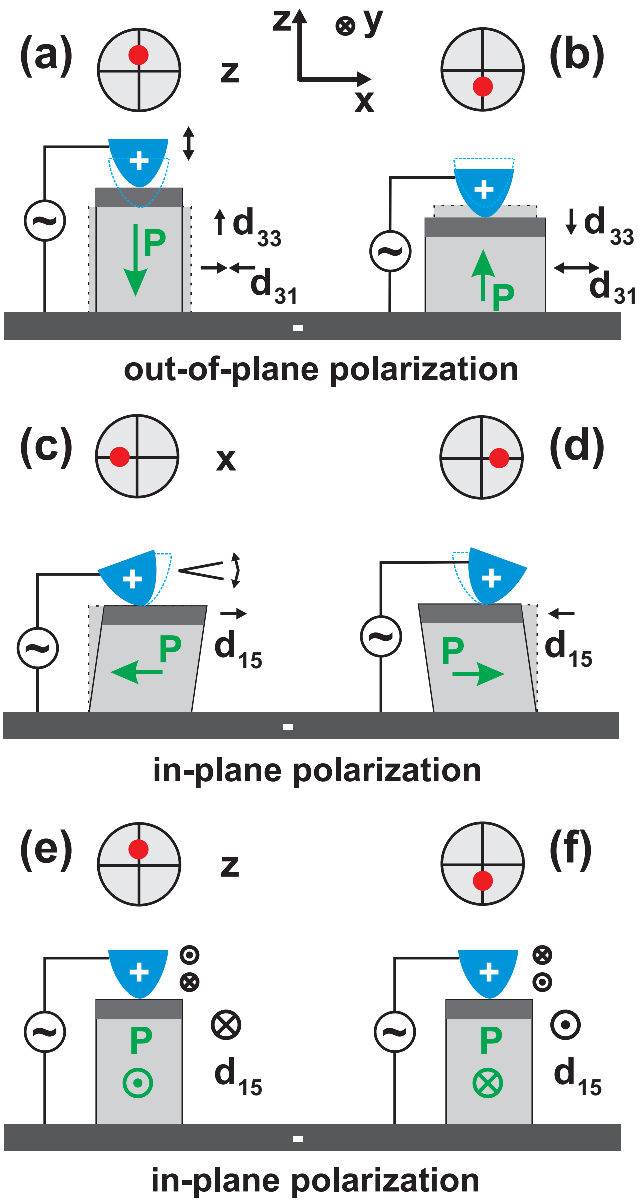

Figure 4.3: Principle of PFM Measurements. The AFM tip indicated in blue is in direct contact with the sample and an ac voltage is applied between the cantilever and a bottom electrode. The orientation of the spontaneous polarization **P** with respect to the applied electric field **E** determines the mechanical stress, which is induced to a sample volume below the probe due to the converse piezoelectric effect. (a) and (b): **P** is oriented along the field axis. The d_{33} component of the piezoelectric tensor induces either an expansion or a contraction in z-direction. The direction depends on the polarization orientation. Additionally, a contraction or expansion in x-direction is caused by the tensor component d_{31}. The cantilever motion is resolved by the detector as a signal change in z-direction. (c) - (f): The polarization is perpendicular to **E**. A shear motion is induced by d_{15}. For **P** pointing in x-direction, the cantilever deflection is detected as a signal variation in x-direction. In contrast, a polarization orientation in y-direction leads to a change of the z-signal [16].

Electrostatic interactions between AFM tip and sample cause an oscillation of the tip with the frequency f of the applied voltage U_{ac} and are therefore competitive to the converse piezoelectric effect. For high contact forces applied on the tip the electrostatic signal is decreased and the detector signal is caused by the piezoelectric interaction only [105, 106]. However, this leads to an increased tip radius and consequently to a loss of spatial resolution.

The measurements presented in this work were performed with a commercially available AFM (Explorer™, TopoMetrix Corp., US). This stand-alone AFM is characterized by the special feature of a movable tip and a maximum scan range of 100 μm.

4.2.2 Domain Manipulation

An AFM is not only appropriate for imaging the ferroelectric polarization but can also be used to manipulate the domain state on the nanoscale. If the voltage applied between bottom electrode and cantilever is larger than the coercive voltage, the polarization in the sample volume below the tip will be reversed [107, 108]. By scanning the tip across a certain area, it is possible to create any desired domain structure at least for out-of-plane oriented domains. Furthermore, the switching behavior can be investigated. Measuring the PFM-signals written in equations 4.4 and 4.5 with a variable dc voltage applied simultaneously with the PFM probing voltage, allows the record of piezoelectric hysteresis curves [103]. From this loops the local coercive voltages can be obtained. This technique provides insight in the spatial and energy distribution of nucleation centers [109].

The switching of ferroelectric polarization was also investigated on a macroscopic scale. For this, a ferroelectric test system (TF Analyzer 2000, Aixacct GmbH, Germany) was available, which was able to apply a voltage ramp and measure the current flow through a sample. A current peak appears at the coercive voltage where the polarization is switched. Integration of this current peak leads to a hysteresis loop of the ferroelectric polarization. The lateral resolution of this method is determined by the size of the electrodes used to contact the material.

5 Electron Emission from PMN-PT Single Crystals

Due to its low coercive field and high remanent polarization, lead magnesium niobate - lead titanate (PMN-PT) is a promising candidate for low voltage electron emission. This chapter presents experiments, in which current densities up to $10^{-5}\,\mathrm{A/cm^2}$ *have been achieved for extraction fields measuring less than* $4\,\mathrm{kV/cm}$. *The first part describes the preparation of a top electrode on the investigated single crystals. It is followed by a profound investigation of the dependence of the electron emission on the amplitude, frequency and shape of the applied extraction voltage. The influence of polarization switching is discussed in the third section, whereas the kinetic energy distribution of the emitted electrons is presented in the fourth part of this chapter. Finally, the surface conductivity of the emitter structure was investigated and found to be a limiting factor of the emission current for high voltage frequencies.*

5.1 Sample Preparation

$\mathrm{Pb(Mg_{1/3}\,Nb_{2/3})O_3}$ - $\mathrm{PbTiO_3}$ (PMN-PT) is a relaxor ferroelectric as described in Section 2.4. This material was chosen for electron emission experiments because of its low coercive field of $\sim 2\,\mathrm{kV/cm}$, which promises low operation voltages. Furthermore, PMN-PT exhibits a large spontaneous polarization of several tens of $\mu\mathrm{C/cm^2}$, which is a precondition for large achievable emission currents. The purchased samples were (001)-oriented single crystals and both crystal surfaces were covered with solid gold electrodes. To achieve an electrode structure, appropriate for electron emission experiments, the top face of the sample was polished and a customized top electrode structure was prepared, which can be seen in Figure 5.1.

A thin wire with a diameter of $25\,\mu\mathrm{m}$ was used as a mask and positioned on top of the sample surface. Subsequently, the structure was evaporated with 5 nm and 60 nm thick layers of chromium and gold, respectively. As a

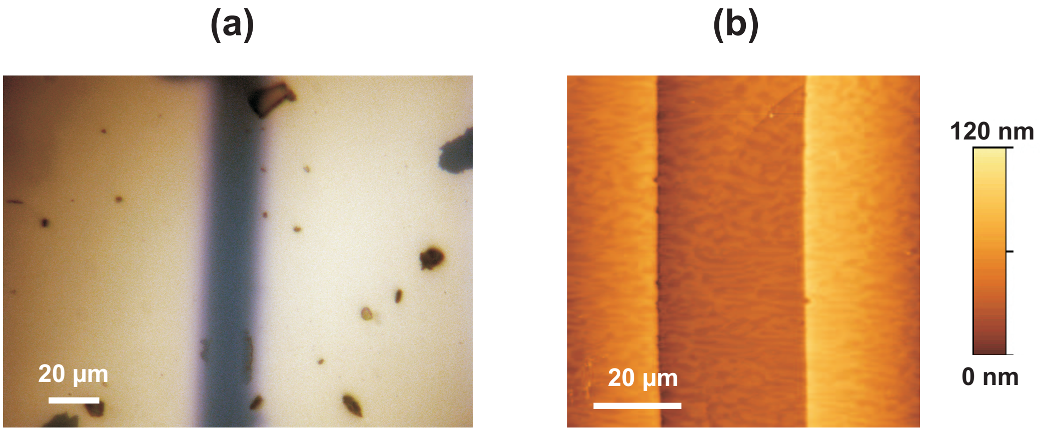

Figure 5.1: Top electrode structure of PMN-PT samples. The two parts of the top electrode are separated by a 25 μm wide slit, which is shown in the image centers. Image (a) is obtained by means of an optical microscope, whereas image (b) shows the sample topography recorded with an atomic force microscope.

result, a top electrode structure consisting of two parts, which were separated by a 25 μm wide slit, was created. Thus, electrical contact could be applied independently to each part of the electrode, which all in all covered an area of about 8 mm^2 of the sample surface.

The free surface area between the two components of the top electrode represents the aperture within the electrode structure shown in Figure 3.2 (b) and is therefore supposed to be the origin of a electron emission current. The aperture width of 25 μm is small compared to a sample thickness of around 400 μm and reasonable normal components of the applied electric field should be present within the free surface region as can be obtained from Figure 3.5.

5.2 Dependence on Voltage Amplitude and Frequency

For electron emission measurements the elements of the top electrode were connected and put on ground potential, whereas an ac voltage was applied to the bottom electrode. The wiring scheme can be seen in Figure 5.2. The ac voltage induced a periodic polarization variation and a steady emission current could be recorded.

5.2.1 Single Electron Detector Measurements

During these electron emission measurements the voltage amplitude U_0 was varied at a constant frequency. The resulting emission signal was measured by

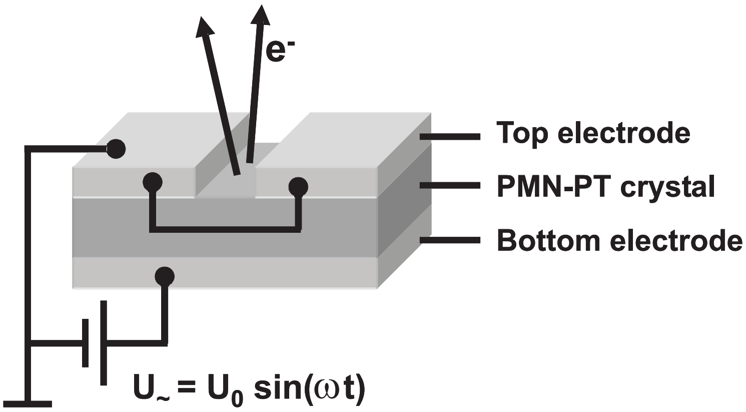

Figure 5.2: Wiring scheme for electron emission experiments. The two parts of the top electrode were put on ground potential and an ac voltage of variable frequency and amplitude was applied to the bottom electrode. Electron emission is originated in the aperture region.

Detector 1, which was operated with an integration time of 1 s. In Figure 5.3 the observed count rate, which has been averaged over several hundreds of data points, can be seen as a function of the voltage amplitude for an excitation frequency of 1 kHz.

The black curve has been achieved using a sinusoidal voltage, whereas the blue graph corresponds to a square wave excitation voltage. Compared to a sinusoidal voltage, a square wave exhibits a much smaller rise time of the maximum voltage value U_0 and a faster variation of ferroelectric polarization. This should result in a higher field strength at the sample surface, and thus a larger electron emission is expected. Both curves show a general increase of the emission signal for rising voltage amplitudes. Higher voltage amplitudes lead to a larger polarization variation and consequently to more imbalance surface charges. In both experiments, the measured count rate for values of $U_0 < 60\,\mathrm{V}$ was hardly above the resolution limit of the detector. For instance, a small signal of about 20 counts/s was recorded at about 25 V with a sinusoidal excitation voltage. A significant enhancement of the count rate can be seen for voltages $> \sim 80\,\mathrm{V}$.

The blue graph shows a saturation level of approximately 70000 counts/s for a voltage amplitudes larger than 95 V. Apart from this saturation, higher emission signals are revealed for a square wave excitation voltage compared to a sinusoidal one at a given voltage amplitude, as has been expected. Measurements of the emission current by means of an electrometer are presented in Section 5.2.2 and proove that the saturation of the count rate is caused by non-linearities in the detector efficiency. As mentioned previously, the rise time of the voltage is much shorter ($\sim 4\,\mu$s) for square waves. Therefore, the subsequent emission of electrons is supposed to be intiated and completed within a smaller period than for a sinusoidal excitation voltage. The detector is not able to measure all electrons coming in within this period for reasons discussed in Section 4.1. Thus, the count rate observed for the 1 kHz square wave voltage is underestimated, whereas no such pronounced saturation is measured for a sinusoidal excitation voltage, where the emission process is extended over a longer time span. Obviously, for high count rates the single electron detector resolution is limited and the emission behavior is not measured reliably.

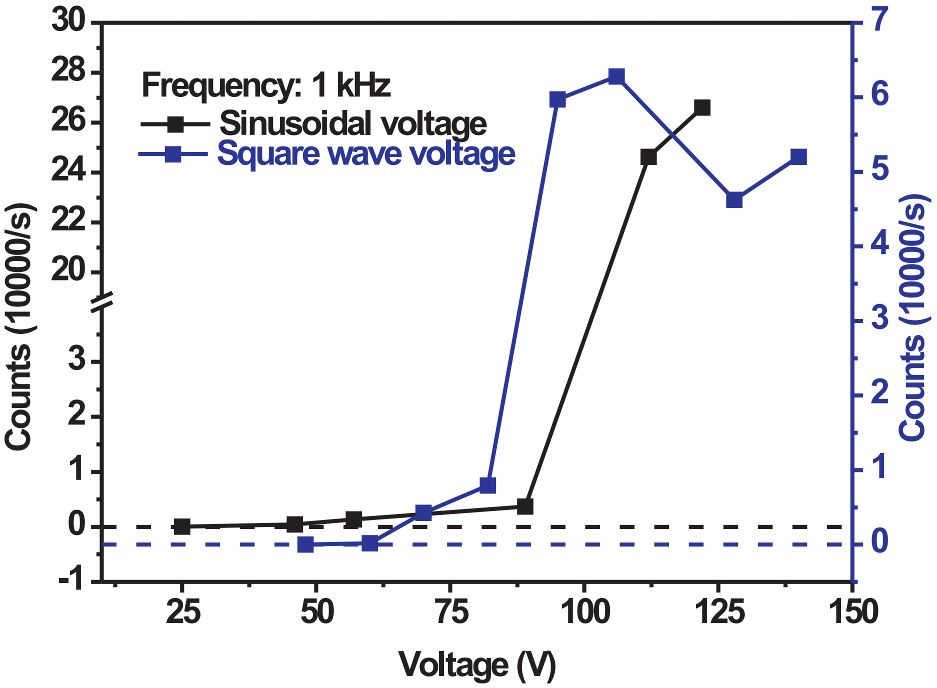

Figure 5.3: Single electron detector measurements. Electron emission from PMN-PT single crystals observed by a channel electron multiplier as a function of the applied voltage amplitude U_0. The black and the blue curve correspond to a sinusoidal and a square wave emission voltage of 1 kHz frequency, respectively.

The frequency dependence of the electron emission can be seen in Figure 5.4. For the count rate, a logarithmic scale was chosen to better visualize the behavior of small signals. Part (a) shows the results obtained by the application of a sinusoidal voltage.

The black, blue, and red curves represent measurements with a voltage frequency of 1 kHz, 100 Hz, and 10 Hz, respectively. The black graph corresponds to the measurement also shown in Figure 5.3. The signals obtained for lower

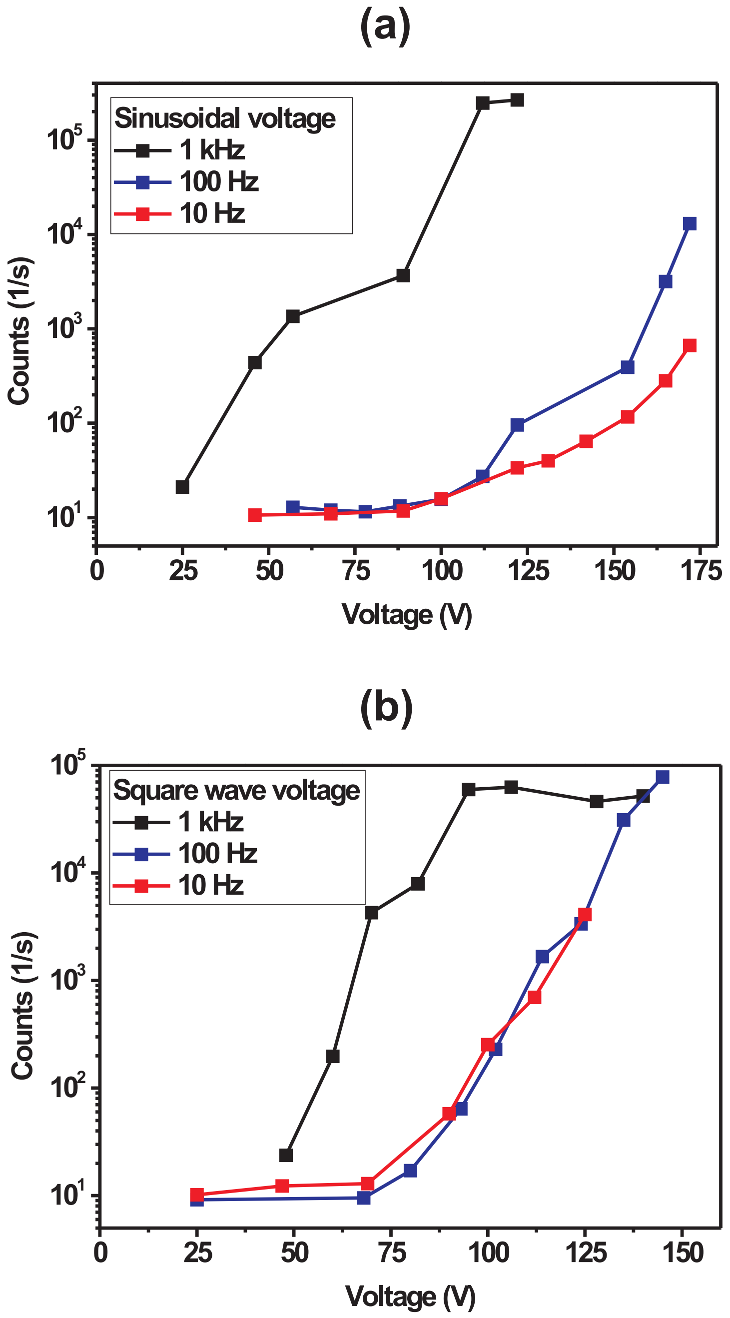

Figure 5.4: Frequency dependence of electron emission. Electron emission from PMN-PT single crystals observed by a channel electron multiplier as a function of the applied voltage amplitude U_0. The recorded signals are shown on a logarithmic scale. (a) Results achieved with a sinusoidal excitation voltage. The black, blue and red curve correspond to voltage frequencies of 1 kHz, 100 Hz and 10 Hz, respectively. A strong signal increase for $U_0 > 80$ V can be seen for all graphs. (b) For comparison, a square wave voltage was used to intitiate electron emission for the same frequencies as shown in Part (a). The observed signals are not directly proportional to the voltage frequency. This is particularly obvious for the 100 Hz and 10 Hz experiments.

frequencies reveal a generally smaller emission signal than for the 1 kHz measurement. For $U_0 < 80\,V$ the observed count rate was below the detector resolution limit, but remarkably, the signal strength is not directly proportional to the excitation frequency. A linear correlation between the number of switching cycles, which is determined by the frequency, and the observed count rate is expected, assuming the same amount of emitted charges per polarization reversal. However, this seems not be the case and gets particularly obvious when comparing the signals measured with a frequency of 100 Hz and 10 Hz in the voltage regime $U_0 < 120\,V$. There, the recorded count rates are almost equal. Moreover, the rise time of the voltage strongly depends on the frequency for a sinusoidal excitation. Accordingly, the amount of emitted charges for a single switching cycle should be smaller for decreasing frequencies. In Section 7.3 it will be shown that the variation of the ferroelectric polarization is larger for smaller frequencies, which explains the similar count rates measured for the 100 Hz and 10 Hz voltages. Moreover, the emission process is finished after a period of several hundreds of milliseconds, as will be revealed in Section 5.3.1. Thus, a faster reorientation of the polarization leads to an incomplete emission of imbalance surface charges and the current will be smaller for higher excitation frequencies.

In Figure 5.4 (b) the emission signal achieved with a square wave excitation voltage can be seen for frequencies of 1 kHz, 100 Hz, and 10 Hz, which are again depicted as a black, blue and red curve, respectively. Similarly to the results shown in Part (a), the count rates obtained with a 100 Hz and 10 Hz voltage are almost equal but smaller than for a 1 kHz excitation. This is even more pronounced, since the rise time of the voltage is constant for all frequencies for a square wave and thus, no reduction of the emitted charges per switching cycle is expected. Remarkably, no saturation of the emission signal can be seen for frequencies < 1 kHz. Actually, the 100 Hz signal gets even larger than the 1 kHz signal for $U_0 > 140\,V$. Accordingly, this effect is not solely caused by non-linearities in the detector efficiency but also related to the faster reorientation of the ferroelectric polarization. This will be discussed in more detail in Section 5.5, where it is shown that the electron emission current is limited by the surface conductivity of the sample. For high excitation frequencies the amount of charges flowing from the electrodes to the free surface area is not sufficient to completely screen the depolarization field. Thus, the achievable electron emission current is limited for high frequencies. This can be seen in Figure 5.4 (b), where the count rate is saturated for the 1 kHz measurement only.

5.2.2 Emission Current Measurements

In a further experiment (see Section 4.1) the emission current was measured directly. In Figure 5.5 the recorded emission current can be seen as a function of the excitation voltage amplitude. Each measurement was averaged over several minutes to annihilate artifacts caused by the capacitance of the anode-sample system. The black and the blue curve correspond to the results obtained with a 1 kHz sinusoidal and square wave voltage, respectively.

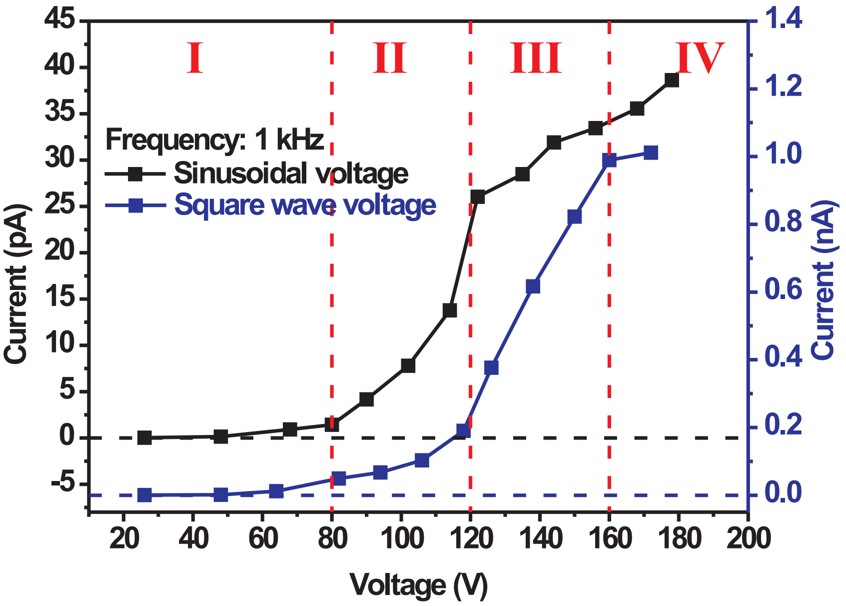

Figure 5.5: Regimes of electron emission. The electron emission current obtained for a 1 kHz excitation voltage is shown as a function of the voltage amplitude. The black and the blue curve correspond to a sinusoidal and a square wave emission voltage, respectively. The vertical dashed red lines mark the threshold voltages between the identified emission regimes, which are labeled by the red numbers. The horizontal dashed lines represent the zero current levels of the respective curves.

The measured current values for voltage amplitudes < 80 V are very small and hardly above the resolution limit of the electrometer. For higher values of U_0 a rising current was recorded for increasing voltages. The slopes of the curves increase up to 120 V. From there on, a constant slope is visible for both graphs. The maximum current values are 40 pA and 1 nA for a sinusoidal and square wave excitation, respectively. In contrast to the count rates observed by the single electron detector (see Figure 5.3), the current measured directly is always larger for a square wave voltage than for a sinusoidal one. Thus, the count rate saturation for $U_0 > 95\,\mathrm{V}$ obtained with the detector can be indeed related to non-linearities in the detector efficiency, as discussed above. However, the blue curve reveals a reduced current increase for voltage amplitudes $> 160\,\mathrm{V}$.

Generally, four regimes of electron emission could be identified, which are indicated by the red numbers in Figure 5.5. The first regime takes place for voltage amplitudes $< 80\,\mathrm{V}$ and is characterized by small emission currents. It will be clarified in Section 5.3 that the second regime is initiated by the onset of complete polarization switching between top and bottom electrode. The electron emission is strongly enhanced with an increasing slope for rising voltage amplitudes. For $U_0 > 120\,\mathrm{V}$ a linear dependence of the emission on the voltage amplitude can be observed. In this third regime the polarization is reversed in the entire area of the top electrode aperture, as will be shown in Section 7.4. Thus, the sample area, from which the electron emission originates, is constant and the increase of the current is caused by the larger polarization variation for higher voltages only. The fourth emission regime sets in for voltages higher than 160 V for a square wave excitation and is characterized by a much smaller increment of the current. This saturation is caused by the limited supply of screening charges that are brought on the sample surface between the emission pulses, as will be discussed in Section 5.5.

The emission current was also recorded for an excitation frequency of 100 Hz, as is shown in Figure 5.6. The measured current can be seen on a logarithmic scale as a function of the voltage amplitude U_0. As a comparison, the results presented in Figure 5.5, which have been achieved with a 1 kHz excitation, are also depicted.

Similar to the count rates measured by means of the single electron detector (see Figure 5.4), the difference between the signals obtained with a 1 kHz and a 100 Hz voltage is more pronounced for a sinusoidal exciation than for a square wave, which can be attributed to the larger rise time of a sinusoidal voltage for lower frequencies. The maximum current achieved for a 100 Hz square wave of 180 V was about 200 pA, whereas only 2.5 pA were measured for a sinusoidal voltage of the same frequency. This corresponds to 20 % and 6 % of the maximum current measured with an excitation voltage of 1 kHz for a square wave and a sinusoidal voltage, respectively. Accordingly, the amount of charges being emitted during a single switching cycle is enhanced for a square wave and reduced for a sinusoidal excitation.

Summarizing the results presented in this section, the following important characteristics of electron emission from PMN-PT single crystals can be listed:

- Four different regimes of electron emission can be identified. In Sec-

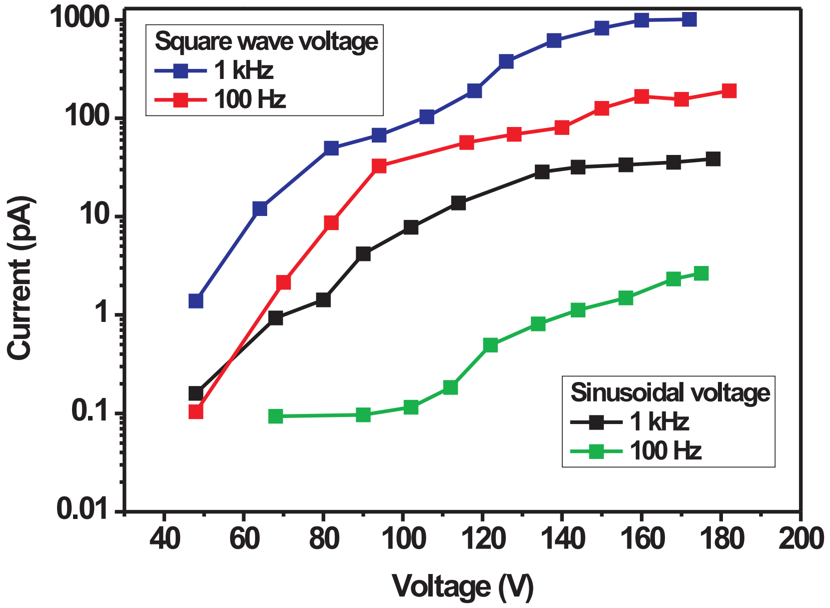

Figure 5.6: Frequency dependent electron emission current measurements. The current was measured directly by means of an electrometer and is shown in a logarithmic scale as a function of the voltage amplitude. A sinusoidal and a square wave voltage were applied to the sample bottom electrode, each with frequencies of 1 kHz and 100 Hz. The black and the blue curves correspond to the measurements shown in Figure 5.5.

tions 5.3 and 7.4 the impact of the ferroelectric polarization on the onset of the different regimes will be elucidated.

- The rise time of the applied voltage influences the magnitude of the emission current. The application of a square wave voltage results in higher emission signals than a sinusoidal one. A faster polarization variation leads to higher repulsive electric fields on the sample surface and the probability of competitive effects, like compensating currents from the top electrode, is reduced.

- A saturation level of the emission current was observed for high voltage frequencies and seems to represent a limit of the highest achievable current. It is partially determined by the surface conductivity of the sample, as is dicussed in Section 5.5.

- The highest achieved emission current was about 10^{-9} A. Taking the aperture as the active area, where the electron emission originates from, this corresponds to a current densitiy of $5 \cdot 10^{-5}\,\mathrm{A/cm^2}$. The extraction voltage was 160 V, resulting in an applied field of 4 kV/cm.

- The number of emitted charges is not constant for different voltage frequencies. This can be seen in Figure 5.4, comparing the measurements at 100 Hz and 10 Hz. The origin of this effect is found in the mechanism of polarization reversal. In Section 7.3 it is shown that the switched polarization charge is reduced for an increasing voltage frequency. Thus, less screening charges are present close to the sample surface, resulting in a reduced emission current.

5.2.3 Nature of the Electron Emission Process

The highest achieved current densities of $5 \cdot 10^{-5}\,\mathrm{A/cm^2}$ does not allow a categorization of the electron emission presented in this Section, since this value can be attributed to a weak FEE as well as to a strong FEE, which were introduced in Sections 3.2 and 3.3, respectively. However, no indications of the formation of a surface flashover plasma could be found. Such a plasma contains both positively and negatively charged particles. No emission of positive charges could be detected for all applied voltage amplitudes and frequencies. Moreover, the typical damage of the sample and electrode surface, which is usually caused by a surface plasma, was absent. The lifetime of the samples strongly depended on the magnitudes of the applied voltages, but was solely limited by the high piezoelectric coefficients of PMN-PT. For voltages larger than $\sim$ 150 V the generated mechanical stress leads to cracking of the top electrode or mechanical breakdown of the crystal. This causes shortcircuits between top and bottom electrode or at least changes the capacitance of the emitter structure and equally the effective area responsible for FEE. Hence, the FEE process becomes unreliable being reflected in large emission signal fluctuations. However, for moderate voltage amplitudes the operation time of the PMN-PT crystals was at least up to 10^9 switching cycles. It is therefore believed that no surface plasma is involved and that the results presented in this section can be attributed to a weak FEE mechanism.

5.3 Influence of Ferroelectric Polarization

5.3.1 Polarization Orientation

In order to prove the ferroelectric nature of the measured emission signal, a square shaped voltage of 10 mHz frequency and 170 V amplitude, which was sufficient to initiate a switching of the spontaneous polarization, was applied to the bottom electrode. The count rate obtained by the detectors was correlated to the currently applied voltage state. A positive voltage corresponds to an orientation of the out-of-plane polarization component in positive z-direction, i.e. out of the sample surface. Accordingly, the polarization is directed in negative z-direction for a negative bottom electrode voltage. The low frequency made it possible to interrelate the measured emission signal to the two possible switching events between the mentioned polarization states.

The result is depicted in Figure 5.7 (a). Applied voltage and recorded detector signal are plotted as a function of the elapsed time with a resolution of 10 ms It is clearly visible that the electron emission is restricted to the transition from a positive to a negative voltage applied to the bottom electrode. At this transition the polarization is reversed from a +z to a -z orientation, i.e. from pointing upwards to downwards, as shown in Figure 3.1. This switching event leads to negative imbalance surface charges and subsequently to an emission of electrons, which has been measured by the detector. In contrast, no ferroelectric electron emission is expected for a polarization switching from -z to +z direction, where positive surface charges are present. The observed absence of electron emission at the transition from a negative to a positive voltage therefore indicates that the measured electron emission is induced by a variation of the ferroelectric polarization.

Another possible emission mechanism would be field emission from the top electrode. However, this process would take place if the top electrode was biased negatively, i.e. a positive bottom electrode voltage. Since no signal was measured in this case, tis process can be ruled out. Moreover, field emission means a steady state current. The short period of emission measured in Figure 5.7 indicates a transient mechanism, like ferroelectric electron emission, being responsible for the observed signal.

Figure 5.7 (b) shows a single electron emission event from part (a) with a higher time resolution. Again, the voltage, which was applied to the bottom electrode, and the measured count rate are depicted as a black and a red curve, respectively. It is clearly visible that the electron emission, which is triggered by the transition from a positive to a negative bottom electrode voltage, is completed after a period of about 300 ms. Furthermore, two peaks of the count rate can be seen. The first one is initiated directly after the voltage transition and decayed after about 100 ms. The second peak occurs about 200 ms after the application of a negative voltage.

The reason for the two distinct emission pulses can be found in the dynamics of ferroelectric polarization. Several polarization switching mechanisms are

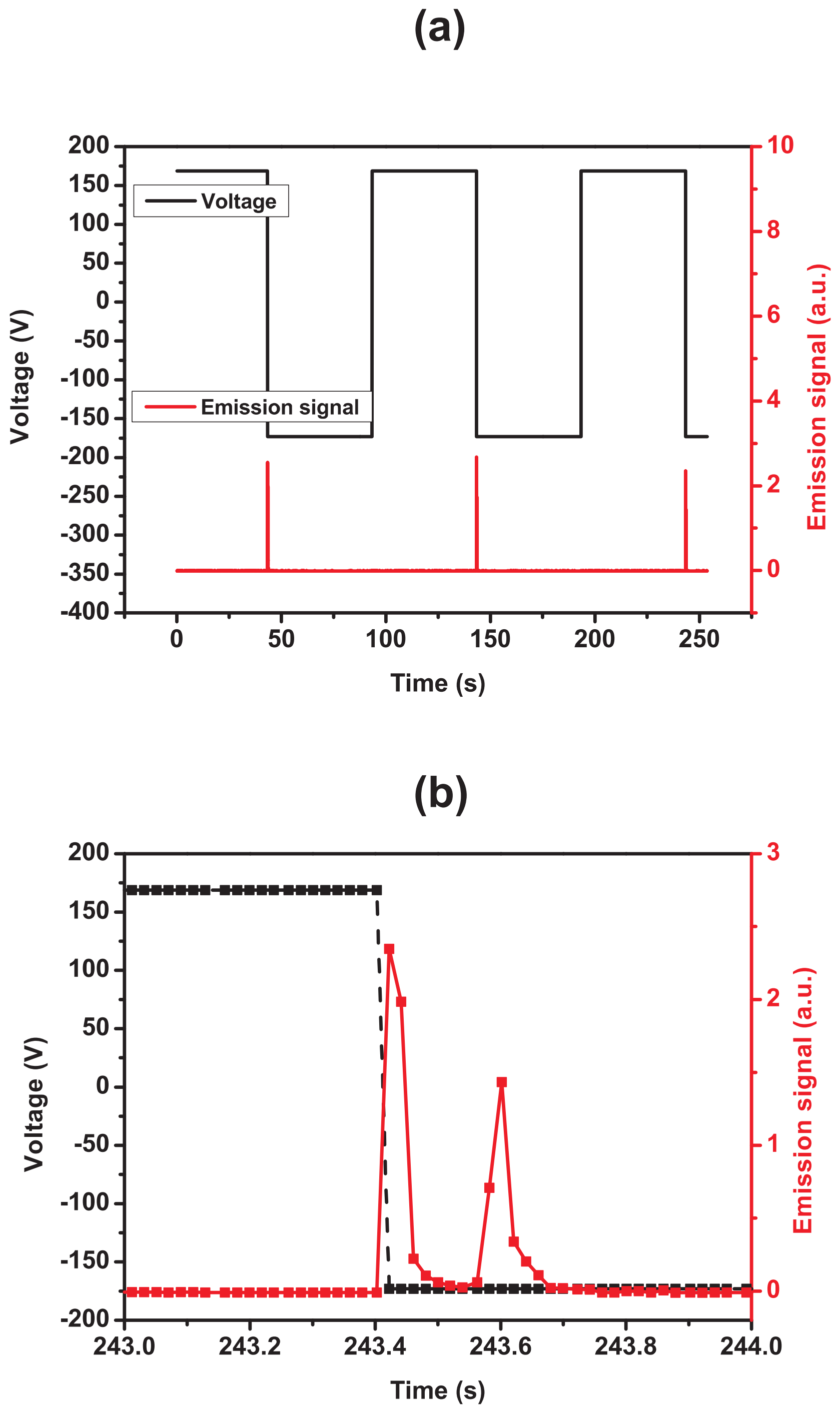

Figure 5.7: Electron emission dependence on polarization orientation. A square shaped voltage of 10 mHz frequency and 170 V amplitude was applied to the bottom electrode and the resulting electron emission was measured by a single electron detector. Both voltage and recorded emission signal are shown as a function of elapsed time. Obviously, electron emission occurs only at the transition from a positive to a negative voltage, as can be seen in part (a). Part (b) shows a fraction of part (a), which contains an electron emission pulse, in more detail. The emission conists of two distinct pulses and is completed after a period of about 300 ms.

present, which take place on different time scales, as has been reported for PMN-PT and PZN-PT single crystals [110]. Thus, the field induced polarization variation, which is screened by charge emission, is divided into several steps. This issue will be discussed in more detail in Section 7.3.

The impact on the electron emission is quite obvious. For high excitation frequencies, the polarization reversal is not completed and only parts of the first emission peak shown in Figure 5.7 (b) are measured. This explains the higher amount of charges emitted per single switching cycle for decreased frequencies, as can be seen in Figure 5.6 for a square wave voltage applied to the bottom electrode.

5.3.2 Polarization Reversal

Ferroelectric electron emission is initiated by a variation of the spontaneous polarization. In this work, electron emission was achieved by the application of an external voltage. Accordingly, the dependence of the polarization on the applied voltage should explain the presence of the different regimes of electron emission, which have been shown in Figure 5.5. A ferroelectric hysteresis loop of PMN-PT can be seen in Figure 5.8. A voltage ramp was applied between top and bottom electrode and the current flow was measured. From this data, the hysteresis loop of the polarization was calculated. Coercive voltage values of $70\,\mathrm{V}$ and $-82\,\mathrm{V}$ can be obtained from the graph. The asymmetry of the two values is caused by the prepoling of the sample. Initially, the out-of-plane polarization component is oriented in the positive z-direction and a higher energy and consequently a higher voltage is required to switch the polarization vector in the opposite direction.

From Figures 5.4, 5.6, and 5.5 a strong enhancement for voltage amplitudes $> \sim 80\,\mathrm{V}$ is known. This was marked as the threshold voltage between the first and second emission regime. Furthermore, Figure 5.7 revealed the restriction of electron emission to negative bottom electrode voltages. The correlation between the negative switching voltage of $82\,\mathrm{V}$ and the threshold voltage of $\sim 80\,\mathrm{V}$ is obvious and can be seen in Figure 5.9.

There, electron emission measurements are shown, which were performed on the same sample as for the hysteresis loop presented in Figure 5.8 with a sinusoidal excitation voltage of $1\,\mathrm{kHz}$. The signal recorded by the single electron detector is indicated in black, whereas the blue curve corresponds to the current measured directly by means of the electrometer. Both graphs are shown as a function of the voltage amplitude. Like for the measurements presented in Section 5.2, the transition between the first and second emission regime is

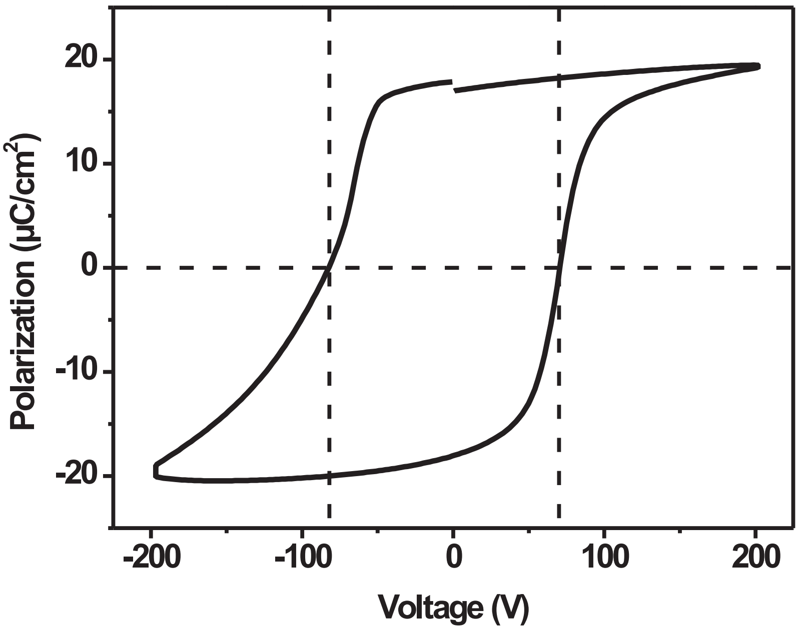

Figure 5.8: Hysteresis loop of a PMN-PT single crystal. A voltage ramp was applied between top and bottom electrode and from the recorded current flow the ferroelectric polarization was calculated. The vertical dashed lines mark the coercive voltages. Values of 70 V and -82 V were revealed.

clearly visible and characterized by a significant increase of the electron emission current. The coercive voltage obtained from Figure 5.8 is marked by the vertical dashed green line and can be attributed to the transition voltage. The strong increase of the electron emission is quantified by linear fits to the detector signal, which are indicated by the dashed red lines. The slope of the count rate is about 100 counts $(\mathrm{Vs})^{-1}$ and 12000 counts $(\mathrm{Vs})^{-1}$ for the first and second regime, respectively.

Thus, the onset of polarization switching is responsible for the enhancement of electron emission that goes along with the transition to the second emission regime. However, the coercive voltages obtained from Figure 5.8 indicate a polarization reversal in the crystal volume below the top electrode. From calculations of the electric field strength, which are shown in Figures 3.3, 3.4, and 3.5, it can be deduced that in the aperture region smaller field strength are present. The spontaneous polarization will be reversed only in a small fraction of the free surface area in proximity to the electrode edges and therefore, in this voltage regime, electron emission is limited to the region close to the top

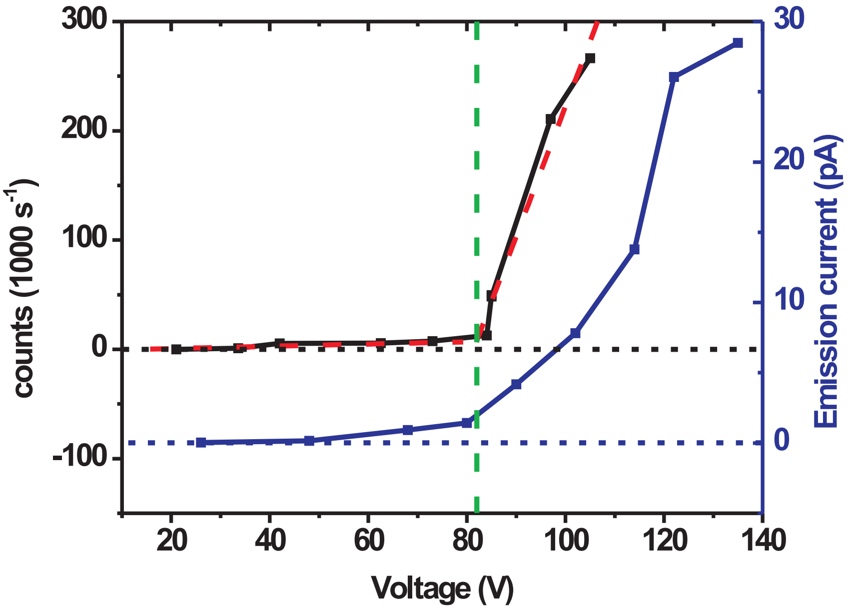

Figure 5.9: Impact of polarization switching on electron emission. Electron emission signals were measured by a single electron detector (black curve) and by an electrometer (blue graph) for a sinusoidal voltage with 1 kHz frequency. Both curves are shown as function of the voltage amplitude. Particular attention is paid to the transition between the first and second emission regime at a threshold voltage of about 80 V, which comes along with a strong signal enhancement. The transition corresponds to the onset of polarization switching. The coercive voltage of 82 V is marked by a vertical dashed green line. For the detector signals, the slopes of the count rate are marked with dashed red lines for each regime and reveal values of 100 counts $(\mathrm{Vs})^{-1}$ and 12000 counts $(\mathrm{Vs})^{-1}$ for the first and second regime, respectively.

elctrode.

To verify this, electron emission was measured with only one part of the top electrode being contacted and therefore, without a confined aperture, the polarization will only be reversed in a fraction of the whole uncovered sample surface. Figure 5.10 shows the results achieved with a square wave voltage of 1 kHz frequency. The emission current measured with the electrometer can be seen in dependence on the voltage amplitude in the black curve. It is compared to the recorded emission current for the same excitation voltage when both parts of the top electrode were used, which is presented as the blue graph in Figure 5.10. For small voltage amplitudes the behavior of the two curves is similar and it can be seen that the transition to the second emission regime at $\sim 80\,\mathrm{V}$ takes place for both experiments. For this, no aperture is required

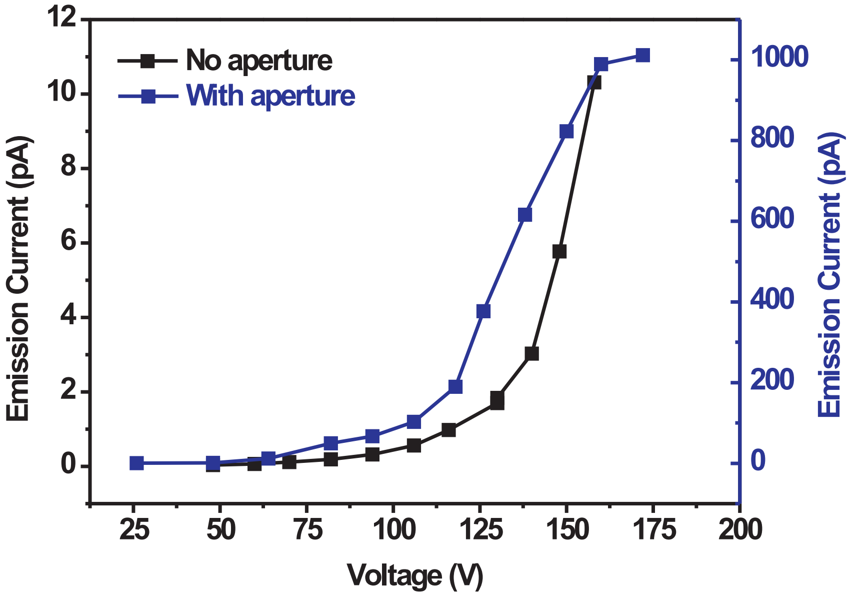

Figure 5.10: Impact of the electrode structure. The black curve shows the recorded electron emission current for a top electrode without an aperture. Electron emission is restricted to the free surface region close to the electrode edges. The blue graph corresponds to the emission current achieved with an aperture in the electrode structure (see Figure 5.1). Both experiments were performed with a square wave excitation voltage of $1\,\mathrm{kHz}$ frequency.

but a junction of an electrode and a free surface area, which was given for both measurements. However, for higher voltages, the signal increase is much stronger for the blue curve. This is an aperture related effect as well as the transition to the third emission regime, which is characterized by a change of the slope of the current , at voltage values of $\sim 120\,\mathrm{V}$. The confinement of the aperture leads to much larger electric fields at the sample surface and the polarization switching in the whole free surface region results in a change of the current slope in the third regime. Accordingly, no third emission regime is visible in the black graph, corresponding to an "aperture-free" electrode structure, but an exponential increase for all voltage values. For this electrode structure smaller electric fields are initiated, since the free screening charges are able to redistribute to non-switched regions of the crystal surface. This explains the difference of the measured emission currents for the two curves, which is about two orders of magnitude.

5.4 Energy Distribution

The kinetic energy of the emitted electrons is an important parameter of any cathode and determines possible device structures of the emitter. Generally, high kinetic energies are favorable, since the need of an additional acceleration voltage complicates the cathode structure. For a possible usage in electron microscopes a discrete energy spectrum is desired to tune the electron wavelength.

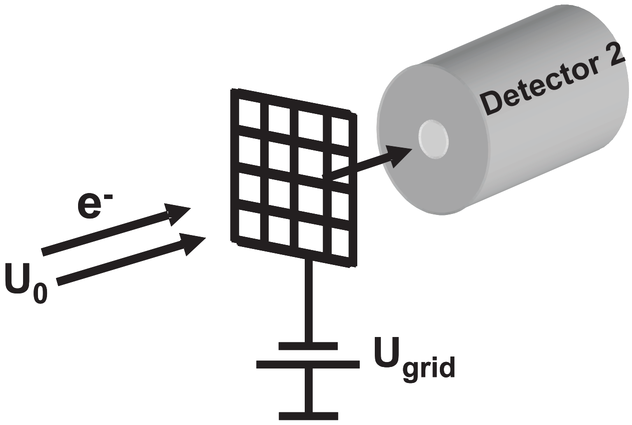

Figure 5.11: Modified setup for measurements of the electron energy. A metal grid was positioned in front of the detector aperture. A negative dc bias applied to the grid repels incoming electrons. Only particles with a sufficient kinetic energy overcome the repulsive field and are counted by the detector.

In order to access the kinetic energy of the electrons emitted from the presented PMN-PT structures, one of the single electron detectors was modified. A metal grid was placed in front of the detector aperture. The periodicity of the mesh was $100\,\mu$m. The grid, on the one hand, screens the built-in detector voltage of $+500\,$V, whereas, on the other hand, acts as an energy filter when biased with a negative dc voltage U_{grid}. Then, only electrons that have a sufficient kinetic energy are able to overcome the repelling force from the grid and pass through it towards the detector. A basic sketch of this principle can be seen in Figure 5.11.

Figure 5.12 shows the measured count rates as a function of U_{grid} for the example of sinusoidal excitation voltages with $110\,$V and $140\,$V amplitudes and $1\,$kHz frequency. The obtained count rates were normalized to the total emission signal as measured simultaneously by detector 1, which was used as an in-situ reference without a mesh. As can be clearly seen, the signal decreases continuously for a rising negative grid voltage. This indicates a broad energy distribution of the emitted electrons. The maximum kinetic electron energies correspond to the smallest negative grid voltage ${U_{grid}}^{max}$ with no counted

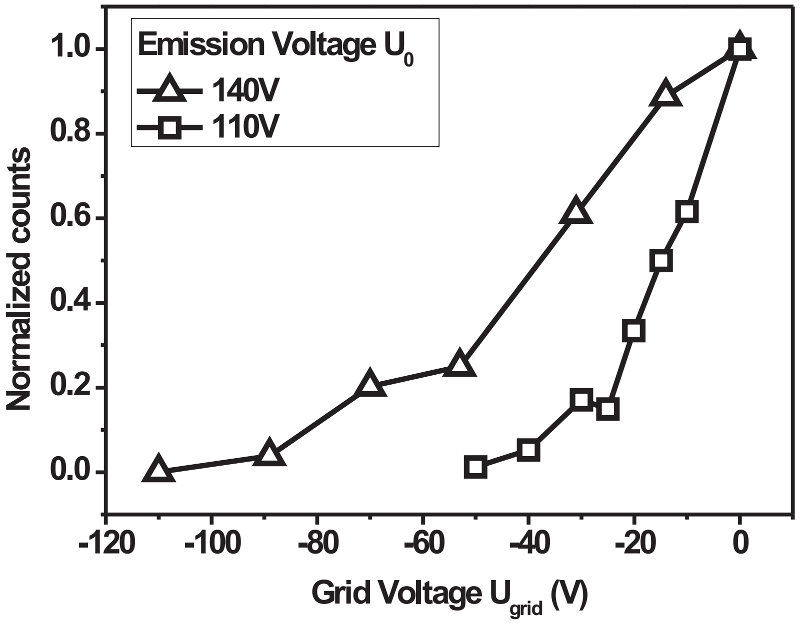

Figure 5.12: Energy distribution of the emitted electrons. The emission signal for different voltages U_{grid} applied to the metal grid placed in front of detector. The count rates were normalized to the signal with zero grid voltage. The measured signal continuously decreases in both curves that are collected for sinusoidal emission voltages of 140 V and 110 V and a frequency of 1 kHz. This is interpreted as a broad energy distribution of the emitted electrons. The maximum energy corresponds to the first grid voltage with no counted electrons, and is determined to be 110 eV and 50 eV for emission voltages of 140 V and 110 V, respectively.

electrons. From Figure 5.12 values of about 110 eV and 50 eV can be deduced for the emission voltages of 140 V and 110 V, respectively. This is much lower compared to values of several kilovolts, as reported so far in the literature for other samples and experimental setups [10]. Since ${U_{grid}}^{max}$ is smaller than the applied voltage amplitude, the emitted electrons were accelerated by the excitation voltage only and thus, the amplitude U_0 is the upper limit of the kinetic electron energy.

5.5 Surface Conductivity of Emitter Structures

Ferroelectric Electron Emission is a transient current that screens a variation of the spontaneous polarization. In order to achieve a steady current, the polarization must be changed periodically. However, this requires a certain time span between two emission pulses to bring the system back into the initial state, where the depolarization field is screened by free charges. Sufficient supply of new screening charges is required, since these charges are to be emitted in the next polarization switching cycle.

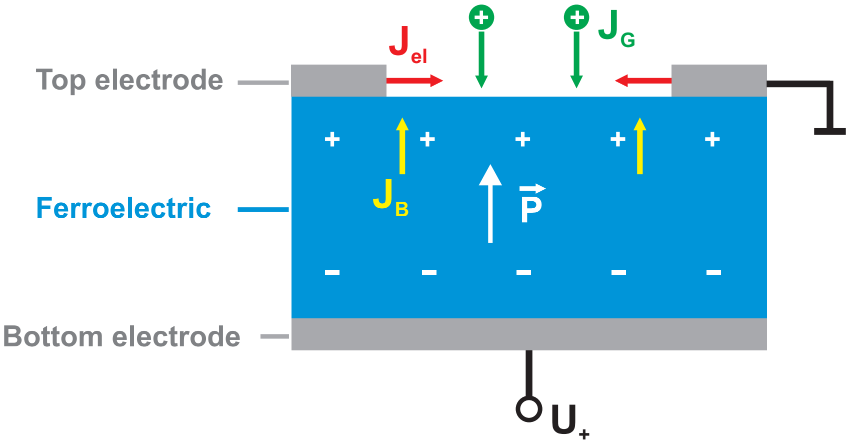

Figure 5.13: Screening currents between electron emission cycles. A positive voltage is applied to the bottom electrode after an electron emission pulse, which switches the ferroelectric polarization (indicated in white color). Negative charges are distributed at the sample surface in the aperture to screen the depolarization field. Several screening currents are possible. A current through the material bulk is indicated as J_B. J_G denotes the ionization of surrounding gas atoms or molecules. A charge injection current from the top electrode is shown as J_{el}. The arrows are oriented in the direction of the electron motion.

Different mechanisms of charge supply are possible and sketched in Figure 5.13. The case of a positive voltage applied to the bottom electrode is shown, which corresponds to the situation, when the polarization has been switched back to an upward orientation after an emission pulse. The resulting depolarization field is to be screened by negative surface charges. Three main processes are possible to bring the system to an equilibrium state and are indicated by arrows in Figure 5.13. J_B denotes a current through the material bulk. However, for the PMN-PT crystals used in this work, J_B can be neglected, owing to the good insulating properties of the material. The ionization of surrounding gas atoms or molecules is shown as J_G. The contribution of this current strongly depends on the ambient pressure and it is known from the literature that reduced pressure leads to a faster relaxation of the unscreened polarization state [11, 83]. The results presented in this chapter were obtained at a pressure of $\sim 10^{-7}$ mbar and thus, only a minor contribution of J_G is expected. The third possible screening current originates from the top electrode and consists of field emission from the electrode edges and a surface current J_{el}, which flows across and within a thin layer below the crystal surface.

In the following, a rough estimation of the surface current is presented leading to the conclusion that, for high frequencies of emission pulses, this current is not sufficient to completely screen the polarization variation. This is one reason for the observed saturation levels of electron emission for 1 kHz square wave excitation voltages.

If a positive voltage is applied to the bottom electrode, electrons are ejected from the top electrode and accelerated towards the aperture center by horizontal components of the electric field. This is basically the same process as for the formation of a surface flashover plasma in strong FEE (see Section 3.3). The magnitude of this current J_{el} is determined by the surface conductivity of the material in the aperture region.

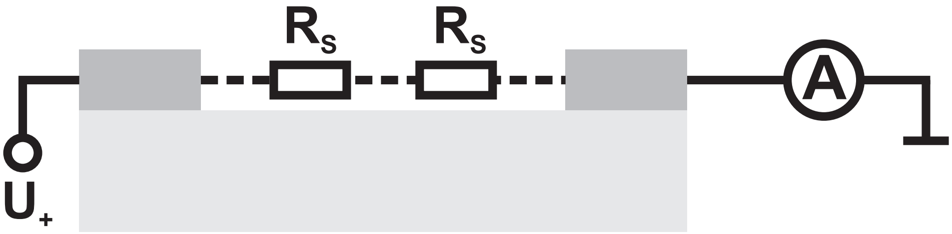

Figure 5.14: Surface conductivity measurements of the emitter structure. A dc voltage is applied between the two parts of the top electrode and the current flow is measured. The resistors R_S are determined by the surface conductivity and limit the recorded current.

In order to access this parameter, a dc voltage was applied between the two parts of the top electrode and the current flow was measured. The principle of this experiment is sketched in Figure 5.14. From the recorded current the resistance R_S can be deduced. This value describes the conductivity of the free surface area and thus, determines the surface current J_{el}. The value of R_S could be calculated to be $> 10^{11}\,\Omega$, which corresponds to a resistivity of $8 \cdot 10^{13}\,\Omega/\text{cm}$.

Taking this as a starting point, an upper limit of J_{el} can be estimated. In the screening process, charges are ejected from the top electrode edges and move towards the aperture center. Two symmetric components of J_{el} are present, each screening half of the free surface area, as can be seen in Figure 5.15.

The surface current is driven by the horizontal components of the electric field applied to the bottom electrode. The calculated distribution of the

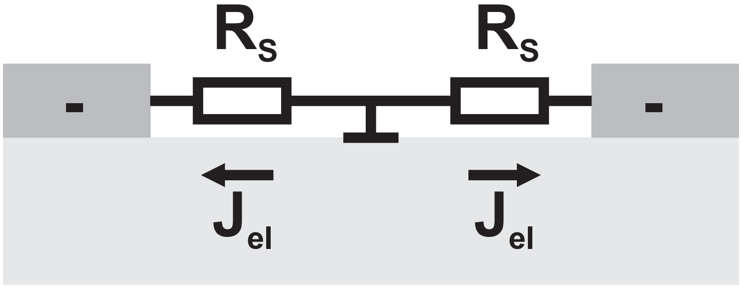

Figure 5.15: Charge injection from the top electrode. The screening current J_{el} flows symmetrically from both sides towards the center of the aperture. The equivalent circuit is shown. The two resistors R_S limit the magnitude of J_{el}.

electric field oriented parallel to the sample surface is depicted in Figure 5.16. This simulation was done with the condition of a voltage applied to the bottom electrode whereas the top electrode was put on ground potential and the same parameters as used for the calculations shown in Figure 3.3. The aperture size was $\sim$ 6 % of the sample thickness and thus close to the value of the investigated PMN-PT crystals. Equal value lines of the horizontal field component E_x are shown normalized to the voltage amplitude U_0, which was applied to the bottom electrode. It is clearly visible that in the aperture center E_x is zero. Close to the electrode edges, the field is enhanced to values up to $1.5 \cdot U_0/d$, where d represents the sample thickness. For an increasing distance from the electrode E_x strongly decreases and only a small field strength of $\sim 0.3 \cdot U_0/d$ remains. Obviously, the surface current strongly depends on the distance from the top electrode and thus, the screening process is less efficient in regions close to the aperture center.

From Figure 5.5 it can be seen that the fourth emission regime, which is characterized by a saturation of the emission current, is initiated for voltage amplitudes of 160 V. To simplifiy the following estimation of the surface current, a voltage component U_S, parallel to the surface, of 80 V is assumed in the aperture for an excitation of 160 V, averaging the field distribution, which is shown in Figure 5.16. This assumption was made to simulate the situation in the area in proximity to the aperture center. A complete screening of the polarization variation close to the electrode edges is assumed due to the high horizontal field components in this region. Therefore, any limitation of the electron emission is caused by an incomplete screening of the interior aperture area.

The surface current then can be approximated to:

$$J_S \approx 2 \cdot \frac{U_S}{R_S} = 1.6 \cdot 10^{-9}\,\mathrm{A} \quad . \tag{5.1}$$

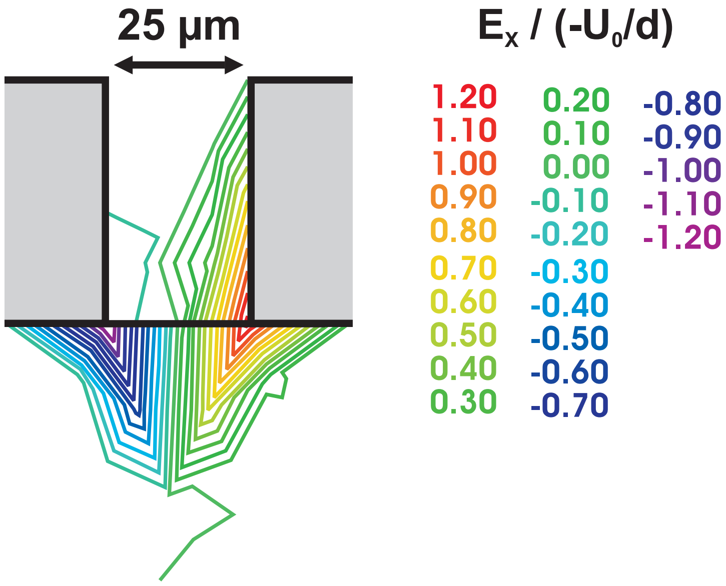

Figure 5.16: Calculations of the horizontal electric field component in emitter structures. The aperture size is ∼ 6% of the sample thickness *d*. A voltage U_0 is applied to the bottom electrode, whereas the top electrode is put on ground potential. Equal value lines of E_x are shown normalized to U_0/d.

The saturation of the emission current was observed for voltage frequencies of 1 kHz. The time t between the emission pulses is half the periodic time of the voltage, i.e. 0.5 ms in this particular case. Accordingly, the amount of new charges Q_S, which are distributed to the aperture region after each emission pulse to screen the polarization variation can be calculated:

$$Q_S = J_S \cdot t = 8 \cdot 10^{-13}\,\mathrm{C} \quad . \tag{5.2}$$

The achieved electron emission current for a voltage amplitude of 160 V was about 10^{-9} A (see Figure 5.5). Hence, a charge of 10^{-13} C is emitted per voltage cycle for a frequency of 1 kHz. Even though the estimated screening charge Q_S of $8 \cdot 10^{-13}$ C is larger than the emitted charge, both values are of the same order of magnitude. Taking into account the several simplifications and assumptions made for the calculation of Q_S, the real value might be smaller, which is particularly owed to the strong decrease of the horizontal field component E_x for larger distances from the top electrode. This makes the screening process less effective in regions close to the aperture center. Furthermore, the obtained surface resistivity of $8 \cdot 10^{13}\,\Omega/\mathrm{cm}$ has to be treated as a lower limit, since the measured values showed a strong scattering and the value used for the assumption presented in this section was the smallest one. Higher resistivities lead to a smaller surface current.

Probably, the incomplete screening process is responsible for the observed smaller slope of the emission current for voltage amplitudes $> 160\,\mathrm{V}$. In Ferroelectric Electron Emission, screening charges are emitted and a limited charge supply confines the achievable emission current. The time span, which is available for the screening process between the emission cycles, increases for decreasing voltage frequencies. Thus, a higher emission charge per cycle is possible and no saturation of the emission was observed for lower frequencies.

6 Electron Emission from PZT Thin Films

Decreasing the thickness of the emitter material is a promising way to reduce the operation voltage of a ferroelectric cathode. This chapter presents electron emission from 600 nm-*thick lead zirconate titanate (PZT) thin films. In the first section the preparation of top electrodes with sub-micrometer sized apertures is described, whereas in the second section successful electron emission from these structures is demonstrated for operation voltages* $< 20\,\mathrm{V}$. *In the last part it is shown that the electron emission is initiated by the onset of a complete reversal of the ferroelectric polarization.*

6.1 Sample Preparation

Lead zirconate titanate is a well known ferroelectric and has been studied in much detail (see Section 2.4). In this work, thin films of $\mathrm{Pb(Zr_{0.4}Ti_{0.6})O_3}$ compositions were used. Films of 600 nm thickness were prepared by multi-target sputtering together with a conductive $\mathrm{BaPbO_3}$ oxide bottom electrode, which was about 30 nm thick, on silicon wafers [111, 112]. The oxide bottom electrode significantly reduced the fatigue of ferroelectric properties compared to a platinum electrode [50].

It was dicussed in Section 3.4 that special requirements have to be fulfilled for the top electrode structure in order to achieve an electron emission from ferroelectric thin films. In a "plane-to-plane" electrode geometry, which is shown in Figure 3.2 (a), a large voltage drop takes place in the vacuum gap and only a very small fraction of the applied voltage affects the ferroelectric layer. Therefore, a structured top electrode pattern has to be used. From Figure 3.5 it is known that the aperture size should be smaller than the film thickness. Otherwise, the normal component of the electric field within the free surface region will be too small to initiate a switching of the spontaneous polarization. For the PZT films used here, this means an aperture width of several hundreds of μm, which is below the resolution limit of any available electron beam lithography device.

Hence, a different approach was chosen, which is sketched in Figure 6.1. By means of spin coating a monolayer of commercially available polystyrene beads (Sigma Aldrich GmbH, Germany) was distributed on the sample surface. The diameter of the spheres was 300 nm. Neighboring particles are in direct contact as is shown in part (a). In the next step the size of the beads was decreased by plasma etching, which results in a certain distance between the spheres (see Figure 6.1 (b)). This regular pattern was used as a mask for the evaporation of 5 nm-thick and 60 nm-thick metal layers of chromium and gold, respectively, which is depicted in part (c). When being cleaned in an ultrasonic bath, the residual particles can easily be removed and the resulting structure is shown in Figure 6.1 (d). It is a metal-covered area with regularly arranged apertures at the positions formerly covered by the polytsyrene spheres.

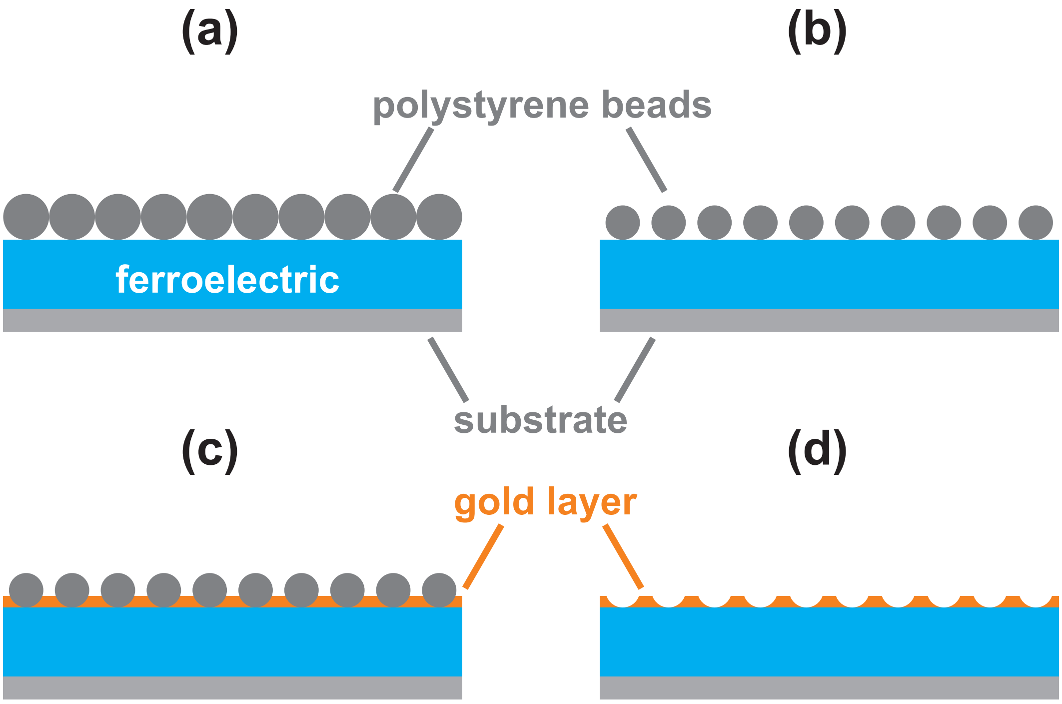

Figure 6.1: Top electrode preparation on PZT thin films. (a) A monolayer of polystyrene beads is distributed on the film surface. (b) Plasma etching shrinks the particle diameter and creates free space between neighboring spheres. (c) A gold layer is evaporated on top of the structure and fills the space between the particles. (d) The polystyrene beads are removed by cleaning in an ultrasonic bath. A closed metal surface remains, which contains regularly patterned apertures.

With this method the size of the apertures can be tuned by changing the duration of the plasma etching process and the thickness of the evaporated metal layers. Moreover, the space between the different holes in the electrode is determined by the initial particle diameter. A similar approach based on a stochastical particle distribution has been reported [113], but the particle diameter was 10 μm in this case. Thus, the presented method of top electrode structuring is indeed unique and offers the possibility to prepare structured aperture patterns with full control of any important parameters.

For the electron emission experiments presented in Section 6.2 the created apertures had a diameter of about 200 nm, as can be seen in Figure 6.2. Accordingly, it is expected to switch the whole free surface region with reasonable voltages applied between top and bottom electrode. The size of the gold electrode was $< 0.5\,\mathrm{mm}^2$, but is difficult to be quantified exactly, since the gold was partially removed during the cleaning process.

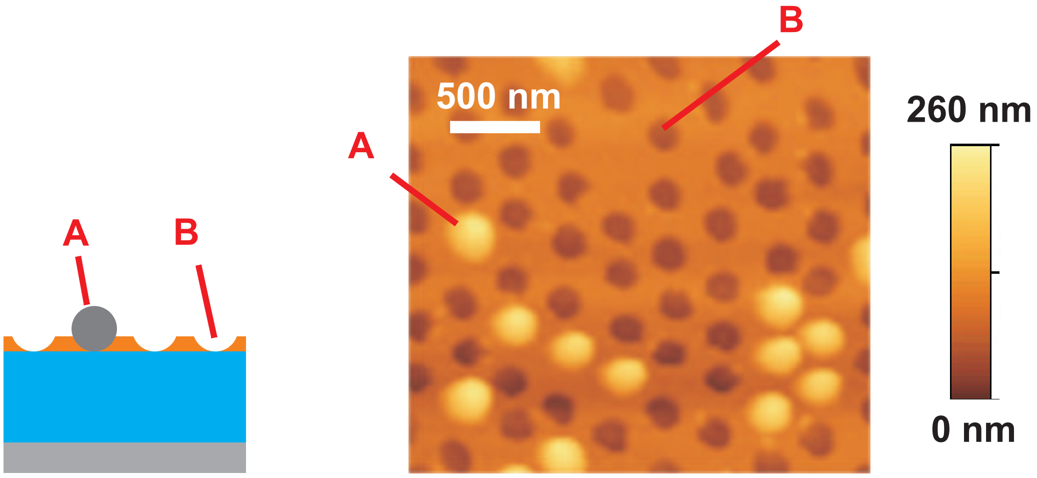

Figure 6.2: AFM-image of the top electrode structure. The film surface is covered by a gold layer. The dark spots represent the apertures with an average size of about 200 nm. The bright regions are polystyrene particles which have not been removed during the cleaning process.

6.2 Electron Emission Measurements

Electron emission experiments were performed with the same electrical wiring as shown in Figure 5.2. An ac voltage was applied to the bottom electrode, whereas the top electrode was put on ground potential. The count rate measured with a single electron detector is shown in Figure 6.3 as a function of the voltage amplitude. The emission was achieved with a sinusoidal excitation voltage of 1 kHz frequency.

It is clearly visible that the general signal strength is much smaller than the emission obtained from the PMN-PT crystals, which has been presented in

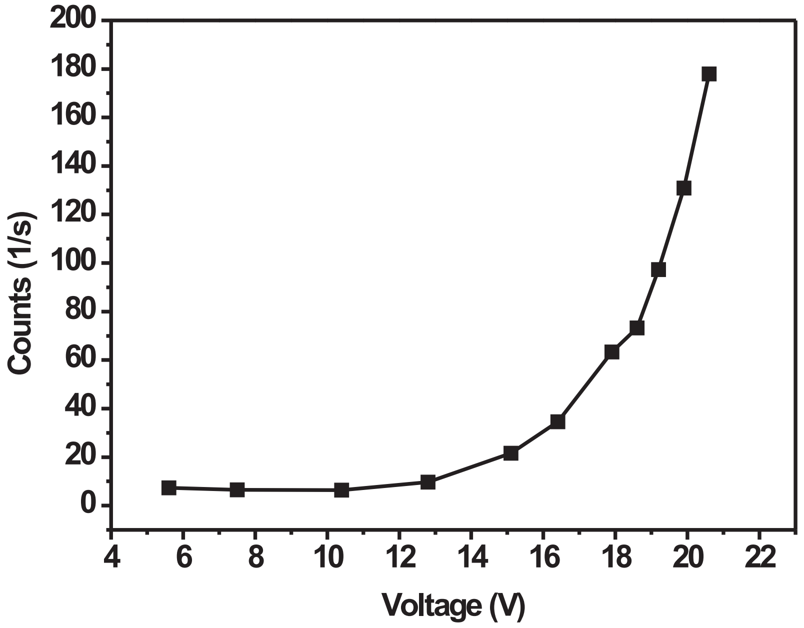

Figure 6.3: Electron emission from PZT thin films. The emission was achieved with a sinusoidal excitation voltage of 1 kHz frequency. The count rate obtained by means of the single electron detector is shown as a function of the excitation voltage amplitude. For voltage values < 13 V the emission signal was below the resolution limit of the detector.

Section 5.2. The highest observed count rate was 180 counts/s. Furthermore, an exponential behavior of the count rate can be seen with an onset of the electron emission for a voltage amplitude of about 13 V.

The small emission signal might be caused by the area of the apertures, which is approximately $3 \cdot 10^{-2}\,\mu\text{m}^2$ for each single opening. With the size of the top electrode being $< 0.5\,\text{mm}^2$ an upper limit of about $0.1\,\text{mm}^2$ for the free surface area can be estimated. However, due to irregularities in the pattern and polystyrene particles, which remain at the sample surface, the real value is smaller. To increase the electron emission current, the electrode preparation has to be improved and extended to larger areas.

However, the small measured count rates cannot be explained by the size of the free surface area, which is comparable to the aperture size of the PMN-PT single crystals, only. In Figure 3.3 the ratio of aperture width w and sample thickness d was revealed to be an important parameter for the distribution of the electric field. Values of $\frac{1}{3}$ and $\frac{1}{16}$ can be calculated for the PZT and PMN-PT systems, respectively. As a result, higher field strengths compared to the respective coercive fields are required to switch the polarization in the free surface area of the PZT films than for the PMN-PT crystals.

Beside the relative ratio w/d, the aperture width of 200 nm means a close proximity of the aperture center to the top electrode and therefore increases the probability of the screening current J_C to be initiated (see Figure 3.1). This current strongly depends on the surface conductivity and is competitive to the electron emission process. For decreasing distances to the electrode edges, more surface charges are attracted by the top electrode and subsequently screened by J_C as a current in the external circuit. Therefore, a smaller fraction of the imbalance surface charges is emitted into the vacuum.

This is a general drawback of thin film emitters, since a reduced thickness of the material requires smaller aperture sizes in order to initiate an electron emission current. Consequently, the aperture center exhibits a smaller distance to the top electrode for thin film cathodes. This is combined with an increased impact of the competitive screening current J_C and a less efficient emission process.

6.3 Influence of Ferroelectric Polarization

From Figure 6.3 an onset of the electron emission for voltage amplitudes $> 13\,\mathrm{V}$ was revealed. In order to clarify the impact of the ferroelectric polarization on the emission process, the dependence of the spontaneous polarization on an externally applied electric field was investigated for different thicknesses of the $BaPbO_3$ oxide bottom electrode [50]. The obtained hysteresis loops can be seen in Figure 6.4.

Coercive field strengths of $-180\,\mathrm{kV/cm}$ and $220\,\mathrm{kV/cm}$ can be determined for a bottom electrode thickness of 30 nm. These values correspond to coercive voltages of $-10.8\,\mathrm{V}$ and $13.2\,\mathrm{V}$, respectively. Accordingly, a measurable electron emission signal is only present for excitation voltages, which induce a complete switching of the ferroelectric polarization. The polarization reversal leads to more imbalance negative surface charges and thus, similarly to the electron emission from PMN-PT single crystals (see Section 5.3.2), strongly enhances the electron emission current.

Owing to the generally small signal strength observed for the electron emission from the investigated PZT films, the presence of an emission current for excitation voltages $< 13\,\mathrm{V}$ cannot be ruled out. However, a possible emission signal in this voltage regime was below the resolution limit of the detector. Accordingly, an increased emission is necessary to clarify this and will most probably be successfully achieved by an optimization of the top electrode

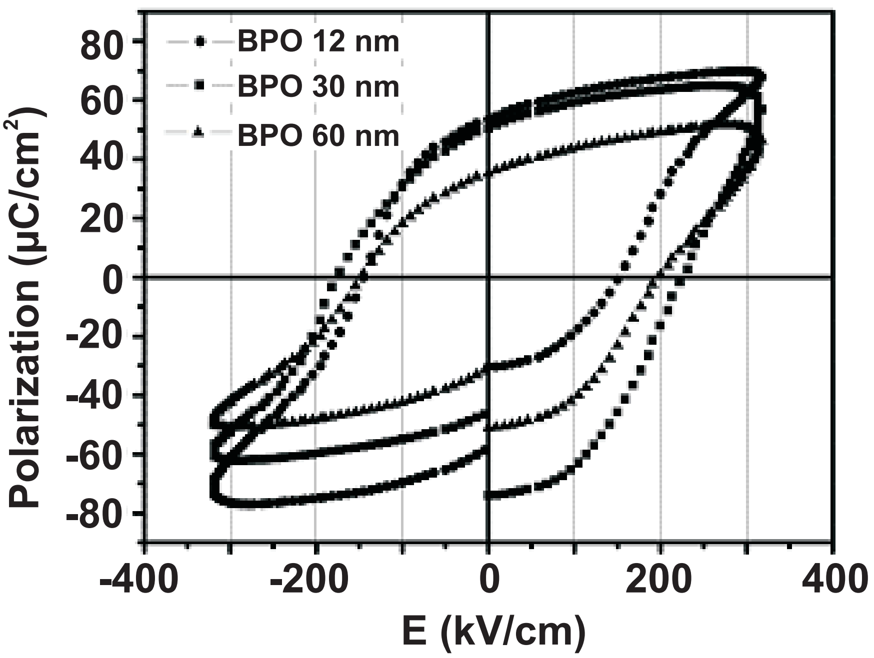

Figure 6.4: Hysteresis loops of PZT thin films for different thicknesses of the $BaPbO_3$ bottom electrode. Coercive field strengths of -180 kV/cm and 220 kV/cm are revealed for a 30 nm thick electrode [50].

preparation process. Another promising approach is the usage of films with a larger thickness of $\sim 1\,\mu$m, where the thickness dependent effects, such as small aperture sizes, are reduced.

7 Switching of Ferroelectric Polarization in PMN-PT Single Crystals

Ferroelectric electron emission is initiated by changes of the ferroelectric polarization. In this work, the polarization has been varied by the application of external voltages. Accordingly, it is crucial to understand and investigate the dependence of the spontaneous polarization on an externally applied voltage. This is the subject of this chapter. In the beginning, the initial domain structure of the investigated PMN-PT single crystals is shown as well as the coexistence of monoclinic phases. The second part presents macroscopic hysteresis curves revealing a strong frequency dependence of the switched charge. The third section shows measurements of a rotation of the polarization vector and possible rotation paths are discussed. Finally, the voltage-dependent domain state in the electrode structures used for electron emission measurements is imaged by piezoresponse force microscopy.

7.1 Initial Domain Structure

It has been shown in Sections 5.3 and 6.3 that the electron emission process is strongly influenced by the dependence of the ferroelectric polarization on an externally applied electric field. Due to the relaxor ferroelectricity of lead magnesium niobate - lead titanate, the distribution of the spontaneous polarization on the nanoscale is very random. Small polar clusters with a size of several nanometers are formed [114], caused by the differently charged ions and spatial composition inhomogeneities.

Moreover, the coexistence of crystal phases with monoclinic symmetry has been predicted [115] and reported [44, 45] for compositions close to the morphotropic phase boundary, as is shown in Figure 2.5. The reduced symmetry of a monoclinic structure leads to more possible orientations of the polarization.

In contrast to a rhombohedral or a tetragonal symmetry, where the polarization is restricted to certain crystal axes, the polar vector is only confined to be aligned within a certain mirror plane for a monoclinic phase.

Two different monoclinic phases have been identified for (001)-oriented crystals. In the so-called M_A and M_C phases, the polarization vector is restricted to the $\{110\}$ and $\{100\}$ crystallographic planes, respectively. This is sketched in Figure 7.1, where the monoclinic mirror planes are shown for a perovskite unit cell.

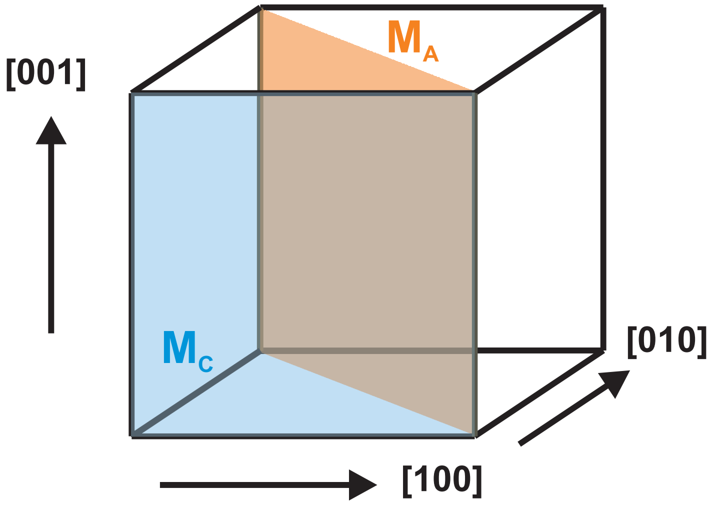

Figure 7.1: Monoclinic mirror planes in a perovskite. The monoclinic M_A and M_C phases are present in PMN-PT crystals with a composition close to the morphotropic phase boundary. In contrast to a rhombohedral or tetragonal phase, where the polarization is pinned along certain crystallographic axes, in monoclinic phases the polarization vector is confined to certain mirror planes. As examples, the (110) monoclinic plane (M_A) is shown in orange color, whereas the (010) plane (M_C) is indicated in blue.

The stability of the two monoclinic phases is strongly determined by the composition ratio x of the $(1\text{-x})\mathrm{Pb}(\mathrm{Mg}_{1/3}\,\mathrm{Nb}_{2/3})\mathrm{O}_3$ - $x\mathrm{PbTiO}_3$ compound. The presence of M_A phases has been observed for $0.27 \leq x \leq 0.30$, whereas M_C phases are stable for $0.31 \leq x \leq 0.34$ [116]. Thus, for the crystals investigated in this work, which exhbit a value of $x = 0.28$, M_A phases are expected to coexist with a rhombohedral symmetry.

All this leads to a rather intricate ferroelectric domain structure in PMN-PT, which depends not only on the composition and crystal orientation but also on the sample history. By means of piezoresponse force microscopy (see Section 4.2) the initial domain distribution of the PMN-PT crystals was imaged and can be seen in Figure 7.2. The amplitude and the phase of the PFM signal are shown for the polarization components perpendicular (out-of-plane) and parallel (in-plane) to the sample surface, i.e. in z and x-direction, respectively (see Figure 4.3).

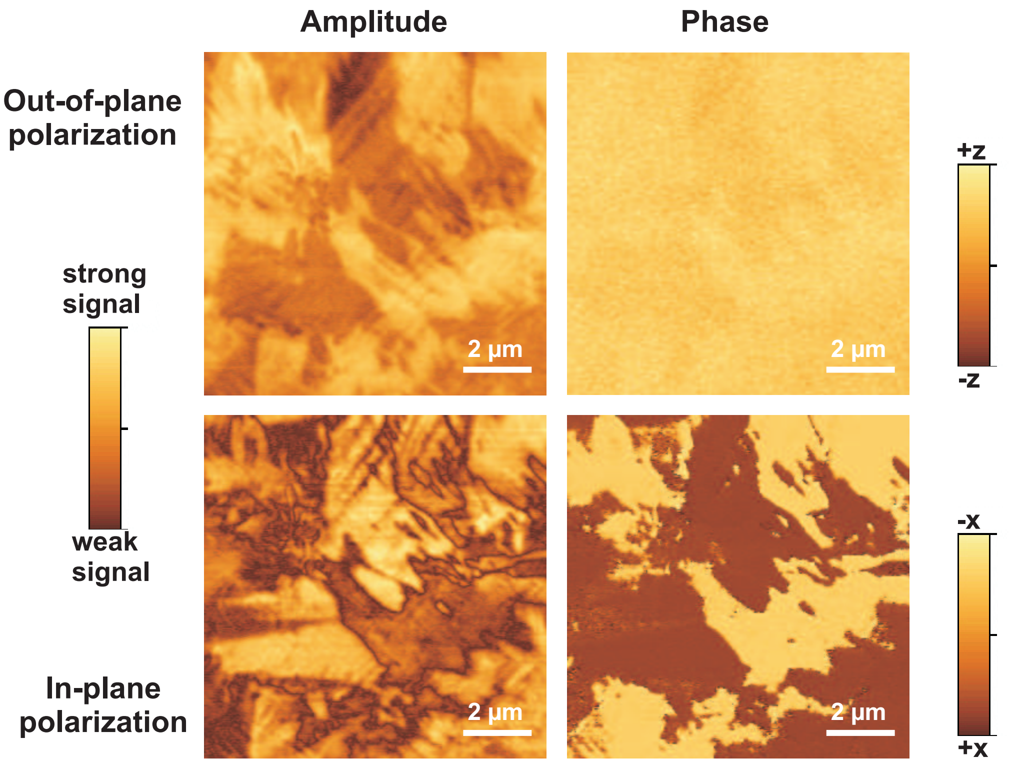

Figure 7.2: Domain structure of PMN-PT samples. PFM measurements of an untreated PMN-PT crystal are shown. The upper row shows the out-of-plane signal, whereas the lower row represents the polarization component, which is oriented parallel to the surface and perpendicular to the cantilever axis. The left column shows the amplitudes of the PFM signals and can be seen as a measure of the polarization magnitude. The right column contains the phase images and therefore shows the polarization orientation.

The z-signal phase reveals an almost constant value, which corresponds to a polarization orientation out of the sample surface in positive z-direction. This is caused by the prepoling of the crystals done by the manufacturer. The small signal fluctuations are probably caused by a buckling of the cantilever for domains pointing in y-direction, since they are correlated with the contrast, which is visible in the respective amplitude image. There, different polarization states can be clearly identified. In a perfect rhombohedral crystal structure (see Figure 2.2), all four possible polarization states being oriented in +z-direction should exhibit the same magnitude in the out-of-plane signal. Therefore, the contrast in the amplitude is caused either by a polarization relaxation on a local scale or by the presence of monoclinic crystal phases, where the polar vector is only confined in a certain mirror plane.

The phase image of the x-signal reveals the presence of regions with a polarization oriented in +x-direction as well as domains pointing in -x-direction. A diversified contrast can be seen in the in-plane amplitude image, which is partially correlated to the domains identified from the out-of-plane signal. A larger amplitude in the out-of-plane image leads to a weaker signal in the in-plane orientation and vice versa. This suggests the presence of monoclinic crystal phases. Hence, apart from the prepoling in +z-direction, a complex domain structure is obtained.

7.2 Macroscopic Polarization Reversal

The macroscopic switching behavior of the ferroelectric polarization was investigated by the measurement of the current flow between top and bottom electrode for a voltage ramp of frequency f and amplitude U_{Max} applied to the bottom electrode (see Section 4.2.2). The obtained current represents an average of the polarization reorientation within the whole crystal volume below the top electrode.

In Figure 7.3 the calculated hysteresis loops can be seen. The upper image shows the curves measured for a voltage amplitude of 120 V, whereas the lower graph corresponds to a value of 200 V. In both cases the frequency was varied from 1 mHz to 1 kHz.

Two frequency induced effects are clearly visible. An increasing frequency leads to a reduced remanent polarization as well as an increased coercive voltage. This can be seen in more detail in Figure 7.4, where the extracted coercive voltages and the remanent polarizations are plotted as a function of the hysteresis frequency for both experiments presented in Figure 7.3. The averaged values of both switching directions are shown, i.e.

$$U = \frac{U_C^+ + U_C^-}{2} \quad ,$$

and

$$P = \frac{P_r^+ + P_r^-}{2} \quad .$$

A comparison of the hysteresis loops performed with voltage amplitudes of 120 V and 200 V reveals higher values of the coercive voltages as well as of the remanent polarizations at a given frequency for $U_{Max} = 200\,\mathrm{V}$. Obviously, the switching process strongly depends not only on the frequency but also on the amplitude of the applied voltage.

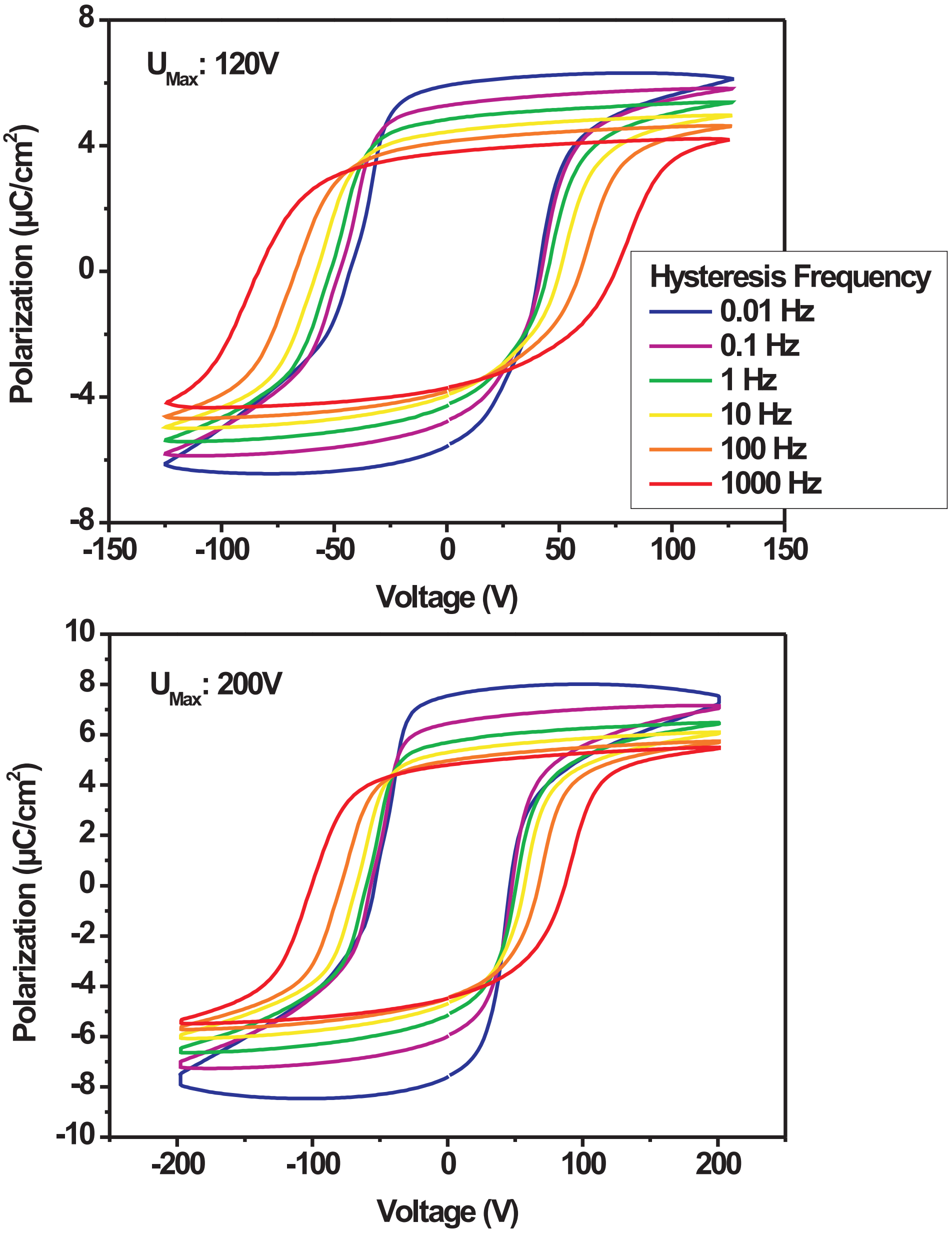

Figure 7.3: Dynamics of polarization switching. The ferroelectric polarization of a PMN-PT single crystal is shown as a function of the applied voltage for frequencies varied from 1 mHz to 1 kHz. The upper image shows experiments with a maximum voltage of 120 V, whereas the lower picture corresponds to measurements performed with a voltage amplitude of 200 V. A strong frequency relaxation of the remanent polarization and the coercive voltage can be seen.

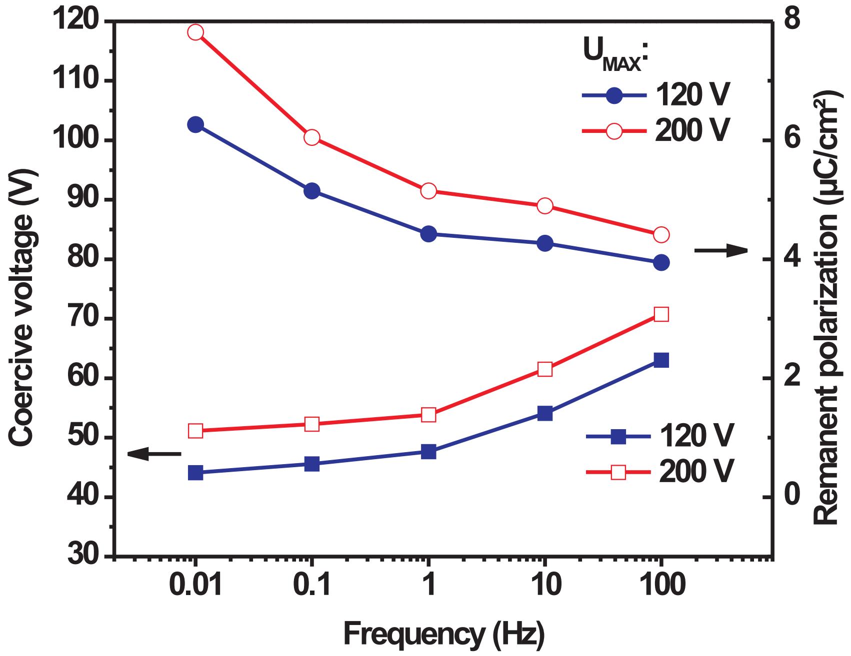

Figure 7.4: Frequency dependence of ferroelectric properties. The values of the coercive voltages and remanent polarizations extracted from both experiments presented in Figure 7.3 are shown as a function of the hysteresis frequency. An increase of the switching voltage and a decrease of the remanent polarisation can be seen for increasing frequencies. Moreover, a voltage amplitude of 200 V results in higher values of the coercive voltage and the achieved polarization than an amplitude of 120 V.

A random-field model has been used to explain this behavior [117]. The small polar clusters, which are typical for relaxor ferroelectrics, are treated as quenched defects, which induce random fields. As mentioned in Section 2.2, these defects change the energy potential of the surrounding crystal volume and lead to spatially different nucleation energies. However, due to the addition of lead titanate the defect density is insufficient to induce a breakdown of the long-range ferroelectric order in the absence of an external electric field. Hence, the material is in a ferroelectric phase, which is characterized by micrometer-sized domains, as can be seen in Figure 7.2.

For the application of an electric field the randomly oriented internal fields lower the energy barrier for domain nucleation in proximity to the quenched defects. Thus, small polar nanoregions with a reversed domain state nucleate even for field strengths smaller than the coercive field E_C within the existing normal ferroelectric domains. For $U_{Max} < U_C$ the intial domain structure is recovered after a certain relaxation time when the field is switched off. Higher field strengths lead to an irreversible nucleation of polar clusters and a remanent polarization with reversed orientation is achieved. The number of polar clusters increases exponentially with a rising applied field and a mesoscale polydomain state is formed [118]. This is in contrast to the polarization switching in conventional ferroelectrics, which is described in Section 2.1.2, where the polarization reverses due to the motion of domain walls.

This model is in principle valid for all ferroelectrics, where defects are present for instance due to stoichiometrical inhomogeinities. However, usually the defect density is much smaller than in relaxor materials and the nucleation of reversed domains is concentrated mainly at domain walls, which are certain defects itself.

The dynamics of the nucleation process are described by the relaxation time τ, which characterizes the velocity of the nucleation process. Thus, the irreversible stage of this process is reached at higher voltage values for increasing hysteresis frequencies and a higher coercive voltage is measured. Moreover, the amount of nucleated clusters is reduced for higher frequencies, since the period the external voltage is applied to the system is reduced. Consequently, the obtained macroscopic remanent polarization is decreased for increasing hysteresis ferquencies, as can be seen in Figures 7.3 and 7.4, and in this sense, the switching process is not fully completed.

The relaxation time τ strongly decreases for higher magnitudes of the applied electric field. Accordingly, larger voltage amplitudes result in a higher switched remanent polarization for a given frequency, as is revealed in Figure 7.4 for the measurements with $\mathrm{U}_{Max} = 120\,\mathrm{V}$ and $200\,\mathrm{V}$. Following this argumentation, one would expect smaller values of the coercive field for an increasing voltage amplitude, since the irreversible nucleation state should be reached at lower voltage values with a smaller realaxation time. However, the opposite can be seen in Figure 7.4, where the obtained coercive voltages are larger for the experiment performed with $\mathrm{U}_{Max} = 200\,\mathrm{V}$. The reason for this is found in the different magnitudes of the remanent polarization. A larger value of P_r requires more nucleated polar clusters to be reversed and consequently more energy supplied to the system. Therefore, the coercive field is enhanced for rising voltage amplitudes.

This is confirmed in Figure 7.5, where the energy dissipated by the system per switching event is shown as a function of the frequency. In order to access this parameter the area included by the left and right branch of the loops presented in Figure 7.3 has been calculated by integration of

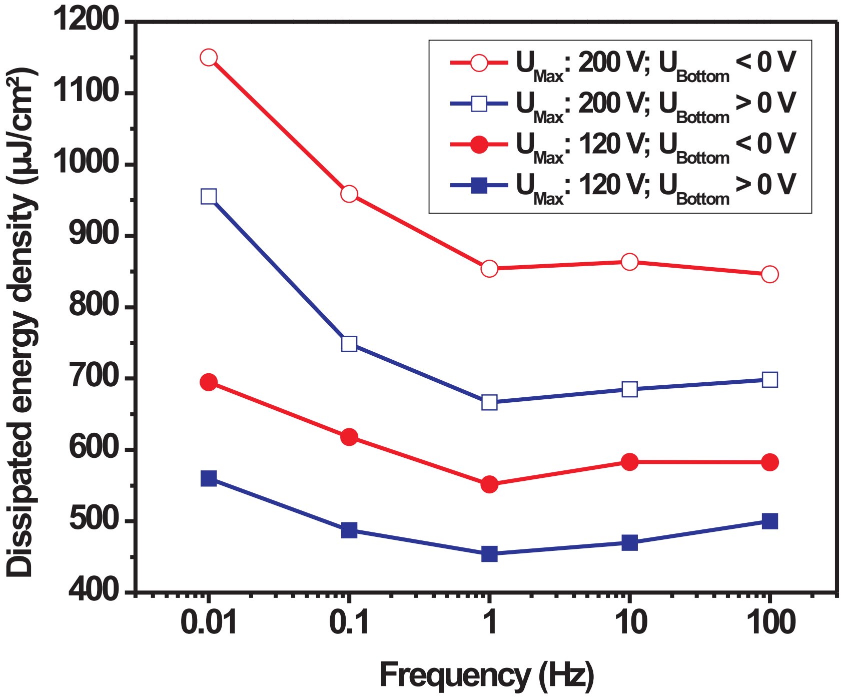

Figure 7.5: Energy dissipation of polarization switching. The areas enclosed by the left and the right half of the hysteresis loops shown in Figure 7.3 correspond to the energy dissipated by the material for the polarization switching with a negative and positive bottom electrode voltage, respectively. These energies are shown as a function of the hysteresis frequency for different voltage amplitudes.

$$E^- = \int_{P_r^+}^{P_r^-} U\,dP \quad , \quad \text{with U} < 0 \quad ,$$

and

$$E^+ = \int_{P_r^-}^{P_r^+} U\,dP \quad , \quad \text{with U} > 0 \quad ,$$

for the switching with a negative and positive bottom electrode voltage, respectively.

Obviously, more energy is dissipated for the polarization reversal with a negative voltage, i.e. in -z-direction, than for a reorientation with U $>$ 0 for both amplitudes of the hysteresis voltage. This is due to the prepoling of the crystals, which are poled to be oriented in +z-direction, as can be seen in Figure 7.2. Thus, this polarization orientation is energetically favored and can be achieved with a lower applied electric field.

Furthermore, the comparison of the switching cycles performed with amplitudes of 120 V and 200 V reveals a higher energy dissipation for the 200 V hysteresis loops. As discussed above, a shorter relaxation time τ for higher applied field strengths leads to more nucleated polar clusters and a higher remanent polarization. Consequently, more energy is required to achieve a macroscopically reversed polarization.

The frequency dependence of the achieved remanent polarization has a strong impact on the electron emission from the investigated PMN-PT crystals. The amount of imbalance screening charges being emitted from the sample surface is determined by the voltage-induced polarization variation, which, in the case of polarization switching, is established by the sum of the two remanent polarizations:

$$\Delta P = \left|P_r^+\right| + \left|P_r^-\right| \quad . \tag{7.1}$$

Accordingly, ΔP is reduced for decreasing values of the remanent polarization and consequently, less surface charges are available for electron emission. This explains the higher amount of emitted charges per single polarization switching cycle for lower excitation frequencies, which is presented in Section 5.2.2.

7.3 Rotation of Ferroelectric Polarization

Beside the random-field based approach, which has been discussed in the previous section, the rotation of the polarization in existing domains has been suggested as a different mechanism to explain the reorientation of the polarization and the large piezoelectric properties in PMN-PT and PZN-PT single crystals. The rotation has been reported to be involved in the phase transition from a rhombohedral to a tetragonal crystal structure for an electric field applied parallel to the polarization direction [119, 120] as well as in a reversal of the polarization direction within a rhombohedral structure for a field antiparallel to the initial polarization orientation [47].

The polarization rotation is accepted to take place via different monoclinic intermediate phases, which are separated by a small energy barrier [121, 122] and used to explain the large electromechanical response of PMN-PT and related compounds.

7.3.1 Configurations of PFM Measurements

In order to clarify the nature of the polarization reversal, within the present work the PMN-PT samples were investigated by means of piezoresponse force microscopy. Three configurations are possible for this kind of experiment, which are shown in Figure 7.6. For all cases, the recorded phase of the z-signal for a hysteresis frequency of 10 mHz and a sketch of the cantilever position with the electrical wiring can be seen.

Part (a) depicts a measurement with the tip positioned directly on the crystal surface. A voltage ramp was applied to the bottom electrode, whereas the tip was put on ground potential. The z-signal phase shows a clear polarization reversal at voltages of $-10\,\mathrm{V}$ and $-1\,\mathrm{V}$ to an orientation in -z and +z-direction, respectively. Accordingly, the polarization state in -z-direction is not stable and the system switches back to the +z-orientation when the applied negative bottom electrode voltage gets larger than $-1\,\mathrm{V}$. It will be shown in Section 7.4 that this effect is caused by the prepolarization of the evironmental area, which strongly favors one particular polarization orientation. However, the switching voltages are significantly smaller than the values obtained from the macroscopic measurements shown in Figures 7.3 and 7.4.

The situation is different if the tip is positioned on the top electrode. For the case of the electrode not being contacted separately, an increased loop width was measured, as can be seen in Figure 7.6 (b), but the revealed coercive voltages of $-6\,\mathrm{V}$ and $30\,\mathrm{V}$ were still smaller than the macroscopic values. In this particular hysteresis measurement, a different sample prepolarization for the investigated area is visible compared to the loop depicted in part (a), since a smaller voltage is needed to initiate the switching process with a negative voltage than for a positive one.

The measured coercive voltages further increase to $-80\,\mathrm{V}$ and $38\,\mathrm{V}$ if the top electrode is contacted separately as is shown in Figure 7.6 (c). These values are comparable to the switching voltages obtained from the macroscopic hysteresis measurements shown in Figure 7.3.

Thus, the configuration of the PFM experiments strongly determines the measured switching properties. The main difference recording conditions behind Figures 7.6 (a) - (c) was the size of the investigated area. For the probe being positioned directly on the sample surface, only a small crystal volume below the tip is excited by the applied voltage and eventually the polarization is switched if the voltage magnitude exceeds a certain threshold value. This is in accordance with the random-field theory based approach introduced in Section 7.2. Within the investigated crystal volume the nucleation of only a

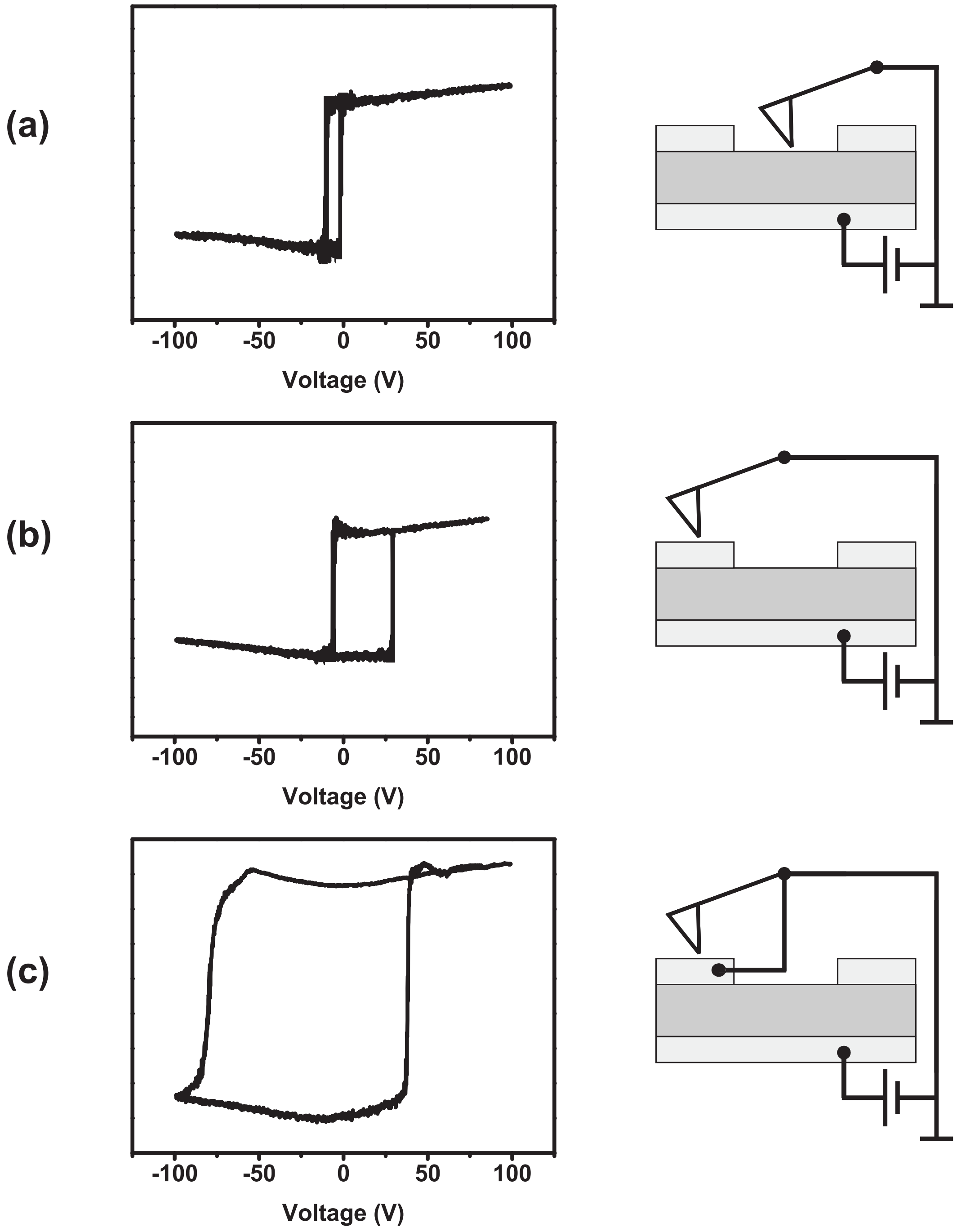

Figure 7.6: Configuration of PFM measurements. The z signal phase and a sketch of the electric wiring are shown for different possibilities to record PFM hysteresis loops. Part (a) depicts the case of the cantilever being positioned directly on the sample surface. A voltage is applied between the conductive tip and the sample bottom electrode. The width of the obtained hysteresis loop with respect to the voltage axis is increased if the probe is located on the top electrode. In part (b) the voltage is again applied between tip and bottom electrode, whereas in part (c) the top electrode is contacted separately.

small amount of polar nanoclusters is sufficient to initiate a polarization reorientation requiring less energy than for the switching of a larger volume. Consequently, the domain reversal is accomplished at lower voltage magnitudes. However, the nucleated clusters are not stable on a macroscopic scale, since the formation of domain walls at the boundaries to the non-switched sample volume also requires a certain energy. Thus, in a zero-field condition, the nucleated region switches back to the initial polarization orientation.

A measurement on top of the electrode leads to an increased area that is influenced by the applied voltage. For the case visible in Figure 7.6 (b), the electrode is connected to ground potential by the conductive AFM probe only. The tip radius of several tens of nanometers leads to a certain contact resistance and thus, to a partial voltage drop at the tip-electrode interface. Nevertheless, the sample volume, which is excited by the applied voltage is larger than for measurements directly on the crystal surface. According to the random-field theory introduced in the previous section, the nucleation of more small polar clusters is required to switch the probed volume and therefore, the obtained width of the hysteresis loop is increased.

If the tip-electrode resistance is short-circuited by additionally contacting the top electrode, the absolute values of the coercive voltages is in the range of the macroscopic ones measured in Figure 7.3, since for this configuration, the wiring was identical with the macroscopic measurements. The whole sample volume below the top electrode is influenced by the applied voltage and the cantilever acts as a sensor for the piezoelectric sample oscillations. The recorded signal thus represents an average over a larger area. The resolution can be quantified to be $\sim 0.2 \cdot \mathrm{d}$ with d representing the sample thickness [123]. This corresponds to approximately $100\,\mu$m for the PMN-PT samples investigated in this work.

7.3.2 Complete Polarization Rotation Path

As has been shown in the previous Section 7.3.1, a PFM configuration, where the top electrode and tip are both put on ground potential, resembles the hysteresis loops obtained by switching current measurements and presented in Figure 7.3. However, a closer look on these experiments reveals some features that are not visible in the current-based hysteresis loops.

In Figure 7.7 the recorded amplitude and phase of the PFM signals in z and x-direction can be seen. The measurements were performed on a PMN-PT crystal that had not been exposed to an external voltage for about 3 years. Thus, the effect of the prepoling of the z polarization component was reduced due to long-term relaxation and the shift along the voltage axis of the hysteresis loops is decreased. Therefore, it was possible to induce a complete 180 ° polarization switching within the available voltage range of ±120 V.

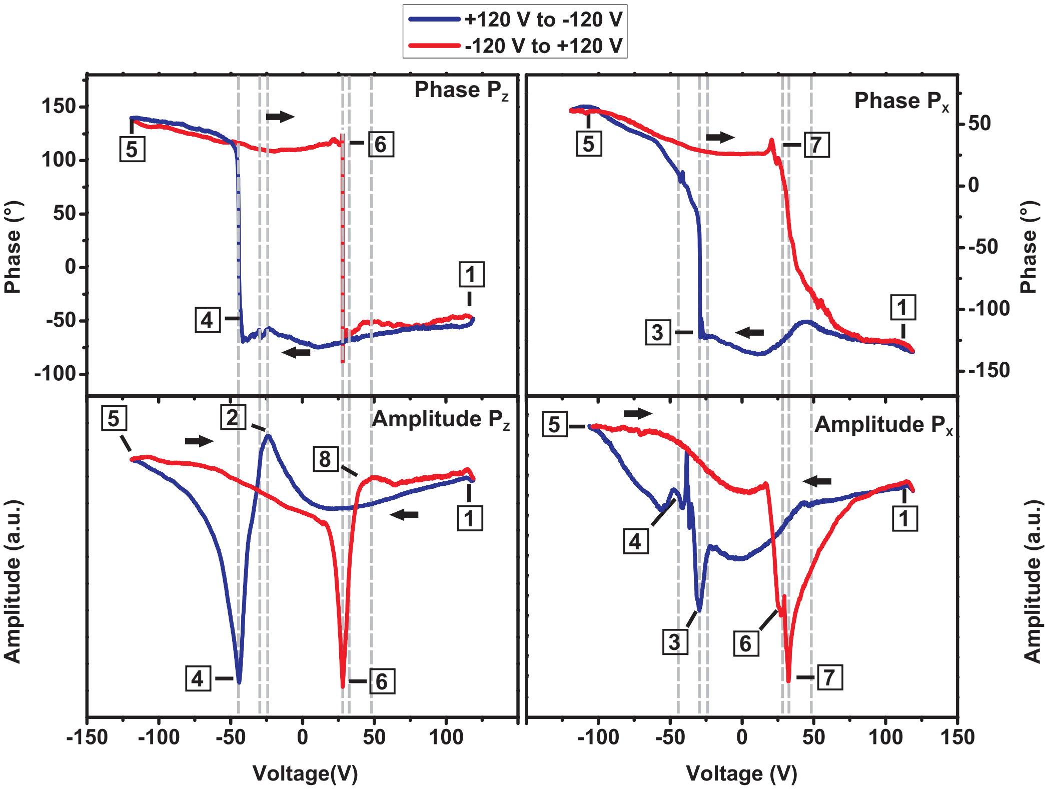

Figure 7.7: PFM measurement of a 180° polarization rotation. Phase and amplitude of the z and x-signals recorded during a PFM measurement on the top electrode of a PMN-PT single crystal are shown. Arrows indicate the direction of the voltage change along the hysteresis curves. A 180° switching of the ferroelectric polarization can be seen. Several features corresponding to a rotation of he polarization vector are visible and labeled with numbers. The vertical grey lines correspond to identified intermediate polarization states and are plotted at the same voltage values for both columns as a guide for the eye.

In all curves the data points corresponding to the transition from a positive to a negative bottom electrode voltage, i.e. a polarization switching in -z-direction, are indicated in blue, whereas the signals measured during the application of a positive voltage can be seen as the red parts of the loops. Vertical grey lines indicate the correlation between these signals upon partial switching and are plotted at the same voltage values for both columns. The signals all together reveal a complete 180° ferroelectric polarization rotation path, what can be deduced from the phase signals in both directions. Clearly, two distinct states can be seen, separated by 180°.

Apart from the changes in the signal phases, several features can be seen in the graphs, which are listed in Table 7.1. The numbers listed in the left column are also indicated in Figure 7.7 near the corresponding features in the PFM curves. Obviously, for both switching directions intermediate maxima of the x and z-amplitudes occur. This cannot be explained by a simple nucleation of reversed domains, which is the mechanism of polarization reversal in most ferroelectrics, but can be related to a rotation of the polarization vector.

Negative bottom electrode voltage

No.	Applied voltage	PFM signal feature
1	120 V	+z-orientation in z-phase -x-orientation in x-phase
2	−23 V	Maximum in z-amplitude
3	−30 V	Minimum in x-amplitude Change in x-phase
4	−44 V	Minimum in z-amplitude Change in z-phase Maximum in x-amplitude

Positive bottom electrode voltage

No.	Applied voltage	PFM signal feature
5	−120 V	-z-orientation in z-phase +x-orientation in x-phase
6	28 V	Minimum in z-amplitude Change in z-phase Maximum in x-amplitude
7	33 V	Minimum in x-amplitude Change in x-phase
8	49 V	Maximum in z-amplitude

Table 7.1: Characteristic features in a PFM measurement of a 180° polarization rotation.

In Figure 7.8 two possible rotation paths are depicted. The numbers correspond to the ones listed in Table 7.1. It can be seen that the cantilever is not oriented parallel to one of the crystallographic [100] and [010] directions. Thus, both in-plane components of the polaritation vector are detected in the x-signal, but with different efficiency.

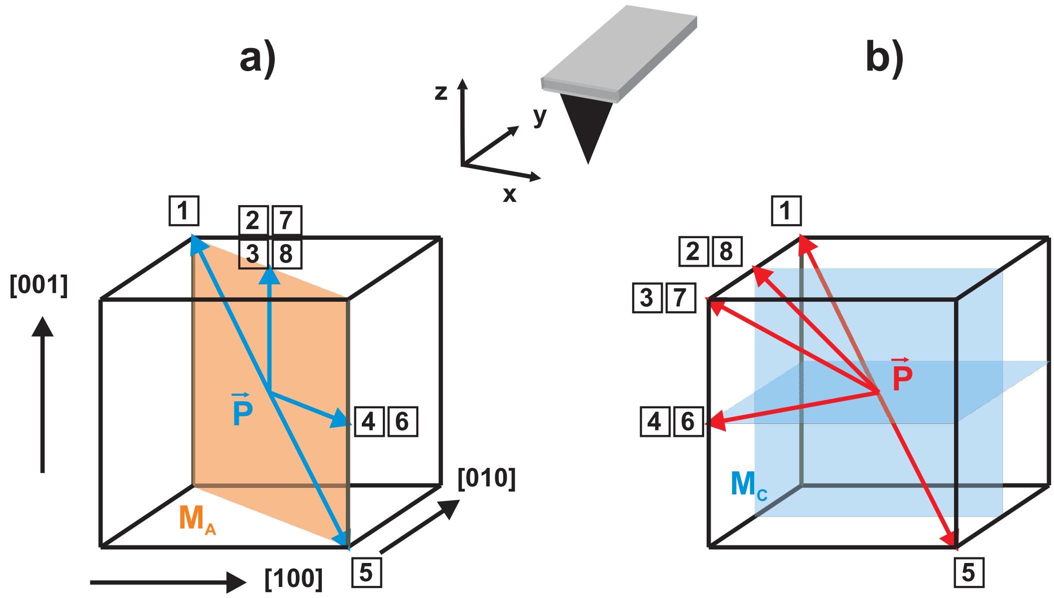

Figure 7.8: Possible rotation paths for a complete switching process within a perovskite unit cell. Part (a) shows the polarization rotation via a monoclinic M_A phase. The numbers correspond to the identified polarization states measured in Figure 7.7 and listed in Table 7.1. In part (b) an alternative path is depicted, where the vector rotates via different monoclinic M_C phases. The cantilever orientation was not parallel to any crystallographic axis.

Rotation via M_A phases Part (a) shows the rotation via a monoclinic M_A phase. The vector is confined within the (110) plane, which connects the two rhombohedral states oriented in $[\bar{1}11]$ and $[1\bar{1}\bar{1}]$ directions.

The rhombohedral $[\bar{1}11]$ polarization state 1 pointing in positive z-direction and negative x-direction is the present state when a positive voltage is applied, and also constituting the initial poling direction. The application of a negative voltage leads to a change of the ferroelectric polarization. For a voltage regime from -23 V to -30 V the polarization is rotated to the states 2 and 3, respectively, which for this rotation path both correspond to an alignment of the polar vector in [001] direction. Accordingly, the z-signal and x-signal amplitudes are increased and decreased, respectively. Simultaneously, the phase of the x-signal starts to change, since the polarization component P_x changes its orientation from -x to +x. A further increase of the applied voltage to approximately -44 V continues the rotation process to state 4, where the vector is oriented along the $[1\bar{1}0]$ direction. This results in a maximized x and a minimized z-signal amplitude. The polarization component P_z changes its orientation from +z to -z which is seen by the change in the z-signal phase. Larger negative voltages result in an increase in amplitude of both the x and z-component of the PFM signal, whereas the phase signals reach a final saturation value. This corresponds to a further rotation of the polarization vector to state 5, which is the final state of the switching path. As a result, both the x and z-components have been switched by 180°. Therefore, the new $[1\bar{1}\bar{1}]$ polarization state is oriented in +x and -z direction.

The ferroelectric polarization can be switched back to state 1 by applying a positive voltage to the PMN-PT crystal following the same rotation path as shown in Figure 7.8 (a). For a voltage bias of about 28 V the polarization is rotated into state 6, where the polarization axis is aligned in $[1\bar{1}0]$ direction. The x and z-amplitudes exhibit a maximum and a minimum, respectively. Simultaneously, a change in the z-signal phase can be seen, since the orientation of the polarization component P_z changes from -z to +z. Increasing voltage values result in a further polarization rotation to state 7 and 8, where the vector is oriented along the z-direction. The polarization component P_x is switched from +x to -x, which is seen by a change of the x-signal phase. A minimum in the x-signal amplitude at 33 V can be seen, whereas the z-signal amplitude increases rapidly reading a peak value at approximately 49 V, while the phase for this direction is constant. The final polarization orientation 1 is reached for voltage values > 50 V. The z-signal amplitude decreases since the polarization vector is partially oriented within the surface plane according to the rhombohedral crystal symmetry.

The rotation of the polarization within a monoclinic M_A phase explains the measured features in the PFM signals. However, there are two basic arguments against this rotation path:

Firstly, the intermediate states 2/3 and 7/8 represent one step within the M_A phase, i.e. a polarization orientation in [001] direction. This state is characterized by a maximized and minimized z and x-signal, respectively. However, these events are initiated at different voltage amplitudes in the PFM signal curves, shown in Figure 7.7. The difference between state 2 and 3 is $\sim 7\,\mathrm{V}$, whereas state 7 and 8 are separated by $\sim 16\,\mathrm{V}$. Generally, the energy difference between the monoclinic polarization orientations is very small [47] and thus, the coexistence of different states within the rotation process is probable. Given a lateral resolution of $\sim 100\,\mu\mathrm{m}$ for the PFM experiments, the obtained signals must be treated as an average of several polarization orientations within the investigated sample volume. Accordingly, corresponding features might be measured at different applied voltage values. However, differences up to 16 V are certainly too large to be seen to occur simultaneously.

Secondly, when switching the polarization with a negative voltage applied to the bottom electrode, the intermediate state 2/3 means a polarization orientation antiparallel to the external field and thus is energetically unfavorable.

Rotation via M_C phases Another possible switching path is shown in Figure 7.8 (b), where the rotation of the polar vector is accomplished by several monoclinic M_C configurations. Again, the starting point is the rhombohedral polarization state 1 pointing in $[\bar{1}11]$ direction. A voltage of $-23\,\mathrm{V}$ leads to a reorientation to the $[\bar{1}01]$ direction within the (010) monoclinic mirror plane, i.e. state 2. Subsequently, the z-amplitude is increased, whereas the x-signal is reduced, since the polarization shows a larger y-component in this orientation. In contrast to the rotation via a monoclinic M_A phase (see Figure 7.8 (a)), the polarization states 2 and 3 are separated for this rotation path. State 3 means a further rotation to a rhombohedral configuration pointing in $[\bar{1}\bar{1}1]$ direction. The x-signal amplitude exhibits a minimum, since the polarization is shifted in the y-direction with respect to the cantilever axis. Higher voltage amplitudes cause an alignment of the polarization to the $[\bar{1}\bar{1}0]$ direction within the (001) monoclinic M_C plane, where the vector is oriented completely in the surface plane. Accordingly, the z-signal is minimized in this configuration and the phase signal shows a change corresponding to the switching of the out-of-plane polarization component. The next identified state for voltage amplitudes of $\sim 120\,\mathrm{V}$ is the final orientation 5, corresponding to a rhombohedral symmetry, where a -z and +x-orientation of the polarization can be obtained from the respective phase signals.

The polarization switching with a positive voltage applied to the bottom electrode can be interpreted to follow the same rotation path via different monoclinic M_C phases. For voltage amplitudes of $28\,\mathrm{V}$ and $33\,\mathrm{V}$ the polarization rotates to state 6 and 7,which are characterized by a switching of the z and x-polarization component, respectively. Orientation 8 is achieved at $49\,\mathrm{V}$ as can be seen in the maximized z-amplitude. Eventually, the polarization shows the initial rhombohedral state 1 for higher voltage values.

The transition between states 4 and 5 is not resolved in the PFM experiments since no characteristic features could be identified in the corresponding voltage regime. More clarification about this is given in the following section.

7.3.3 Incomplete Polarization Rotation Path

The rotation of the polarization was investigated on a different fresh sample, where the initial prepoling was not relaxed. Thus, a negative voltage of $-120\,\mathrm{V}$ was not sufficient to complete the polarization switching in -z-direction. The measurements were performed with the same parameters as for the signals shown in Figure 7.7 and can be seen in Figure 7.9.

Obviously, the z-component of the ferroelectric polarization reverses as can

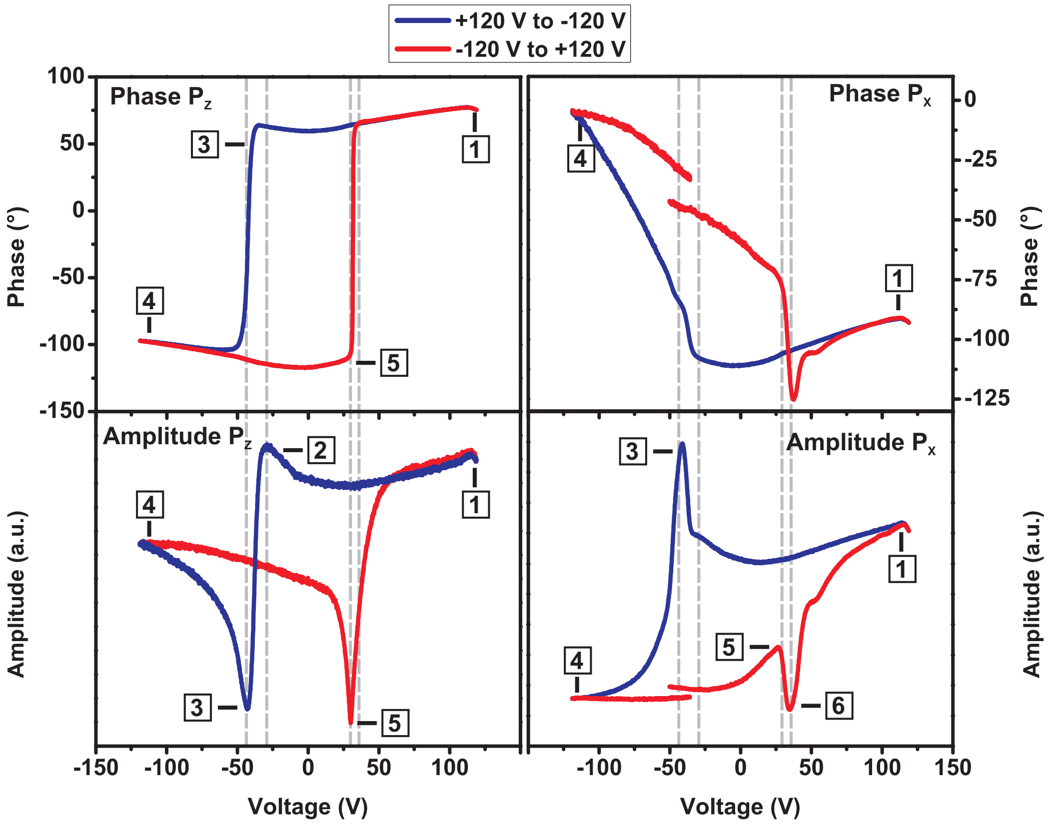

Figure 7.9: PFM measurement of an incomplete polarization rotation. Phase and amplitude of the z and x-signals recorded during a PFM measurement on the top electrode of a PMN-PT single crystal are shown. A reorientation of the ferroelectric polarization in z-direction can be seen in the respective phase signal, wheras the x-signal phase varies only about 100°. Several features corresponding to a rotation of the polarization vector are visible and labeled with numbers. The vertical grey lines correspond to identified intermediate polarization states and are plotted at the same voltage values for both columns as a guide for the eye.

be seen from the phase of the z-signal. However, in contrast to the hysteresis loops presented in Figure 7.7, the process is not a 180 ° switching, since the x-signal phase shows only a variation of about 100 °. Nevertheless, similar features are revealed that can also be attributed to a rotation of the polar vector and are listed in Table 7.2.

Figure 7.10 shows a possible rotation path via different M_C phases, which can be related to the features obtained from the PFM signals, whereas a rotation via M_A phases can be excluded in this case.

Again, the rhombohedral $[\bar{1}11]$ polarization state 1 pointing in positive z-direction and negative x-direction is the starting point when a positive voltage is applied. The application of a negative bottom electrode voltage of $-30\,\mathrm{V}$ results in a rotation of the polar vector to the $[\bar{1}01]$ direction, which is indicated

Negative bottom electrode voltage

No.	Applied voltage	PFM signal feature
1	120 V	+z-orientation in z-phase -x-orientation in x-phase
2	-30 V	Maximum in z-amplitude
3	-44 V	Minimum in z-amplitude Change in z-phase Maximum in x-amplitude

Positive bottom electrode voltage

No.	Applied voltage	PFM signal feature
4	-120 V	-z-orientation in z-phase -x-orientation in x-phase Decrease of the x-amplitude
5	29 V	Minimum in z-amplitude Change in z-phase Maximum in x-amplitude
6	36 V	Minimum in x-amplitude

Table 7.2: Characteristic features in a PFM measurement of an incomplete polarization rotation.

by the maximum in the z-amplitude, as has been observed for the experiment shown in Figure 7.7.

However, higher voltage values lead to a maximum in the x-signal amplitude and a minimized z-signal, which changes its orientation at -44 V. This can be explained by two possible polarization orientations, which are labeled 3 and 3' in Figure 7.10 pointing in the $[\bar{1}00]$ and $[\bar{1}\bar{1}0]$ direction, respectively. Thus, both orientations are aligned within the monoclinic (001) plane and no out-of-plane component of the polarization is present. It cannot be clarified completely from the existing data which polarization state is present, but a coexistence of both is probable.

This assumption is supported by the slight changes that can be seen in the x-signal phase for this voltage regime. Actually, the phase should show either a +x or a -x-orientation (see Equation 4.5) separated by 180 °. Any signal level between these states is not induced by a phase shift of the PFM signal, but likely to be caused by an averaging of the lock-in amplifier integrating the signal over a period of 10 ms. If the phase signal fluctuates from +x to -x

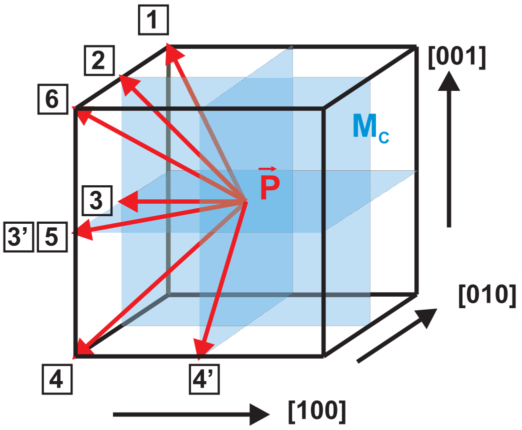

Figure 7.10: Possible rotation paths for an incomplete switching process within a perovskite unit cell via different monoclinic M_C phases. The numbers correspond to the identified polarization states measured in Figure 7.9 and listed in Table 7.2.

during this integration time, the output signal represents an averaged value which leads to the small changes in the x-signal phase of $< 100\,°$.

Larger negative voltage amplitudes up to $-120\,\mathrm{V}$ result in an increased z-signal amplitude, whereas the magnitude of the x-component of the polarization shows a smaller value compared to the previous polarization states. Obviously, the polar vector is moved to the -z-orientation and shifted in y-direction, which results in a smaller x-component. However, no reorientation in +x-direction is revealed in the x-signal phase indicating a non-180 ° polarization switching in this direction. Two possible states can be attributed to the obtained features, which are labeled 4 and 4' in Figure 7.10. The rhombohedral state 4 is oriented in $[\bar{1}\bar{1}\bar{1}]$ direction, whereas the 4' orientation is aligned within the (100) plane in $[0\bar{1}\bar{1}]$ direction. Again, a coexistence of both polarization orientation is probable.

Remarkably, the measured magnitude of the z-polarization component is smaller for state 4 compared to the final state 1 pointing in positive z-direction. This indicates that the switching process is not completed for an applied voltage of $-120\,\mathrm{V}$ and the magnitude of the polarization is not completely rebuilt in -z-direction.

The application of a positive voltage to the bottom electrode switches the polarization back to the rhombohedral state 1. A voltage amplitude of 29 V leads to a change in the z-signal phase and a minimized and maximized z and x-signal, respectively. The polarization is rotated to state 5 being completely oriented in the surface plane. Interestingly, for higher positive voltages a different path is revealed than for the switching with a negative bottom electrode voltage. At a voltage of 36 V the x-signal decreases to the value that has been measured for state 4. Thus, the polarization exhibits the same in-plane orientation as in state 4 and the polar vector is shifted to state 6, which is oriented in $[\bar{1}\bar{1}1]$ direction, corresponding to a rhombohedral crystal symmetry.

Higher voltage amplitudes recover the initial $[\bar{1}11]$ oriented rhombohedral polarization state 1. However, in contrast to the other switching directions and the experiment shown in Figure 7.7 no maximum in the z-signal amplitude has been measured, and thus no indication of a $[\bar{1}01]$ alignment (state 2) of the polarization is visible.

Summarizing the PFM measurements shown in Figures 7.7 and 7.9, it can be stated that a rotation of the ferroelectric polarization has been revealed, which is more probable to proceed via monoclinic M_C than M_A phases. This is in contradiction to the expectation of stable M_A phases for a lead titanate content of 28 % [116] made in Section 7.1. Several intermediate states have been identified corresponding to different rotation paths. Obviously, multiple sequences of intermediate polarization orientations are possible on a local scale and the obtained signals represent an average over several polarization states. The additional measurements of the y-polarization component, which can be accomplished by a sample rotation about 90 °, might give more clarification of the actual rotation path.

7.3.4 Multiphase Coexistence

In order to visualize the coexistence of different monoclinic phases within the polarization rotation process, the following experiment was performed, which can be see in Figure 7.11. A negative voltage of −120 V was applied to the bottom electrode for both samples corresponding to the measurements shown in Figures 7.7 and 7.9. Subsequently, the domain distribution in x-direction was imaged within the aperture region of the top electrode used for electron emission experiments. This method provides the advantage of a higher resolution when scanning directly on the sample surface.

The negative bottom electrode voltage reverses the polarization to the states 5 and 4/4’ for the case of a complete 180 ° (see Figure 7.8) and an incomplete switching process (see Figure 7.10), respectively.

Obviously, for the complete polarization reversal the x-component exhibits a uniform orientation within the aperture region, which corresponds to the stable $[1\bar{1}\bar{1}]$ rhombohedral configuration (state 5 in Figure 7.8). In contrast, the incomplete switching process results in a more diversified domain structure. Generally, the left part of the free surface area is oriented in -x-direction, whereas the right section mainly shows an +x-alignment. The reason for this

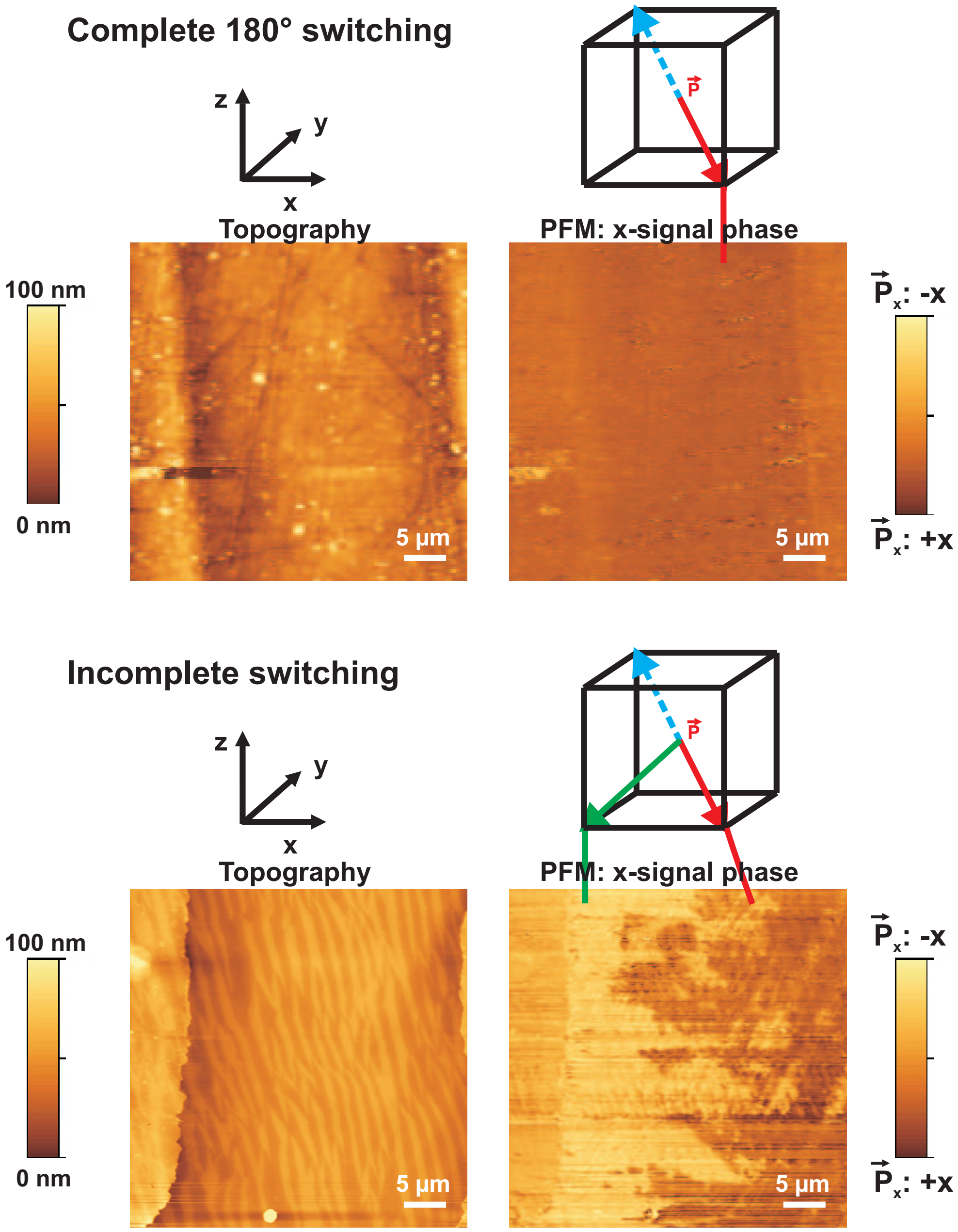

Figure 7.11: In-plane polarization orientation for a complete and incomplete rotation process. A voltage of -120 V was applied to the bottom electrode of the samples corresponding to the measurements of a complete and incomplete rotation shown Figures 7.7 and Figures 7.9, respectively. Subsequently, the x-orientation (in-plane) of the polarization in the aperture region of the top electrode has been imaged and is shown in the right column. The left images represent the topopraphy of the investigated area, which was measured simultaneously. The alignment of the polarization vector in the perovskite unit cell is sketched for both cases. The blue arrow represents the initial orientation at the beginning of the switching process, whereas the green and red arrows correspond to polarization states at the end of the polarization rotation.

behavior is found in the horizontal electric field components which are present in the aperture region and have been calculated in Figure 5.16. In case of a negative voltage applied to the bottom electrode the lines of electric flux are oriented towards the aperture center, thus leading to a converse x-component of the electric field for both parts of the free surface area. If the sample exhibits a monoclinic symmetry, as for an incomplete switching process, the distinct monoclinic states are only separated by a small energy barrier and the horizontal field component is sufficient to change the polarization orientation. In terms of the intermediate states depicted in Figure 7.10, the -x domains correspond to the $[\bar{1}\bar{1}\bar{1}]$ rhombohedral state 4, whereas a +x orientation belongs to the $[0\bar{1}\bar{1}]$ monoclinic state 4'.

7.4 Polarization State in Electron Emission Structures

The experiments presented in the previous sections of this chapter investigated the polarization reversal for the sample volume below the top electrode. However, the electron emission is supposed to be originated in the aperture region between the two electrode components. Thus, it is necessary to investigate the polarization state directly in the free surface area in order to correlate the properties of the electron emission (see Chapter 5) with changes of the ferroelectric polarization.

To accomplish this, a dc bias U_0 was applied to the bottom electrode for several seconds, whereas the top electrode was put on ground potential. After the voltage had been switched off, PFM measurements of the aperture region were performed.

The results can be seen in Figure 7.12, where the orientation of the z-polarization component within the free surface area is shown for different applied voltages U_0. In the upper row the topography and the initial domain structure of the investigated area are depicted. The polarization is completely oriented out of the sample surface, i.e. in +z-direction.

It is clearly visible that even after the application of only $-50\,\mathrm{V}$, which is well below the coercive voltage, small regions with a reversed domain orientation appear within the aperture mainly close to the electrode edges. According to Figure 3.3, the electric field is enhanced in proximity to the electrode. Higher magnitudes of U_0 lead to an increasing fraction of a reversed polarization and for a voltage regime of $-75\,\mathrm{V}$ to $-80\,\mathrm{V}$, which corresponds to the coercive voltage of this particular sample, the crystal volume below the top electrode is

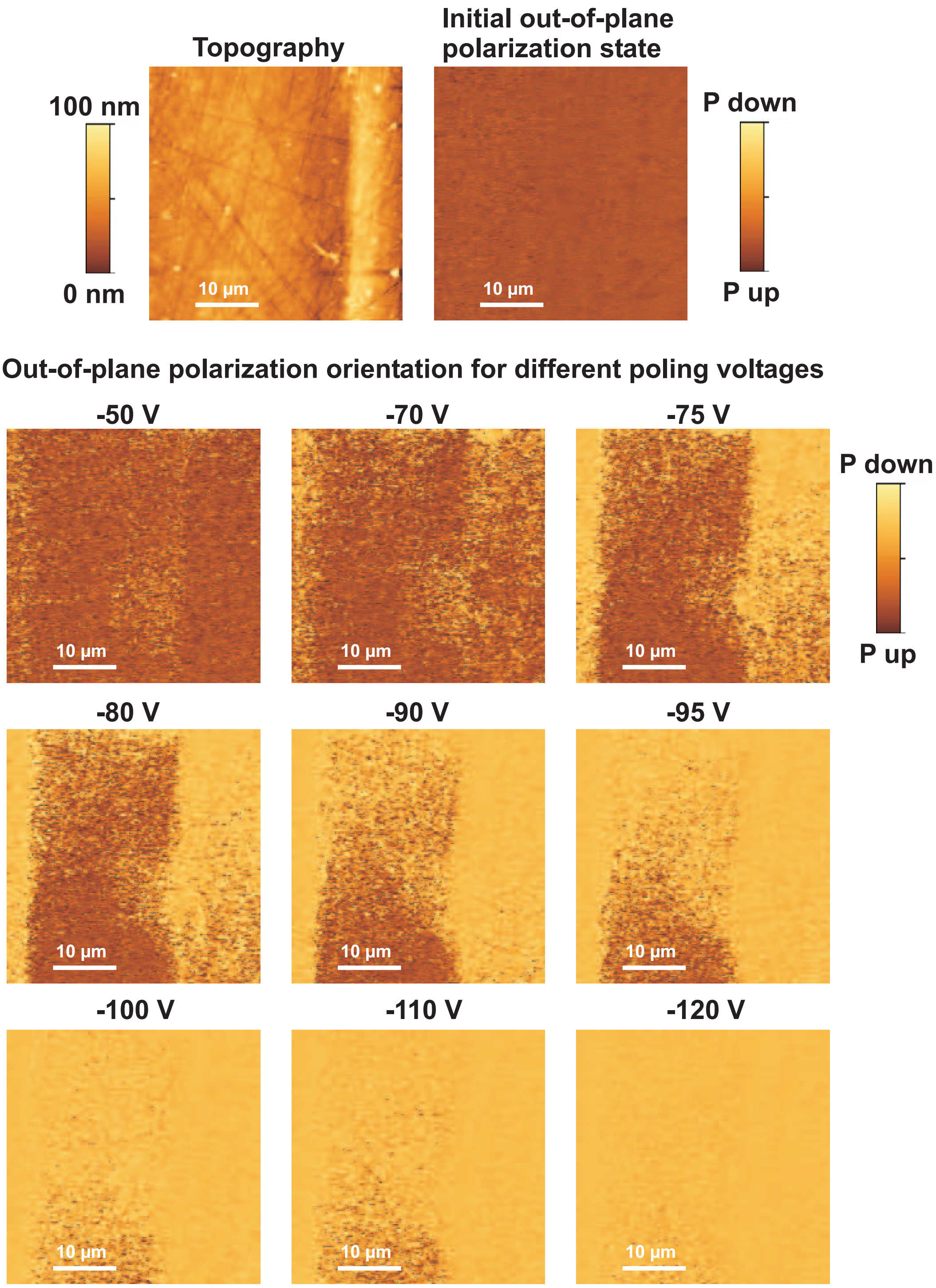

Figure 7.12: Voltage dependent polarization state in electron emission structures. Different negative poling voltages up to -120 V were applied to the sample bottom electrode. Subsequently, the z-orientation (out-of-plane) in the aperture region has been imaged. The upper images represent the topography of the investigated area and the initial domain structure, which is uniformly oriented in +z-direction. An increasing fraction of the free surface area is switched in -z-direction for rising magnitudes of the poling voltage.

completely switched to the -z-orientation. For $U_0 = -120\,\mathrm{V}$, the whole aperture region exhibits the reversed domain state. Obviously, the polarization switching is not driven by a continuous movement of domain walls from the electrode edges towards the aperture center but by the nucleation of randomly located small regions with reversed polarization orientation. The higher the applied electric field the more nucleated regions appear, finally covering the whole free surface area.

These measurements directly proove that the free surface area is influenced by an electric field applied between top and bottom electrodes. Moreover, comparing the PFM measurements shown in Figure 7.12 with the recorded electron emission currents presented in Figure 5.5, a correlation of the onset of the third emission regime for an excitation voltage of $\sim 120\,\mathrm{V}$ and the complete switching of the entire aperture region can be seen. The third regime is characterized by an almost constant slope of the recorded emission current with increasing excitation voltage.

If the polarization is reversed in the whole aperture region, the area, where the electron emission is initiated, is constant. Thus, an increase of the emission current for higher voltages is driven by the rising field strength only. In contrast, in the second emission regime ($U < 120\,\mathrm{V}$) an increasing fraction of the free surface area is switched and therefore, the electron emission process originates from a larger area resulting in an increasing slope for rising excitation voltages.

A closer look on the PFM images presented in Figure 7.12 reveals that a higher fraction of the aperture region is switched in the upper half of the images. This is the area, which is scanned firstly during the measurements. Usually, the recording of an image takes about 15 minutes. This gives rise to the assumption that there is some relaxation of the domain switching on a time scale of several minutes, i.e. the reversed polarization state is not stable.

In Figure 7.13 the time evolution of the polarization can be seen for the examples of poling voltages of $-75\,\mathrm{V}$ and $-100\,\mathrm{V}$. The domain orientation in z-direction was imaged 1 min and 15 min after the external voltage had been switched off.

It is clearly visible that for a poling with $-75\,\mathrm{V}$ the area of domains oriented in -z-direction strongly decreases after 15 min. In this case, only a minority of the free surface area shows the reversed polarization state. The domain walls surrounding the small clusters are energetically unfavorable and thus, the initial polarization orientation is recovered within a certain period. In contrast, no such relaxation was revealed for a switching voltage of $-100\,\mathrm{V}$, where a larger fraction of the aperture region is switched by the poling field.

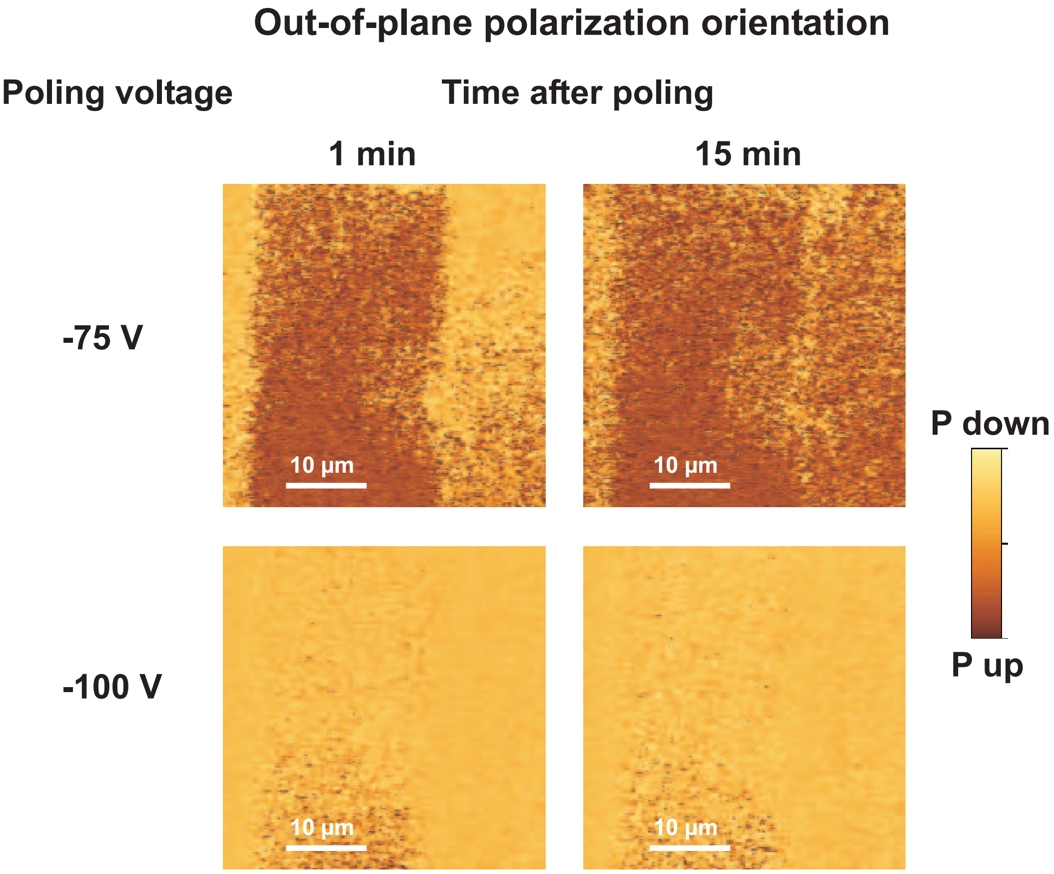

Figure 7.13: Relaxation of polarization. The time stability of the reversed domains shown in Figure 7.12 was investigated and is shown for the examples of poling voltages of -75 V and -100 V. The z-orientation was measured immediately after the poling procedure and after a period of 15 minutes. Obviously, the fraction of reversed domains decreases with time for a poling voltage of -75 V, whereas the achieved domain structure is stable for a value of -100 V.

Due to the rather long relaxation time of this process, there should be no impact on the electron emission from these structures. Usually the emission is initiated with excitation frequencies $> 100\,\mathrm{Hz}$ and thus completed on much shorter time scales.

In order to investigate the impact of the environmental area on the switching of the ferroelectric polarization PFM hysteresis loops were measured directly on the crystal surface. As is known from Figure 7.6 smaller coercive voltages are obtained for this experiment compared to a macroscopic hysteresis loop with a voltage applied between top and bottom electrodes.

Figure 7.14 shows the phase of the z-signals for two measurements obtained for different prepolarizations of the sample. Obviously, both loops are strongly asymmetric and shifted along the voltage axis in different directions.

For a sample prepolarization in +z-direction a voltage of $-38\,\mathrm{V}$ is required

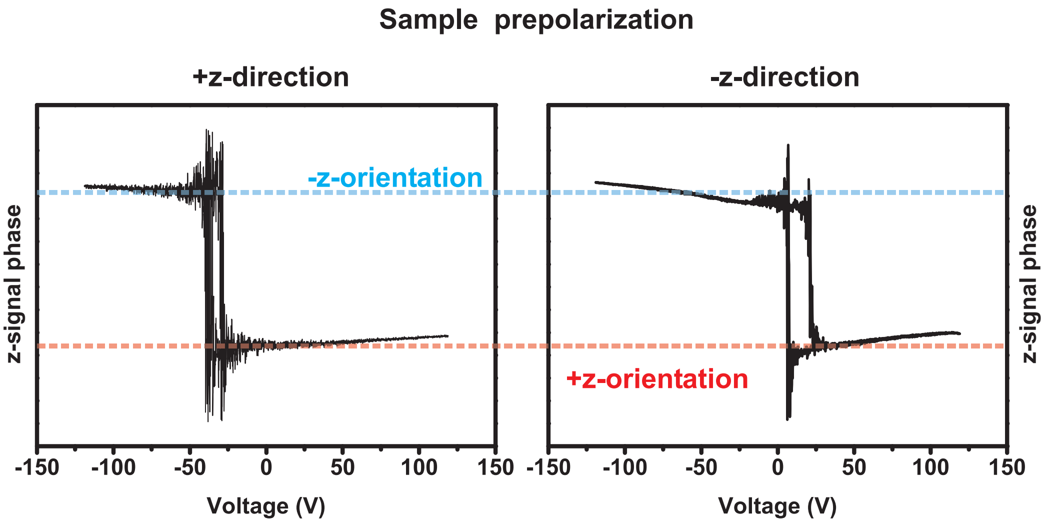

Figure 7.14: Impact of the sample prepolarization on the local polarization switching. PFM hysteresis loops were measured directly on the surface of a PMN-PT single crystal. The z-signal phase (out-of-plane) is shown for a sample prepolarization in +z-direction and -z-direction on the left-hand and right-hand side, respectively. Obviously, both curves exhibit a strong shift along the voltage axis but in different directions.

to intiate a polarization reversal in the opposite direction. If the voltage gets larger than −28 V the polarization switches back to its initial orientation.

A similar behavior is observed for the case of a prepoling in -z-direction. The polarization is reoriented to a +z-orientation for voltages $> 21\,\mathrm{V}$ and recovers a -z-orientation for values $< 6\,\mathrm{V}$.

Accordingly, the reversed domain state is not stable without an externally applied electric field for both presented hysteresis loops. Furthermore, the polarization of the surrounding crystal volume strongly determines the switching properties of the ferroelectric polarization on a local scale.

8 General Conclusions and Future Perspectives

8.1 Summary

In this work electron emission from ferroelectric materials was investigated paying particular attention to the influence of the spontaneous polarization. The focus was set on structures promising a stable emission at low operation voltages. Two routes were followed to achieve this goal.

Firstly, lead magnesium niobate - lead titanate (PMN-PT) was chosen as emitter material, because of its low coercive field strength. Thus, a large variation of the ferroelectric polarization could be accomplished with low applied voltages even for single crystals of 400 μm thickness. The PMN-PT samples were prepared with split gold top electrodes exhibiting a 25 μm wide gap region. Applying an ac voltage between the two top electrodes and the bottom electrode initiated electron emission from the aperture. Current densities up to $5 \cdot 10^{-5}$ A/cm^2 were achieved for an extraction voltage of 160 V, which corresponds to a field strength of 4 kV/cm. A variation of the excitation frequency revealed that more charges are emitted per single emission pulse for decreasing frequencies. Furthermore, the onset of complete polarization reversal has been shown to significantly enhance the recorded emission current.

Secondly, the thickness of the emitter material was decreased. Lead zirconate titanate (PZT) thin films being 600 nm thick were used as emitter material. It was shown that, in order to achieve a polarization reversal in the whole aperture region of the top electrode, smaller gap sizes are required for a reduced sample thickness. A novel approach was implemented to prepare top electrodes with sub-micrometer sized regularly patterned apertures. Based on a monolayer of polystyrene particles, which were used as a mask during the evaporation of a metal layer, the size and the distribution of the apertures can be easily tuned to optimize the electron emission process. The application of an ac voltage resulted in a stable emission signal being initiated at voltage amplitudes above the coercive voltage of the investigated films.

The mechanism of polarization reversal in the PMN-PT crystals was thoroughly investigated macroscopically and on the nanoscale. The presence of monoclinic phases has been revealed by means of piezoresponse force microscopy. A rotation of the polarization vector via so-called monoclinic M_A phases was observed for an applied external electric field with a resolution of about $100\,\mu$m. These intermediate phases probably coexist within the investigated sample volume and several rotation paths are possible until the final reversed polarization state is achieved.

Macroscopic measurements of the switching current showed a decreasing remanent polarization for rising frequencies. This was explained by a limited velocity of domain nucleation exhibiting the reversed polarization orientation and is the reason for the smaller amount of emitted charges per switching cycle for higher excitation frequencies. The nucleation of randomly located small polar clusters was directly imaged within the electron emission structures even for voltage amplitudes below the coercive voltage obtained macroscopically. This is in accordance with a random-field based theory.

It is believed that both revealed mechanisms of polarization switching, i.e. polarization rotation and nucleation of small polar clusters, occur simultaneously. Consequently, the magnitude of the polarization vector is not constant during the rotation process.

8.2 Outlook

The goal of this work was to proove the possibility of low-voltage ferroelectric electron emission and to understand the role of the polarization within this process. Taking this as a starting point, it is simple to optimize the existing cathodes and achieve results that may one day initiate devices based on this structures.

To *increase the emission current* the top electrode structures can be improved for both investigated materials. The slit between the two electrode fragments of the PMN-PT crystals represents a very simple aperture structure that offered the possibility to investigate the polarization state in the free surface region. One could for instance think of a configuration of inderdigitating fingers, which would provide some significant field enhancement in the free surface region. The top electrode preparation for the PZT thin films can also be improved. Apart from an extension to larger electrode areas, a large fraction of the aperture area is lost by an incomplete removal of the polysterene particles. Thus, an increased free surface area can easily be accomplished and will certainly lead to larger emission currents for both presented sample-electrode configurations.

The size of the aperture represents a very important parameter. Generally, a polarization reversal of the whole free surface region is desired to achieve a maximized emission signal. Therefore, the ideal dimension of the gap region depends on the intended excitation voltage of the cathode and should be chosen to result in a complete polarization switching of the aperture at this particular voltage value. This is required to establish high repulsive electric fields close to the sample surface and to enhance the electron emission process. Accordingly, the aperture size is a trade-off between a maximized free surface area and a complete switching in this region.

To *decrease the emission voltage* it is possible to reduce the thickness of the emitter material. This might be problematic for thin films, since the requirement of smaller apertures complicates the top electrode preparation process and leads to an increased impact of competitive effects. However, for the PMN-PT crystals this is an easy task to do. Even with the existing aperture structure of a simple $25\,\mu$m wide gap between two top electrode components, a reduction of the sample thickness down to about $100\,\mu$m is expected to have no effect on the obtained emission currents, but would reduce the coercive voltage and therefore the operating voltage drastically. Emission currents of several nA at excitations of $< 40\,$V are imaginable. This combination would be superior to most ferroelectric cathodes known so far.

Provided the application of moderate voltages $< 200\,$V, the lifetime of the PMN-PT cathodes was $> 10^9$ switching cycles and solely limited by the high piezoelectric coefficients of PMN-PT. Probably, samples of another composition away from the morphotropic phase boundary (25% - 35% of lead titanate content) will reduce generated mechanical stress and strongly *enhance the cathode lifetime.*

References

[1] E. Goldstein: *Ueber eine noch nicht untersuchte Strahlungsform an der Kathode inducirter Entladungen.* Annalen der Physik **300**, 38–48 (1898).

[2] J. J. Thomson: *Cathode Rays.* Phil. Magazine **44**, 293–316 (1897).

[3] A. Einstein: *Über einen die Erzeugung und Verwandlung des Lichtes betreffenden heuristischen Gesichtspunkt.* Annalen der Physik **322**, 132–148 (1905).

[4] M. Knoll and E. Ruska: *Das Elektronenmikroskop.* Z. Physik **78**, 318–339 (1932).

[5] B. Rosenblum, P. Bräunlich, and J. P. Carrico: *Thermally stimulated field emission from pyroelectric* $LiNbO_3$. Appl. Phys. Lett. **25**, 17–19 (1974).

[6] J. Valasek: *Piezoelectricity and Allied Phenomena in Rochelle Salt.* Phys. Rev. **17**, 475–481 (1921).

[7] J. F. Scott: *Ferroelectric Memories.* Springer-Verlag, Berlin-Heidelberg-New York (2000).

[8] L. Peng, L. Ran, H. Chen, H. Zhang, J. A. Kong, and T. M. Grzegorczyk: *Experimental Observation of Left-Handed Behavior in an Array of Standard Dielectric Resonators.* Phys. Rev. Lett. **98**, 157403, 1–4 (2007).

[9] Q. Zhao, B. Du, L. Kang, H. Zhao, Q. Xie, B. Li, X. Zhang, J. Zhou, L. Li, and Y. Meng: *Tunable negative permeability in an isotropic dielectric composite.* Appl. Phys. Lett. **92**, 051106, 1–3 (2008).

[10] G. Rosenman, D. Shur, Y. E. Krasik, and A. Dunaevsky: *Electron emission from ferroelectrics.* J. Appl. Phys. **88**, 6109–6161 (2000).

[11] H. Gundel, H. Riege, E. J. N. Wilson, J. Haderek, and K. Zioutas: *Copious electron emission from PLZT ceramics with high zirconium concentration.* Ferroelectrics **100**, 1–16 (1989).

[12] R. Drori, M. Einat, D. Shur, E. Jerby, G. Rosenman, R. Advani, R. J. Temkin, and C. Pralong: *Demonstration of microwave generation by a ferroelectric-cathode tube.* Appl. Phys. Lett. **74**, 335–337 (1999).

[13] G. Rosenman, D. Shur, and A. Skliar: *Ferroelectric electron emission flat panel display.* J. Appl. Phys. **79**, 7401–7403 (1996).

[14] S.-E. Park and T. R. Shrout: *Ultrahigh strain and piezoelectric behavior in relaxor based ferroelectric single crystals.* J. Appl. Phys. **82**, 1804–1811 (1997).

[15] R. Waser: *Nanoelectronics and Information Technology.* Wiley-CH, Weinheim (2003).

[16] F. Schlaphof: *Kraftmikroskopische Untersuchungen dünner ferroelektrischer Filme.* Ph.D. thesis, TU Dresden (2005).

[17] C. Kittel: *Introduction to Solid State Physics.* Wiley, New York (2005).

[18] M. Lines and A. Glass: *Principles and Applications of Ferroelectrics and Related Materials.* Clarendon Press, Oxford (1977).

[19] J. Seidel, L. W. Martin, Q. He, Q. Zhan, Y.-H. Chu, A. Rother, M. E. Hawkridge, P. Maksymovych, P. Yu, M. Gajek, N. Balke, S. V. Kalinin, S. Gemming, F. Wang, G. Catalan, J. F. Scott, N. A. Spaldin, J. Orenstein, and R. Ramesh: *Conduction at domain walls in oxide multiferroics.* Nat. Mater. **8**, 229–234 (2009).

[20] A. Haußmann, P. Milde, C. Erler, and L. M. Eng: *Ferroelectric Lithography: Bottom-up Assembly and Electrical Performance of a Single Metallic Nanowire.* Nano Lett. **9**, 763–768 (2009).

[21] M. Abplanalp, J. Fousek, and P. Günter: *Higher Order Ferroic Switching Induced by Scanning Force Microscopy.* Phys. Rev. Lett. **86**, 5799–5802 (2001).

[22] A. M. Bratkovsky and A. P. Levanyuk: *Easy Collective Polarization Switching in Ferroelectrics.* Phys. Rev. Lett. **85**, 4614–4617 (2000).

[23] C. S. Ganpule, V. Nagarajan, S. B. Ogale, A. L. Roytburd, E. D. Williams, and R. Ramesh: *Domain nucleation and relaxation kinetics in ferroelectric thin films.* Appl. Phys. Lett. **77**, 3275–3277 (2000).

[24] J. F. Scott: *Applications of Modern Ferroelectrics.* Science **315**, 954–959 (2007).

[25] N. Setter and R. Waser: *Electroceramic Materials.* Acta Mater. **48**, 151–178 (2000).

[26] V. K. Wadhawan: *Introduction to ferroic materials.* Gordon and Breach (2000).

[27] O. Auciello, J. F. Scott, and R. Ramesh: *The Physics of Ferroelectric Memories.* Physics Today **51**, 22–27 (1998).

[28] L. E. Cross: *Relaxor Ferroelectrics.* Ferroelectrics **76**, 241–267 (1987).

[29] N. Setter and L. E. Cross: *The role of B-site cation disorder in diffuse phase transition behavior of perovskite ferroelectrics.* J. Appl. Phys. **51**, 4356–4360 (1980).

[30] Z. Kighelman, D. Damjanovic, and N. Setter: *Electromechanical properties and self-polarization in relaxor $Pb(Mg_{1/3}Nb_{2/3})O_3$ thin films.* J. Appl. Phys. **89**, 1393–1401 (2001).

[31] L. A. Bursill, H. Qian, J. L. Peng, and X. D. Fan: *Observation and analysis of nanodomain textures in the dielectric relaxor lead magnesium niobate.* Physica B **216**, 1–23 (1995).

[32] Z.-G. Ye and H. Schmid: *Optical, dielectric and polarization studies of the electric field-induced phase transition in $Pb(Mg_{1/3}Nb_{2/3})O_3$[PMN].* Ferroelectrics **145**, 83–108 (1993).

[33] B. E. Vugmeister and H. Rabitz: *A phenomenology of relaxor ferroelectrics.* Ferroelectrics **201**, 33–42 (1997).

[34] D. Viehland, S. J. Jang, L. E. Cross, and M. Wuttig: *Freezing of the polarization fluctuations in lead magnesium niobate relaxors.* J. Appl. Phys. **68**, 2916–2921 (1990).

[35] S. Ogawa: *On Polymorphic Change of Barium Titanate.* J. Phys. Soc. Jpn. **1**, 32–33 (1946).

[36] N. A. Pertsev, A. G. Zembilgotov, and A. K. Tagantsev: *Equilibrium States and Phase Transitions in Epitaxial Ferroelectric Thin Films.* Ferroelectrics **223**, 79–90 (1999).

[37] L.-B. Li, X.-M. Wu, X.-M. Lu, and J.-S. Zhu: *Effect of external mechanical stress on the domain structure of* $Pb(Zr_{0.35}Ti_{0.65})O_3$ *thin films.* Solid State Commun. **135**, 703–706 (2005).

[38] G. S. Ganpule, A. Stanishevsky, Q. Su, S. Aggarwal, J. Melngailis, E. Williams, and R. Ramesh: *Scaling of ferroelectric properties in thin films.* Appl. Phys. Lett. **75**, 409–411 (1999).

[39] A. V. Bune, V. M. Fridkin, S. Ducharme, L. M. Blinov, S. P. Palto, A. V. Sorokin, S. G. Yudin, and A. Zlatkin: *Two-dimensional ferroelectric films.* Nature **391**, 874–877 (1997).

[40] T. Tybell, C. H. Ahn, and J.-M. Triscone: *Ferroelectricity in thin perovskite films.* Appl. Phys. Lett. **75**, 856–858 (1999).

[41] V. Nagarajan, J. Junquera, J. Q. He, C. L. Jia, R. Waser, K. Lee, Y. K. Kim, S. Baik, T. Zhao, R. Ramesh, P. Ghosez, and K. M. Rabe: *Scaling of structure and electrical properties in ultrathin epitaxial ferroelectric heterostructures.* J. Appl. Phys. **100**, 051609, 1–10 (2006).

[42] N. A. Pertsev, J. Rodríguez Contreras, V. G. Kukhar, B. Hermanns, H. Kohlstedt, and R. Waser: *Coercive field of ultrathin* $Pb(Zr_{0.52}Ti_{0.48})O_3$ *epitaxial films.* Appl. Phys. Lett. **83**, 3356–3358 (2003).

[43] J. Wang, J. B. Neaton, H. Zheng, V. Nagarajan, S. B. Ogale, B. Liu, D. Viehland, V. Vaithyanathan, D. G. Schlom, U. V. Waghmare, N. A. Spaldin, K. M. Rabe, M. Wuttig, and R. Ramesh: *Epitaxial* $BiFeO_3$ *Multiferroic Thin Film Heterostructures.* Science **299**, 1719–1722 (2003).

[44] B. Noheda, D. E. Cox, G. Shirane, J. Gao, and Z.-G. Ye: *Phase diagram of the ferroelectric relaxor* $(1-x)PbMg_{1/3}Nb_{2/3}O_3$-$xPbTiO_3$. Phys. Rev. B **66**, 054104 (2002).

[45] G. Xu, H. Luo, H. Xu, and Z. Yin: *Third ferroelectric phase in PMNT single crystals near the morphotropic phase boundary composition.* Phys. Rev. B **64**, 020102, 1–3 (2001).

[46] H. Fu and R. E. Cohen: *Polarization rotation mechanism for ultrahigh electromechanical response in single-crystal piezoelectrics.* Nature **403**, 281–283 (2000).

[47] F. Fang, X. Lu, and W. Yang: *Polarization rotation and multiphase coexistence for* $Pb(Mg_{1/3}Nb_{2/3})O_3$*-*$PbTiO_3$ *single crystals at the morphotropic phase boundary under electric loading.* Phys. Rev. B **79**, 174118, 1–6 (2009).

[48] A. A. Levin, C. Thiele, P. Paufler, and D. C. Meyer: *In-situ X-ray investigation of a* $PbMg_{1/3}Nb_{2/3}O_3$*-28%*$PbTiO_3$ *single-crystal plate in an external electric field.* Appl. Phys. A **84**, 37–45 (2006).

[49] D. I. Woodward, J. Knudsen, and I. M. Reaney: *Review of crystal and domain structures in the* $PbZr_xTi_{1-x}O_3$ *solid solution.* Phys. Rev. B **72**, 104110, 1–8 (2005).

[50] V. S. Vidyarthi: *Multi-target sputtering technology of* $Pb(Zr,Ti)O_3$ *thin films for electron devices.* Ph.D. thesis, TU Dresden (2008).

[51] H. Riege: *Electron emission from ferroelectrics - a review.* Nucl. Instrument. Methods Phys. Res. A **340**, 80–89 (1994).

[52] H. Riege: *Ferroelectric electron emission: Principles and technology.* Appl. Surf. Sci. **111**, 318–324 (1997).

[53] B. Sujak and W. A. Syslo: *Emission of high-energy free charge carriers in vacuum as a symptom of pyroelectric properties.* Ferroelectrics **22**, 711–712 (1978).

[54] K. Biedrzycki: *New Aspects of Electron Emission from Virgin TGS Single Crystals.* Phys. Status Solidi A **93**, 503–508 (1986).

[55] J. Park, Y. T. Kim, and K. H. Yoon: *Effect of thickness and upper electrode diameter on polarization switching and electron emission of* $Pb(Zr_{0.8}Ti_{0.2})O_3$ *ferroelectric cathode.* J. Appl. Phys. **91**, 1458–1463 (2002).

[56] M. Angadi, O. Auciello, A. R. Krauss, and H. W. Gundel: *The role of electrode material and polarization fatigue on electron emission from ferroelectric* $Pb(Zr_xTi_{1-x})O_3$ *cathodes.* Appl. Phys. Lett. **77**, 2659–2661 (2000).

[57] D. Shur, G. Rosenman, Y. E. Krasik, and V. D. Kugel: *Plasma-assisted electron emission from (Pb,La)(Zr,Ti)O_3 ceramic cathodes.* J. Appl. Phys. **79**, 3669–3674 (1996).

[58] H. Gundel, J. Handerek, and H. Riege: *Time-dependent electron emission from ferroelectrics by external pulsed electric fields.* J. Appl. Phys. **69**, 975–982 (1991).

[59] G. I. Rosenman, O. V. Malyshkina, and Y. L. Chepelev: *Electron emission at switching of ferroelectrics.* Ferroelectrics **110**, 99–112 (1990).

[60] M. Molotskii, A. Agronin, P. Urenski, M. Shvebelman, G. Rosenman, and Y. Rosenwaks: *Ferroelectric Domain Breakdown.* Phys. Rev. Lett. **90, 1-4**, 107601 (2003).

[61] H. Gundel, H. Riege, E. J. N. Wilson, J. Hańderek, and K. Zioutas: *Fast polarization changes in ferroelectrics and their application in accelerators.* Nucl. Instrum. Methods Phys. Res. A **280**, 1–6 (1989).

[62] B. Jiang, G. Kirkman, and N. Reinhardt: *High brightness electron beam produced by a ferroelectric cathode.* Appl. Phys. Lett. **66**, 1196–1198 (1995).

[63] D. Flechtner, C. Golkowski, J. D. Ivers, G. S. Kerslick, J. A. Nation, and L. Schächter: *Electron emission from lead-zirconate-titanate ceramics.* J. Appl. Phys. **83**, 955–961 (1998).

[64] H. Gundel, J. Hańderek, H. Riege, and E. J. N. Wilson: *Electric field-excited electron emission from PLZT-X/65/35 ceramics.* Ferroelectrics **110**, 183–192 (1990).

[65] D. Averty, S. F. Liateni, and R. Le Bihan: *Electron emission from ferroelectric crystals of different thickness.* Ferroelectrics **173**, 171–180 (1995).

[66] D. N. J. Shannon, P. W. Smith, P. J. Dobson, and M. J. Shaw: *Dual mode electron emission from ferroelectric ceramics.* Appl. Phys. Lett. **70**, 1625–1627 (1997).

[67] G. H. Haertling and C. McCampbell: *A new longitudinal display mode for ceramic electrooptic devices.* Proc. IEEE **60**, 450–451 (1972).

[68] S. Chen, X. Dong, S. Zheng, Z. Zhu, and C. Tang: *Electron Emission from Barium Strontium Titanate Ceramics.* J. Am. Ceram. Soc. **89**, 2118–2122 (2006).

[69] D. Shur, G. Rosenman, and Y. E. Krasik: *Surface discharge plasma induced by spontaneous polarization switching.* Appl. Phys. Lett. **70**, 574–576 (1997).

[70] W. Zhang and W. Huebner: *Mixed electron emission from doped Pb(Zr,Ti)*O_3 *ceramics: Microstructural aspects.* J. Appl. Phys. **83**, 6034–6037 (1998).

[71] Y. T. Kim, J. Park, and K. H. Yoon: *Electron Emission from* $Pb(Zr_{0.65}Ti_{0.35})O_3$ *film cathode by pulse electric field.* Mater. Res. Bull. **37**, 631–639 (2002).

[72] O. Auciello, M. A. Ray, D. Palmer, J. Duarte, G. E. McGuire, and D. Temple: *Low voltage electron emission from* $Pb(Zr_xTi_{1-x})O_3$*-based thin film cathodes.* Appl. Phys. Lett. **66**, 2183–2185 (1995).

[73] E. Sviridov, R. Le Bihan, S. Liateni, and A. Désécures: *Electron emission spectra from lead zirconate titanate ferroelectric films on stainless-steel substrates.* Appl. Phys. Lett. **73**, 3953–3955 (1998).

[74] J. Park, Y. T. Kim, and K. H. Yoon: *Influence of Thickness on the Emission Treshold Field of the* $Pb(Zr_{0.4}Ti_{0.6})O_3$ *(PZT) Films.* Jpn. J. Appl. Phys. **41**, L647–L650 (2002).

[75] F. Liu and C. B. Fleddermann: *Electron emission from thin-film ferroelectric cathodes.* Appl. Phys. Lett. **76**, 1618–1620 (2000).

[76] K. Biedrzycki and L. Markowski: *Vacuum emission of electrons from* $(Pb,Ca)TiO_3$ *thin films.* Solid State Comm. **107**, 391–393 (1998).

[77] A. Ghemes, Y. Neo, M. Okada, T. Aoki, and H. Mimura: *Low Voltage Electron Emission from* $BaTiO_3$ *Ferroelectric Thin Films.* Integr. Ferroelectrics **104**, 25–33 (2008).

[78] I. Ohwada, T. Sugiyama, and T. Nanataki: *Electron Emission from Ferroelectric Electron Emitter at Transient State of Negative Polarization Reversal.* Jpn. J. Appl. Phys. **46**, 5981–5987 (2007).

[79] I. Ohwada, T. Sugiyama, and T. Nanataki: *A Ferroelectric Electron Emitter Having a Vacuum Gap.* Electron. Comm. Jpn. **92**, 21–30 (2009).

[80] T. Sugiyama, K. Sato, Y. Mori, I. Ohwada, H. Yamaguchi, and T. Nanataki: *Investigation of Factor Causing Deterioration of Ferroelectric Electron Emitter.* Jpn. J. Appl. Phys. **48**, 051401 (2009).

[81] R. H. Fowler and L. Nordheim: *Electron emission in intense electric fields.* Proc. Roy. Soc. **A119**, 173–181 (1928).

[82] Y. E. Krasik, K. Chirko, A. Dunaevsky, J. Z. Gleizer, A. Krokhmal, A. Sayapin, and J. Felsteiner: *Ferroelectric Plasma Sources and Their Applications.* IEEE Trans. Plasma Sci. **31**, 49–59 (2003).

[83] H. Riege, I. Boscolo, J. Handarek, and U. Herleb: *Features and technology of ferroelectric electron emission.* J. Appl. Phys. **84**, 1602–1617 (1998).

[84] Y. Hayashi and E. Hotta: *Characteristics of Microwave Amplification Using an Electron Beam Generated from Ferroelectric Cathode.* Jpn. J. Appl. Phys. **42**, L869–L872 (2003).

[85] B. Naranjo, J. K. Gimzewski, and S. Putterman: *Observation of nuclear fusion driven by a pyroelectric crystal.* Nature **434**, 1115–1117 (2005).

[86] H. Klumbies: *Elektronenemission aus ferroelektrischen Dünnschichten.* Diploma thesis, TU Dresden (2008).

[87] G. Binnig and H. Rohrer: *Scanning tunneling microscopy.* Helvetia Physica Acta **55**, 726–735 (1982).

[88] G. Binnig and D. P. E. Smith: *Single-tube three-dimensional scanner for scanning tunneling microscopy.* Rev. Sci. Instrum. **57**, 1688–1689 (1986).

[89] G. Binnig, C. F. Quate, and C. Gerber: *Atomic Force Microscope.* Phys. Rev. Lett. **56**, 930–933 (1986).

[90] E. Meyer: *Atomic Force Microscopy.* Prog. Surf. Sci. **41**, 3–43 (1992).

[91] F. J. Giessibl: *Advances in atomic force microscopy.* Rev. Mod. Phys. **75**, 949–983 (2003).

[92] G. Meyer and N. M. Amer: *Novel optical approach to atomic force microscopy.* Appl. Phys. Lett. **53**, 1045–1046 (1988).

[93] G. Meyer and N. M. Amer: *Erratum: Novel optical approach to atomic force microscopy.* Appl. Phys. Lett. **53**, 2400–2402 (1988).

[94] S. Alexander, L. Hellemans, O. Marti, J. Scheir, V. Elings, P. K. Hansma, M. Longmire, and J. Gurley: *An atomic-resolution atomic-force microscope implemented using an optical lever.* J. Appl. Phys. **65**, 164–167 (1989).

[95] O. Mieth: *Ferroelectric polarization influenced by mechanical stress.* Diploma thesis, TU Dresden (2005).

[96] P. Güthner and K. Dransfeld: *Local poling of ferroelectric polymers by scanning force microscopy.* Appl. Phys. Lett. **61**, 1137–1139 (1992).

[97] K. Franke, J. Besold, W. Haessler, and C. Seegebarth: *Modifcation and detection of domains on ferroelectric PZT films by scanning force microscopy.* Surf. Sci. Lett. **302**, L283–L288 (1994).

[98] M. Abplanalp, L. M. Eng, and P. Günter: *Mapping the domain distribution at ferroelectric surfaces by scanning force microscopy.* Appl. Phys. A **66**, S231–S234 (1998).

[99] L. M. Eng, M. Bammerlin, C. Loppacher, M. Guggisberg, R. L. R. Bennewitz, E. Meyer, T. Huser, H. Heinzelmann, and H.-J. Güntherodt: *Ferroelectric Domain Characterisation and Manipulation: a Challenge for Scanning Probe Microscopy.* Ferroelectrics **153**, 153–163 (1999).

[100] E. Grimsehl, W. Schallreuter, and A. Lösche: *Lehrbuch der Physik, Band 4, Struktur der Materie.* Teubner Verlag (Leipzig) (1990).

[101] L. M. Eng, H.-J. Güntherodt, G. A. Schneider, U. Köpke, and J. Muñoz Saldaña: *Nanoscale reconstruction of surface crystallography from three-dimensional polarization distribution in ferroelectric barium-titanate ceramics.* Appl. Phys. Lett. **74**, 233–236 (1999).

[102] C. Loppacher, F. Schlaphof, S. Schneider, U. Zerweck, S. Grafström, L. M. Eng, A. Roelofs, and R. Waser: *Lamellar ferroelectric domains in* $PbTiO_3$ *grains imaged and manipulated by AFM.* Surf. Sci. **532**, 483–487 (2003).

[103] C. Harnagea, A. Pignolet, M. Alexe, D. Hesse, and U. Gösele: *Quantitative ferroelectric characterization of single submicron grains in Bi-layered perovskite thin films.* Appl. Phys. A **70**, 261–267 (2000).

[104] C. Harnagea, A. Pignolet, M. Alexe, and D. Hesse: *Piezoresponse Scanning Force Microscopy: What Quantitative Information Can We Really Get Out of Piezoresponse Measurements on Ferroelectric Thin Films.* Integr. Ferroelectrics **44**, 113–124 (2002).

[105] C. Harnagea, M. Alexe, and D. Hesse: *Contact resonances in voltage-modulated force microscopy.* Appl. Phys. Lett. **83**, 338–340 (2003).

[106] S. V. Kalinin and D. A. Bonnell: *Imaging mechanism of piezoresponse force microscopy of ferroelectric surfaces.* Phys. Rev. B **65**, 125408, 1–11 (2002).

[107] T. Hidaka, T. Maruyama, M. Saitoh, N. Mikoshiba, M. Shimizu, T. Shiosaki, L. A. Wills, R. Hiskes, S. A. Dicarolis, and J. Amano: *Formation and observation of 50 nm polarized domains in* $PbZr_{1-x}Ti_xO_3$ *thin film using scanning probe microscope.* Appl. Phys. Lett. **68**, 2358–2359 (1996).

[108] L. M. Eng, M. Abplanalp, and P. Günter: *Ferroelectric domain switching in tri-glycine sulphate and barium titanate bulk single crystals by scanning force microscopy.* Appl. Phys. A **66**, S679–S683 (1998).

[109] S. Jesse, B. J. Rodriguez, S. Choudhury, A. P. Baddorf, I. Vrejoiu, D. Hesse, M. Alexe, E. A. Eliseev, A. N. Morozovska, J. Zhang, L.-Q. Chen, and S. V. Kalinin: *Direct imaging of the spatial and energy distribution of nucleation centres in ferroelectric materials.* Nat. Mater. **7**, 209–215 (2008).

[110] C. Jullian, J. F. Li, and D. Viehland: *Investigation of polarization switching in* $(001)_C$, $(110)_C$, *and* $(111)_C$ *oriented* $Pb(Zn_{1/3}Nb_{2/3})O_3$*-4.5%* $PbTiO_3$ *crystals.* J. Appl. Phys. **95**, 5671–5678 (2004).

[111] G. Suchaneck, W.-M. Lin, V. S. Vidyarthi, G. Gerlach, and J. Hartung: *Multi-target reactive sputtering - A promising technology for large area* $Pb(Zr,Ti)O_3$ *thin film deposition.* J. Eur. Ceram. Soc. **27**, 3789–3792 (2007).

[112] V. S. Vidyarthi, W. M. Lin, G. Suchaneck, G. Gerlach, C. Thiele, and V. Hoffmann: *Plasma emission controlled multi-target reactive sputtering for in-situ crystallized* $Pb(Zr,Ti)O_3$ *thin films on 6" Si-wafers.* Thin Solid Films **515**, 3547–3553 (2007).

[113] M. Klais, H. Gundel, and G. Schönhesse: *Energy-resolved analysis of ferroelectric electron emission from TGS using electron microscopy.* Appl. Phys. A **80**, 545–549 (2005).

[114] V. V. Shvartsman and A. L. Kholkin: *Domain structure of* $0.8Pb(Mg_{1/3}Nb_{2/3})O_3$-$0.2PbTiO_3$ *studied by piezoresponse force microscopy.* Phys. Rev. B **69**, 014102, 1–5 (2004).

[115] D. Vanderbilt and M. H.Cohen: *Monoclinic and triclinic phases in higher-order Devonshire theory.* Phys. Rev.B **63**, 094108, 1–9 (2001).

[116] A. K. Singh and D. Pandey: *Structure and the location of the morphotropic phase boundary region in (1-x)[Pb($Mg_{1/3}Nb_{2/3}$)O_3-xPbTiO_3.* J. Phys.: Condens. Matter **13**, L931–L936 (2001).

[117] D. Viehland and Y.-H. Chen: *Random-field model for ferroelectric domain dynamics and polarization reversal.* J. Appl. Phys. **88**, 6696–6707 (2000).

[118] Q.Tan and D.Viehland: *ac-field-dependent structure-property relationships in La-modified lead zirconate titanate: Induced relaxor behavior and domain breakdown in soft ferroelectrics.* Phys.Rev.B **53**, 14103–14111 (1996).

[119] F. Bai, N. Wang, J. Li, D. Viehland, P. M. Gehring, G. Xu, and G. Shirane: *X-ray and neutron diffraction investigations of the structural phase transformation sequence under electric field in 0.7Pb($Mg_{1/3}Nb_{2/3}$)-0.3PbTiO_3 crystal.* J. Appl. Phys. **96**, 1620–1627 (2004).

[120] B. Noheda, D. E. Cox, G. Shirane, S.-E. Park, L. E. Cross, and Z. Zhong: *Polarization Rotation via a Monoclinic Phase in the Piezoelectric 92%Pb$Zn_{1/3}Nb_{2/3}O_3$-8%PbTiO_3.* Phys. Rev. Lett. **86**, 3891–3894 (2001).

[121] Z. Kutnjak, J.Petzelt, and R. Blinc: *The giant electromechanical response in ferroelectric relaxors as a critical phenomenon.* Nature **44**, 956–959 (2006).

[122] M. Davis, D. Damjanovic, and N. Setter: *Electric-field, temperature-, and stress-induced phase transitions in relaxor ferroelectric single crystals.* Phys. Rev. B **73**, 014115, 1–16 (2006).

[123] S. V. Kalinin, B. Rodriguez, S.-H. Kim, S.-K. Hong, A. Gruverman, and E. A. Eliseev: *Imaging mechanism of piezoresponse force microscopy in capacitor structures.* Appl. Phys.Lett. **92**, 152906, 1–3 (2008).

List of Figures

List of Tables

Publications

Articles

A1 E. I. Shishkin, V. Ya. Shur, **O. Mieth**, L. M. Eng, L. L. Galambos, and R. O. Miles: *Kinetics of the Local Polarization Switching in Stoichiometric* $LiTaO_3$ *Under Electric Field Applied Using the Tip of Scanning Probe Microscope.* Ferroelectrics **340**, 129-136 (2006).

A2 G. Suchaneck, V. S. Vidyarthi, **O. Mieth**, G. Gerlach, L. Eng, A. V. Solnyshkin, and I. L. Kislova: *Electron emission from ferroelectric thin films enhanced by the presence of 90° ferroelectric domains.* IEEE Trans. Ultrason. Ferroelec. Freq. Control **54**, 2555 - 2561 (2007).

A3 S. C. Kehr, M. Cebula, **O. Mieth**, T. Härtling, J. Seidel, S. Grafström, L. M. Eng, S. Winnerl, D. Stehr, and M. Helm: *Anisotropy contrast in phonon-enhanced apertureless near-field microscopy using a free-electron laser.* Phys. Rev. Lett. **100**, 256403 (2008).

A4 O. Bilani-Zeneli, A. D. Rata, A. Herklotz, **O. Mieth**, L. M. Eng, L. Schultz, M. D. Biegalski, H. M. Christen, and K. Dörr: $SrTiO_3$ *on piezoelectric PMN-PT(001) for application of variable strain.* J. Appl. Phys. **104**, 054108 (2008).

A5 **O. Mieth**, H. Klumbies, V. S. Vidyarthi, G. Gerlach, K. Dörr, and L. M. Eng: *Low-voltage electron emission from thin* $[Pb(Mg_{1/3}Nb_{2/3})O_3]_{0.72}[PbTiO_3]_{0.28}$ *single crystals induced by ferroelectric polarization switching.* New J. Phys. **11**, 023004 (2009).

A6 Y. Kan, Y. Liu, **O. Mieth**, H. Bo, X. Wu, X. Lu, L. M. Eng, and J. Zhu: *Mechanical stress induced polarization reorientation in polycrystalline* $Bi_{3.25}La_{0.75}Ti_3O_{12}$ *films.* Phys. Lett. A **374**, 360-365 (2009).

A7 **O. Mieth**, E. Beyreuther, and L. M. Eng: *Dynamics of ferroelectric polarization rotation in PMN-PT single crystals.* In preparation (2010).

A8 J. Becherer, **O. Mieth**, E. Beyreuther, V. S. Vidyarthi, G. Gerlach, and L. M. Eng: *Low voltage ferroelectric electron emission from PZT thin films with novel regularly arranged nanometer-sized electrodes.* In preparation (2010).

Talks

T1 **O. Mieth**, H. Klumbies, V. S.Vidyarthi, P. Reichenbach, G. Gerlach, and L. M. Eng: *Electron emission from ferroelectric thin films induced by polarization switching.* 2nd International Workshop on Smart Materials and Structures. August 29th to 31st 2007, Kiel, Germany.

T2 **O. Mieth**, H. Klumbies, V. S.Vidyarthi, P. Reichenbach, G. Gerlach, and L. M. Eng: *Electron emission from ferroelectric thin films induced by polarization switching.* Annual Meeting of the Deutsche Physikalische Gesellschaft - spring meeting (DPG-2008). February 25th to 29th 2008, Berlin, Germany.

T3 **O. Mieth**, V. S.Vidyarthi, G. Gerlach, K. Dörr, and L. M. Eng: *Low voltage electron emission from* $[Pb(Mg_{1/3}Nb_{2/3})O_3]_{0.72}$ $[PbTiO_3]_{0.28}$ *single crystals induced by ferroelectric polarization switching.* Annual Meeting of the Deutsche Physikalische Gesellschaft - spring meeting (DPG-2009). March 22th to 27th 2009, Dresden, Germany.

T4 **O. Mieth**, V. S.Vidyarthi, G. Gerlach, K. Dörr, and L. M. Eng: *Low voltage electron emission from PMN-PT single crystals induced by ferroelectric polarization switching.* 16th International Workshop on Oxide Electronics (WOE16). October 4th to 7th 2009, Tarragona, Spain.

Posters

P1 **O. Mieth**, H. Klumbies, T. Otto, L. M. Eng, G. Milde, G. Suchaneck, V. Vidyarthi, and G. Gerlach: *Electron emission from ferroelectric thin films.* The 9th International Symposium on Ferroic Domains and Micro- to Nanoscopic Structures (ISFD-9). June 26th to 30th 2006, Dresden, Germany.

P2 P. Milde, **O. Mieth**, A. Haußmann, and L. M. Eng: *PFM as a versatile tool for probing and manipulating ferroelectric samples.* ORNL Users Week 2007. October 8th to 11th 2007, Oak Ridge, USA.

P3 **O. Mieth**, J. Becherer, E. Beyreuther, and L. M. Eng: *Low voltage electron emission from ferroelectric single crystals and thin films.* The 10th International Symposium on Ferroic Domains and Micro- to Nanoscopic Structures (ISFD-10). September 20th to 24th 2010, Prague, Czech Republic.

Acknowledgments

It is a great pleasure to thank all the people who supported me in any way during my work on this thesis.

First of all I thank my supervisor Professor Lukas Eng, who introduced me into the interesting world of ferroelectricity, ensured the funding of my work, and gave me a lot of freedom to implement my own ideas.

Many thanks go to Professor Ramamoorthy Ramesh for evaluating my work and for giving me the opportunity to join his group for three months. It was a great experience to see how things are done at the other end of the world.

I thank Dr. Elke Beyreuther for reading the manuscript with incredible care.

Furthermore, I thank Dr. Kathrin Dörr and Dr. Vinay Shankar Vidyarthi for providing the PMN-PT and PZT samples, respectively.

I am deeply indebted to Dr. Susanne “Sanni” Kehr, who teached me the girl’s method of finding failures and motivated me in times, which were mainly characterized by short-circuits and vacuum leaks. You are the best tabletop soccer defender the institute has ever seen.

I thank Alexander Haußmann for valuable scientific input and Ralf Raupach for designing the HV-amplifier.

Many thanks go to the whole SPM^2 group for the comfortable atmosphere of mutual support.

All in all, it was very convenient to work in the iapp. I met lots of nice people and enjoyed friendships with Roman Forker, Selina Olthof, Christian Uhrich, and Robert Gehlhaar. Thank you for all-night Warcraft sessions, the visits of festivals and football matches, and all the other fun!

Beside the science, my family and my girlfriend Ilona always supported me and brought me back on track. Thank you for being there!

Erklärung

Diese Dissertation wurde am Institut für Angewandte Physik/Photophysik der Fakultät Mathematik und Naturwissenschaften an der Technischen Universität Dresden unter wissenschaftlicher Betreuung von Prof. Dr. Lukas Eng angefertigt.

Hiermit versichere ich, dass ich die vorliegende Arbeit ohne unzulässige Hilfe Dritter und ohne Benutzung anderer als der angegebenen Hilfsmittel angefertigt habe; die aus fremden Quellen direkt oder indirekt übernommenen Gedanken sind als solche kenntlich gemacht. Die Arbeit wurde bisher weder im Inland noch im Ausland in gleicher oder ähnlicher Form einer anderen Prüfungsbehörde vorgelegt.

Ich versichere weiterhin, dass keinerlei frühere Promotionsverfahren stattgefunden haben.

Ich erkenne die Promotionsordnung der Fakultät Mathematik und Naturwissenschaften an der Technischen Universität Dresden vom 20.03.2000, in der Fassung der vom Fakultätsrat am 19.06.2002 und 12.07.2002 beschlossenen und mit Erlass des Sächsischen Staatsministeriums für Wissenschaft und Kunst vom 18.03.2003 genehmigten Änderungen gemäß Satzung vom 16.04.2003 sowie gemäß der Änderungssatzung vom 17.07.2008, an.

Oliver Mieth
Dresden, den 11.03.2010